Assessing the influence of supraglacial lakes to the mass balance of Tapado Glacier

Augusto Cezar Lima do Nascimento

Thesis for Masters of Science Degree at the University of Bergen, Norway

2023

©Copyright Augusto Cezar Lima do Nascimento

The material in this publication is protected by copyright law.

Year: 2023

Title: Assessing the influence of supraglacial lakes to the mass balance of Tapado Glacier

Author: Augusto Cezar Lima do Nascimento

Acknowledgements

I would like to express my deepest gratitude to the following people, without whom I would never have completed this thesis:

First and foremost, I extend my sincere appreciation to my supervisor, Benjamin Robson. I am grateful for your enthusiasm, invaluable guidance, and support through my academic path, which significantly enhanced the quality of this thesis. I cannot thank you enough for your patience and support, especially at times when I was unable to deliver my best.

I extend this gratitude to my co-supervisor, Álvaro Ayala, which enriched this thesis providing beautiful drone images from his field work. And to Emerson Galvani, who are guiding me since my bachelor studies in Brazil and is a major contributor to my academic journey and where I stand today.

A special thank you goes to Brage, my dearest boyfriend, who is likely missing me during this month of absence when my time was consumed entirely by the thesis. Your understanding and support mean the world to me. I extend my gratitude to all the friends I've made during my time here in Bergen. Whether some have already departed, or others remain, I want to thank you for the camaraderie and the incredible amount of fun we've shared. It is mostly thanks to all of you that I now consider Bergen my home.

And last, but certainly not least, a heartfelt thank you to my mother, Elizabete, who remains in Brazil and whom I miss dearly. Your love, unconditional support, and encouragement have been my pillars. I will be forever grateful to you.

Berge, November 2023

Gus

Abstract

Glaciers are an important source of water for agriculture, mining and large population residing in downstream basins in the semiarid Andes. The Tapado Complex (2.44 km^2) is the main glacier in the catchment Coquimbo-La Serena, thus estimations of ablation rates, area extent, surface lowering, as for glacier inventories, etc. have been strategical for government policies and actions. In order to estimate the longevity of these water stores, it is important to understand the components and systems that play a central role in governing the mass balance. Supraglacial ponds and ice cliffs are of pivotal importance in debris-cover glacier wasting, producing what is called "debris-covered glacier anomaly", it refers to an unexpected behavior when glaciers covered with debris exhibits a mass balance like that of a clean ice glacier, typically attributed to those features that can influence melting patterns. Although the Centro de Estudos Avanzados de Zonas Áridas (CEAZA) has been exploring the cryosphere in the Tapado Complex in the later years with excellence, nor extensive publications have been made with focus on debris-cover glacier components or the usage of unmanned aerial vehicles (UAV) has been properly used in advantage until the latest years. The current study aims to build an inventory of supraglacial ponds and ice cliffs using a combination of aerial photography, high resolution space-born remote sensing and UAV survey from 1956 to 2023, for the purpose of understanding and estimate supraglacial ponds and ice cliffs influence to the surface elevation changes in the Tapado Glacier, using a combination of digital elevation models from tri-stereo satellites and aero photo, and 3D models generated with structure-from-motion photogrammetry acquired from UAV survey. The current study found that ponds and cliffs have consistently occupy more than 1.15% of debris-covered area since 2000 and are likely to develop in zones > 2° & < 14° surface gradient and < 1.5 ma^{-1} surface velocity. The study found that ice cliffs significantly impact lowering rates within a 15-meter radius, leading to an increase in lowering rates up to -0.48 ± 0.32 ma^{-1}. This showcased increase is ~6.53 times higher than the lowering rates observed in the debris-cover glacier. The present study identified a 2.93% omission in surface lowering, derived from tri-stereo satellite photogrammetry, within a single ice cliff. Therefore, the utilization of UAVs is recommended to attain more precise results that closely reflect changes in the Earth's surface.

Table of Contents

List of figures

List of tables

1. Introduction

High mountain regions are characterized by rugged terrain, low-temperature climate regimes, steep slopes, and institutional and spatial remoteness, being home to ~671 million people in 2010 (Jones and O'Neill, 2016) and is expected to grow to ~736–844 million across the shared socioeconomic pathways by 2050 (Gao, 2019). The cryosphere, which includes snow, glaciers, cryo-conditioned landforms, water bodies, and river ice, is an integral element of high mountain regions. Changes in the cryosphere affect physical, biological, and human systems in the mountains and surrounding lowlands. The IPCC Special Report on the Ocean and Cryosphere in a Changing Climate (2019) shows alarming observations on impacts arising from cryosphere changes in snow cover, glaciers, permafrost, natural hazards, runoff, ecosystems, and socioeconomic development.

Clean-ice glaciers, cryo-conditioned landforms (includes debris-covered glaciers, rock-glaciers and permafrost), and snow cover have been going through a widespread decline: snow cover duration has declined on average by 5 days per decade, mass change of clean-ice glaciers in mountain regions was -490 ± 100 kg $m^{-2}yr^{-1}$ (-123 ± 24 Gt yr^{-1}) in 2006– 2015, and permafrost landforms temperature has increased by 0.19ºC ± 0.05ºC during the past decade (IPCC, 2019). Consequently, winter runoff has increased due to more precipitation falling as rain, spring peaks have occurred earlier, and summer and annual runoff have increased due to intensified glacier melt – although, where glacier melt water has lessened as glacier area shrinks, it experiences a trending decrease. Regions dominated by small glaciers are especially affected by decreasing meltwater. The presented changes in the cryosphere dynamics have contributed to localized declines in agricultural yields, to reduce water quality and to impact the operation and productivity of hydropower facilities and water storage.

These current trends in cryosphere-related changes are expected to continue and the impacts to intensify throughout the 21st century. Future projections have estimated the snow depth to decrease up to 40% by 2050, the clean-ice glacier mass to reduce up to 57% by 2100 – with small glaciers losing up to 80% of their current mass and, mostly, disappearing –, the runoff will decline by the end of the century, the number and area of supraglacial water bodies will increase, etc. (IPCC, 2019). However, quantitative projections on cryo-conditioned landforms are still scarce, consisting of sparse and unevenly distributed measurements among and within mountain regions.

The mentioned cryo-conditioned landforms are a group of subsurface landforms that remain continuously below 0 °C for at least 2 years. Globally, cryo-conditioned landforms underlie between 14 – 15.7 × 10^6 km² of the global land area, which equates to ~11% ± 2% of the exposed land surface (Obu, 2021). In mountain regions, 3.6 – 5.2 × 10^6 km² are underlain by cryo-conditioned landforms, in other words, it is 27 – 29% of its global area or 14 – 21 times the area of clean-ice glaciers in these regions (Gruber, 2012). However, as subsurface landforms cannot be easily observed, their distribution and change are less understood than clean-ice glaciers, icecaps, and snow. Therefore, cryo-conditioned landforms changes and impacts can only be inferred in many mountain regions, especially in the Southern Hemisphere – as mostly of the research are conducted in the European Alps, Scandinavia, Canada, Mongolia, the Tien Shan, and the Tibetan Plateau.

Among all above mentioned cryo-conditioned landforms, debris-covered glaciers, which are characterized by a continuous cover of surface debris in their ablation zone with thickness varying from 2cm to meters thick (Briner, 2011; Westoby et al., 2020; Herreid and Pellicciotti, 2020), are one of the most predominant features in all major mountain regions (Kirkbride, 2011). A recent detailed correction of Randolph Glacier Inventory (RGI) show that on Earth's glaciers with a surface area >2 km², 44% have some debris cover (>0.1 km²), 15% have a prominent debris cover (>1.0 km²) and 20% have a substantial debris cover (>7% debris covered and/or >10 km2 of debris). Considering only the above mentioned 20% of substantial debris cover Earth's glacier, the percentage of debris-covered area is 14% (Herreid and Pellicciotti, 2020). Herreid and Pellicciotti (2020) went even further and constrained those 20% glaciers only to the ablation zone area, finding a debris-cover stage of 36%.

Globally, the distribution of debris covered glaciers is uneven, as more than half of all debris-covered ice is found in Alaska (38.6%), Southwest Asia (12.6%) and Greenland (12.0%), and exceeds 15% of glacierized area in North Asia, Central Europe, Caucasus and Middle East, South Asia East, and New Zealand. Of the mountain glacier global area, 7.3% is composed by debris covered glaciers (Herreid and Pellicciotti, 2020). Several other studies have been highlighting the prominence of debris cover in specific mountain ranges, included the Andes (e.g., Azócar et al., 2017, Barcaza et al., 2017, Wigmore and Mark, 2017, Janke et al., 2017), as the proportion of debris-covered glaciers is expected to increase as mountain glacier volumes diminish in coming decades (Rounce et al., 2021).

The altitude that debris-covered glaciers site changes regionally. In Central Europe and Middle Eastern, it is widely spready above ~2000 m.a.s.l., which ceases in altitudes higher than ~3000 m.a.s.l. and 4000 m.a.s.l, respectively. Asian debris-covered glaciers are found in higher altitudes, starting from ~4000 m.a.s.l. and reaching up to ~6000 m.a.s.l. (Rounce et al., 2021). A concise estimate of debris-covered glacier altitudes distribution in the Southern Hemisphere glaciers hasn't been made yet, as it is absent or vaguely described in several individual papers.

Although the exact glacial debris production mechanisms have not been fully understood, most investigators consider the main sources are from headwalls, sidewalls, basal erosion, and moraines, transported through landslides, avalanches, rockfalls, englacial debris loads and rocks encapsulated by basal erosion (e.g., Anderson, 2000; van Woerkom et al., 2019). Climate-debris-covered glacier system components have also been identified, such as irradiant fluxes, precipitation, debris load properties and composition, debris transport dynamics, ablation dynamics, supraglacial water bodies and ice cliffs, feedback and system coupling, and basal processes (Huo et al., 2021), despite that many important processes have not been adequately characterized.

Thus, the state and fate of mostly debris-covered glaciers in the world has not yet reached an agreement. Conflicting interpretations still arise from the lack of data and over-simplified assumptions of processes and feedback on climate-glacier system components, especially related to debris-covered glacier response to climate changes. Nevertheless, it is widely accepted that debris-covered glaciers exert important control on glacial ablation and mass balance through its capacity to insulate ice from fluctuations in air temperature where debris cover is continuous, and enhancing ablation where cover is thin and discontinuous (Fyffe et al., 2015; Westoby et al., 2020; Huo et al., 2021) and that mass loss of debris-covered glaciers is closely associated with the formation of ice-contact and supraglacial ponds or lakes that are likely to pose an increasing local hazard potential in the context of future climate projections (Benn et al., 2012).Thus, debris-covered glacier's system must receive additional attention of glaciological community due to the capacity of expanding debris cover to modify glacier mass balance and to modulate the morphology and evolution of a glacier's hydrological system, once debris-covered area will continue to expand in a warming climate (Westboy et al., 2020; Herreid and Pellicciotti, 2020, Huo et al., 2021). In this way, understanding surface ponding and ice-cliff dynamics is crucial to access the debris-covered glacier sensitivity to climate changes, since supraglacial water bodies and ice-cliffs elevate the ice loss of those glaciers and mostly likely will exhibit accelerated growth (Steiner et al., 2015; Buri et al., 2016a; Miles et al., 2016, 2018).

The number of supraglacial ponds – also known as thermokast ponds –, small and common superficial water bodies during the ablation season and in the ablation zone, has been found to be increasing on many debris-covered glaciers, which also affects water storage, drainage and englacial ablation in a glacier system (Sakai et al., 2000; Benn et al., 2001). Surface ponding and ice-cliff evolution are often a coupled-system, which plays an important role in governing the mass balance of debris-covered glaciers. Studies have shown that the ablation rates around the ponds and ice-cliffs can be more than 2 times that of most debris-covered areas and can contribute to more than 1% of total ablation (Sakai et al., 2002; Steiner et al., 2015; Buri et al., 2016b). However, many questions are still unsolved and need further investigation, including filling and draining cycles that control the evolution of many supraglacial ponds, and ice-cliff backwasting rates, especially in remotely areas that have been neglected.

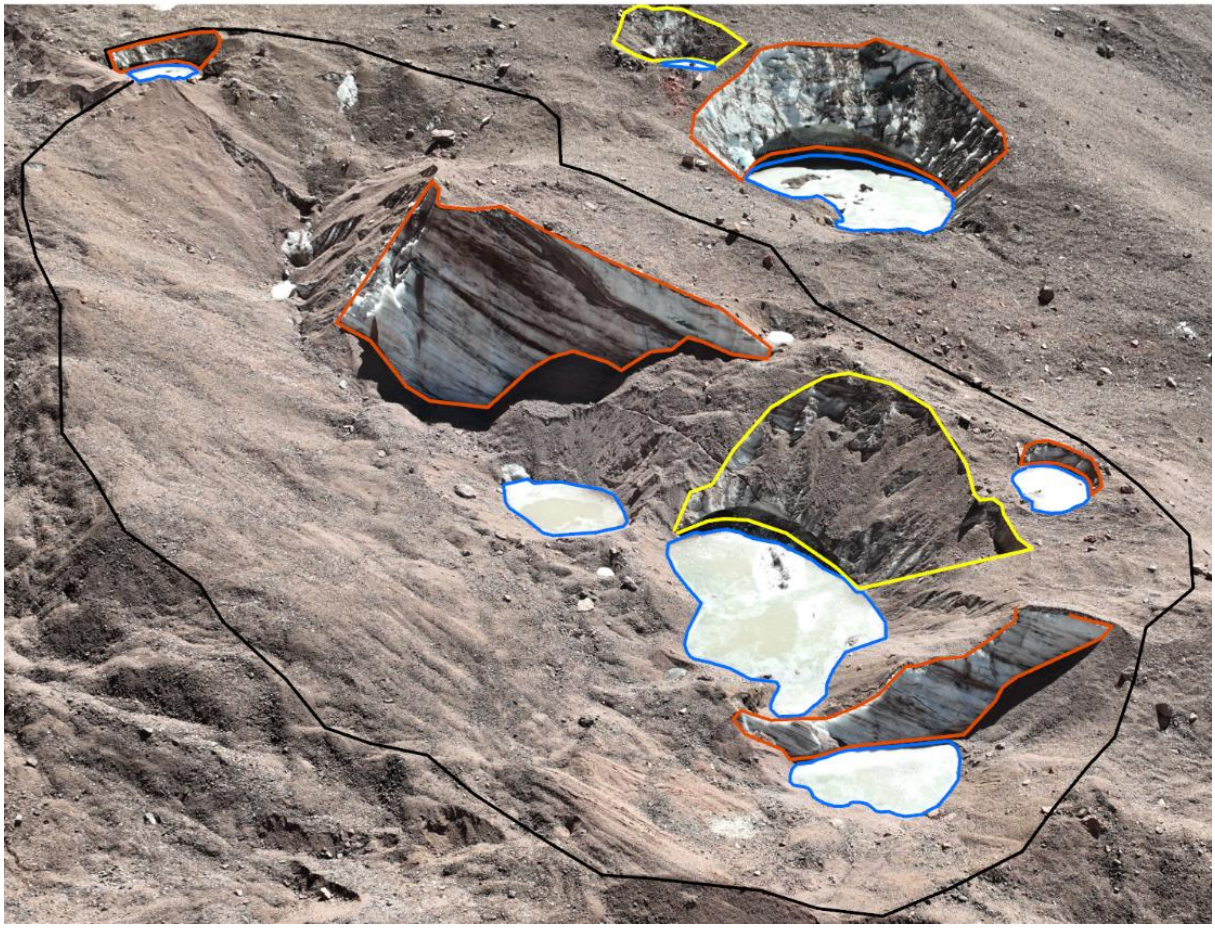

Figure 1 - Surface of Tapado debris-covered glacier showcasing its main features. The black-line comprise a thermokast depression, the red-lines consist of ice cliffs and exposed ice, the yellow-lines contain ice cliffs in development, and the blue-lines account for the supraglacial ponds. Photo by Álvaro Ayala from DJI Mavic 3E in April/2023.

In this way, remote sensing come in aid to answer those questions and has permitted a variety of studies over glacierized regions in different scale, such as broader (low and medium

resolution satellites, and aero photography), medium (high resolution satellites and aero photography) and fine (UAVs and LiDAR) resolutions. Broader remote sensing has been made possible and is generally used for glacier area and volume changes, surface elevation changes, glacial lake dynamics, runoff patterns, bed topography, surface temperature and albedo, sea-ice interactions, etc. Medium scale studies have enabled studies such as glacier flow dynamics, glacier mass balance and elevation changes, glacial hydrology pathways, debris distribution, topographic mapping, energy balance, ice velocity mapping, supraglacial pond evolution, etc. Finally, fine resolution has allowed researchers to investigate subglacial features, internal structures and layers, surface deformation, surface meltwater flow, surface roughness and texture, etc. and to solve 3D challenges in ice-cliff morphology, ice-front dynamics and calving behavior, supraglacial pond volume estimation, debris-cover thickness, etc.

To this extent, UAV remote sensing is a powerful asset to detect, measure, monitor and understand the mechanisms that govern surface ponding and ice-cliff evolution, once many of high mountain glacier forcings are too logistically difficult to regularly access in the field, its features can be too small to be mapped by broader resolution satellites, and medium scale satellites cannot solve all the challenges for volumetric analysis in three-dimensions. Furthermore, field measurements at limited sites do not describe multi-year or longer-term variations in glacier conditions, nor different spatial scales in system couplings and feedback. And conventional remote sensing platforms are limited by spatial and temporal resolutions, and by high costs in data acquisition. Consequently, UAV based studies are arising in glaciology due to its flexibility, convenience, and minimal costs.

High mountain glaciers had its first attempt to map and generate high-resolution DEMs and ortho-mosaics from UAV survey in the Himalayas (Immerzeel et al., 2014), providing a picture of the presence and dynamics supra-glacial and englacial channels and serving as a reference for other studies on glacier dynamics. Immerzeel et al. (2014) also combined, for the first time, UAV data with energy balance measurements on lakes and cliffs to understand differential melting in the debris-covered areas of a glacier. His work was succeeded by Miles et al. (2016), whose performed energy-balance modelling of a supraglacial pond on Lirung glacier, and by Kraaijenbrink et al. (2016), whose generate high-resolution DEMs and ortho-mosaics for further estimating the seasonal surface velocity. The adoption of UAV in high mountain areas fast spread worldwide (e.g., Vivero et al., 2021; Robson et al., 2022), especially in mass balance, volume estimations and surface elevation changes.

In recent years, UAVs are becoming increasingly popular in alpine glaciology, as SfM is a low cost and effective method to analyze glacier dynamics and to map glacier features. Ice cliff backwasting research has benefited the most with the usage of UAV (e.g., Buri et al., 2016a, 2021; Buri and Pellicciotti, 2918; Sato et al., 2021; Kneib et al., 2022), and revealed that north-facing cliffs are stable contributors to the melting of debris-covered glaciers, their proportion and placement on the glacier surface can change considerable in short time, and they can contribute drastically for total ablation, with studies showing annual ice loss, carried by ice-cliff backwasting, of up to 23% of total ablation. Also, other studies have shown that satellite imagery can underestimate volume loss from 3 to 7% if compared to UAV survey derived results (e.g., Brun et al., 2018). In other hand, supraglacial ponds mapping hasn't widely used UAV technology, as many recent papers still use satellite imagery (e.g., Qiao et al., 2015; Watson et al., 2016; Miles et al., 2017b; Miles et al., 2018; Chand and Watanabe, 2019), not yet taking advantage of temporal control, reduced cloud cover interference and higher spatial resolution for reduced cost.

The development of high-resolution unnamed aerial vehicles (UAV) enables highly accurate site-specific data, as high-resolution Digital Elevation Model (DEM) differencing can provide the equivalents of millions of stakes at a sufficiently high accuracy (Immerzeel et al., 2014), in real-time over short-time intervals, with stable positions, from different altitudes, and customized forward and side overlap dimensions. Also, drones equipped with specialized sensors (e.g., LiDAR or photogrammetry) can generate highly accurate 3D models of ice cliffs and their surroundings in different scales, resolutions, angles, and perspective with oblique-viewing function. These models enable detailed volumetric calculations and better understanding of ice cliff morphology coupled with SfM techniques.

Thus, UAV-based remote sensing filled the gap created by the lack of multi-viewing satellite remote sensors, customized stereo satellite spatial and temporal resolution and by the absence of reliable ground control points (GCPs) in high mountain areas, making available imagery at sub-centimeter resolution and with high positional accuracy from different angle-views. It also has the potential to bridge the gap between sparse and discontinuous field observations and continuous but coarser resolution space-borne remote sensing.

In such manner, remote sensing studies with focus on UAV-based monitoring can be an important platform to study Tapado Complex in Chile, an important source of meltwater for the large population residing in the downstream basin. The Tapado Complex is the principal glacier

in the catchment of Coquimbo-La Serena in the semiarid Andes (SA), region characterized by low precipitation at the coast and precipitation as snow in higher elevations even during summer. Thus, cryosphere dynamics, the movement and behavior of ice and snow, is the most important component for the hydrological system and streamflow in the region with glaciers working as water storages. Consequently, the water supply for this catchment is highly dependent on melt from seasonal snow and ice bodies from the Tapado Complex.

Cryosphere dynamics research in Tapado Complex, then, come in urge, as total precipitation has declined over the 21st century (Santibañez 1997; Vuille and Milana 2007) and desertification has been recognized internationally as a critical problem in the SA, according to the United Convention to Combat Desertification (1994). Adding to the poor water distribution, the densely populated regions and the agricultural activities in the catchment, estimations of ablation rates, mass balance, sublimation rates, ice flow, etc. have been strategical for government policies and actions. Hence, the Centro de Estudos Avanzados de Zonas Áridas (CEAZA) has been exploring the cryosphere in the Tapado Complex in the later years with excellence.

However, it is still well unexplored by drones and publications focused mostly on geomorphology of the complex, drainage pathways, penitentes, clean-ice glacier dynamics, and rock glaciers. In the past five years, UAV research has been implemented, as it is easily explored by drones due its small size not requiring different flying routes to different blocks, neither requires placing the differential global position system (DGPS) at different locations, and due to factors, such as inaccessible high elevation, underlying terrain, and year-round rough weather conditions. In other hand, debris-covered glaciers mass balance, nor supraglacial ponds dynamics and ice cliff backwasting, haven't gotten much attention yet.

Thus and so, this master's thesis aims to build an inventory of supraglacial ponds and ice cliffs using a combination of aerial photography, high resolution space-born remote sensing and UAV survey from 1956 to 2023; to estimate selected ice cliffs surface changes in 3D, using dense point cloud derived from UAV survey from 2019 to 2023; and to access how supraglacial ponds occurrence and ice cliff development relates to surface elevation changes using generated DEMs in comparison with Tapado Glacier and debris-covered glacier lowering. In prospect, the results can contribute to improve the understanding of debris-covered glacier system dynamics at global and local scale, to acquire more data related to supraglacial water bodies and ice-cliff influence on glacier ablation, to contribute to high mountain glacier hydrology research, to

provide inputs for numerical modelling, and to propagate the usage of UAV remote sensing in glaciological studies.

2. Study site

2.1 Geographic location

The La Laguna catchment (30°11′ 53″S, 69°56′15″W), situated at the headwaters of the Elqui River catchment, in between ~3500 and 6216 m a.s.l., englobes an area of ~140 km² (Robson et al., 2022). The Tapado Glacier (5536 m.a.s.l.) is the main glacier in the catchment, located in the Río Colorado basin at the head of the Elqui River catchment in the semiarid Andes of Chile (30°08′ S, 69°55′W), capped with the largest (~1.26 km²) glacier of the Elqui catchment (Monnier et al., 2014). The wider Tapado Complex also includes two rock glacier tongues (~0.85 km²), totaling ~2.1 km² of glaciers within the Tapado glacier-rock glaciers.

2.2 Geology and geomorphology

Tapado Complex sites on the South slope of the large glacial cirque and its bedrock are composed of dacitic and rhyolitic materials from upper Paleozoic–Lower Trias and upper Oligocene–Lower Miocene periods (Strauch et al., 2006). In the north-eastern half of the cirque, a debris-covered glacier tongue followed by cryogenic rock glacier tongue extends for 1.2 km from 4250 to 4530 m.a.s.l., while in the south-western half of the cirque, in the continuity of clean-ice glacier, the debris-covered tongue followed by a glaciogenic rock glacier tongue extends for 2 km from 4250 to 4700 m.a.s.l. (Monnier et al., 2014). The debris-covered glacier is characterized by a trident-like shaped tongue with large exposures of ice-cliffs in supraglacial ponds and by rather chaotic hummocky moraines (Monnier et al., 2014). Areas of the catchment above 4500 m.a.s.l. are likely to display continuous permafrost conditions, whereas areas between 3900 and 4500 m.a.s.l. permafrost is probably more scattered (Azócar et al., 2017).

Monnier et al. (2014) identified six main spatial units in the landform assemblage, extending downslope from the glacier front: (i) an upper latero-frontal moraine complex, (ii) an upper debris-covered glacier, (iii) a lower debris-covered glacier, (iv) a first rock glacier, (v) a second rock glacier, and (vi) a lower latero-frontal moraine complex. The upper debris-covered glacier is divided between a vast central area and a marginal and prominent belt of composite moraine ridges, which marks the outer boundary of the upper debris-covered glacier and its piling-up onto the lower debris-covered glacier. The two debris-covered glaciers present typical features, such as irregular set of thermokarst depressions and supraglacial ponds, massive ice exposures, closed crevasses, and hummocky moraines. The walls of the thermokarst depressions often

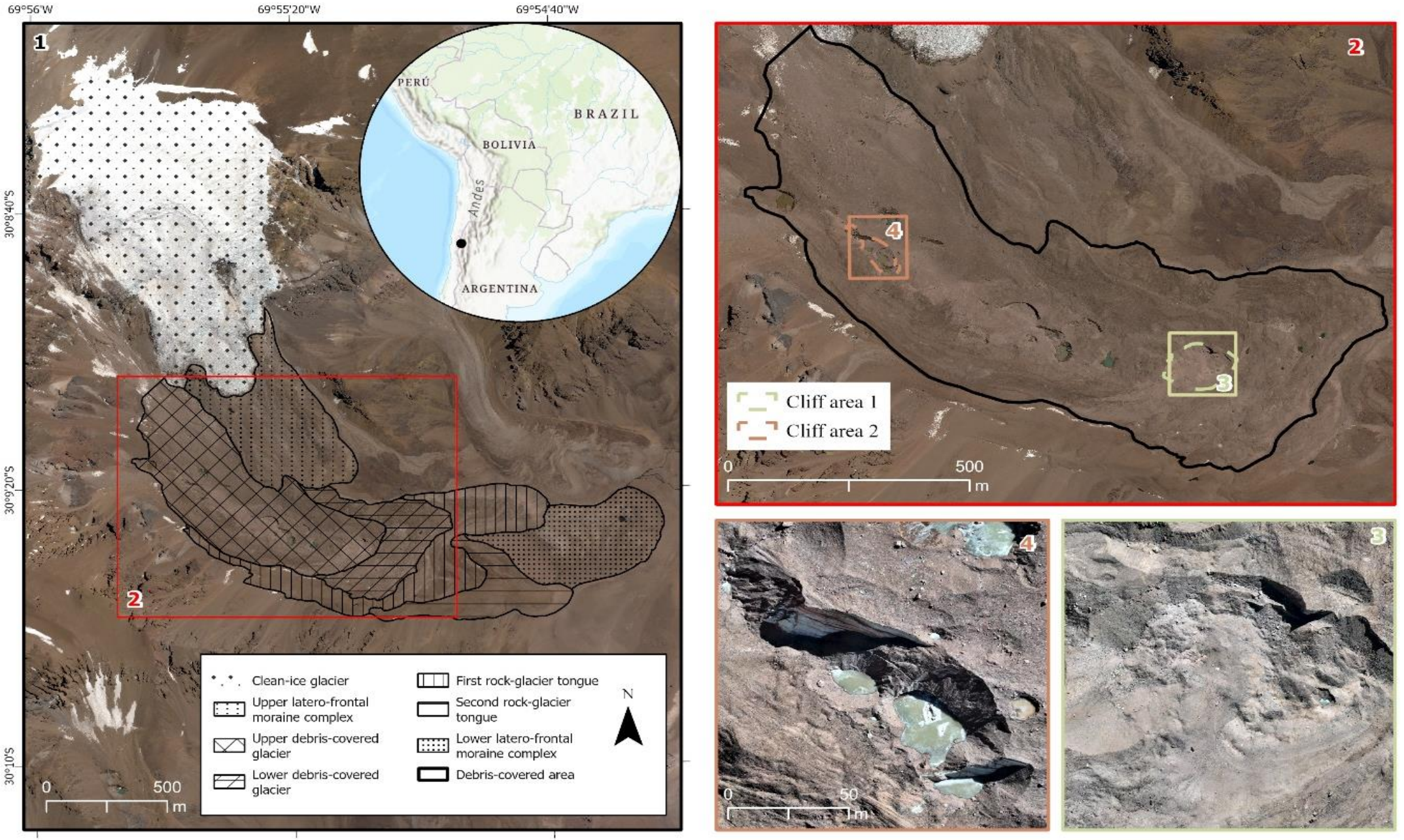

Figure 2 - Location of Tapado *Complex and* its landforms. The three main landforms that will be discussed in the thesis are 1) Tapado Complex-, 2) debris-covered glacier (upper and lower debris-covered glacier*) pinpointing ice cliffs in Area 1 and Area 2,* 3) *Area 1 representing UAV survey thermokarst depression from 2019 to 2020, and 4) Area 2 representing cliffed area surveyed in 2022 and 2023*. Sources: 1) Pléiades imagery (2023), 2) Pléiades imagery (2023), 3) Ayala, A. (2023) field work with DJI Mavick 3E.

exhibit exposures of glacier ice, up to ~30 m high and ~50 m wide, with well visible structural features such as stratification, debris inclusions, thrusting, and folding; the hummocky morphology also exhibits frequent but somewhat smaller ice exposure (Monnier et al., 2014).

The National Water Directorate of Chile (DGA, 2010) monitored vertical displacements between -0.01 and -2.00 ma^{-1} within the debris-covered and rock glaciers. Between 1956 and 2010, the upper debris-covered glacier shows the largest surface displacements, up to 85 m. In the time, the lower debris-covered glacier moved slower, with displacements up to 45 m (Monnier et al., 2014). Thermokarst depressions were tracked in the period and show clear and significant displacements, as well as evolution, including closing, opening, or even joining of depressions over time.

2.3 Climatic setting

The Chilean semiarid Andes (SA) (29°S, 34°S), a transition zone between the extremely arid region north (25°S) and the humid climate south (40°S) (Escobar and Aceituno, 1998), is characterized by low atmospheric pressure, low air densities, high solar radiation, and minimal atmospheric humidity (MacDonell et al., 2013, Navarro et al., 2023). This zone involves a low annual precipitation rate near the coast (80 mma^{-1} at 30°S) and a slightly higher rate on the windward slope (150 to 200 mma^{-1} at 30°S) (Álvarez-Garretón et al., 2018; Falvey and Garreaud, 2007; Favier et al., 2009), with a mean annual orographic precipitation gradient of 6.3 mm km^{-1} in elevation at 30°S (Scaff et al., 2017). In those high-altitude regions, precipitation predominantly falls as snow, due to constantly low temperatures (Favier et al., 2009), even during summer season.

Interannual and seasonal variability in precipitation episodic events are associated with the Pacific Decadal Oscillation (PDO) and El Niño Southern Oscillation (ENSO) (Navarro et al., 2023). During positive-warm phases, higher precipitation is related to El Niño years, and is more pronounced during austral winter (May to August). This scenario occurs because of the influence of the westerly winds and the South Pacific High (Falvey and Garreaud, 2007), which allows cold frontal systems coming from the southwest Pacific to penetrate the continent (Navarro et al., 2023). During cold-negative phases, lower precipitation is related to the La Niña years, and the coast of Chile suffers severe drought. This happens as westerly winds currents blow warm water at the Pacific Ocean's surface towards Asia, cold water from the deep sea rises

to the surface near South America (Escobar and Aceituno, 1998). PDO phases are like ENSO patterns, however, in a long-lived cycle, being able to bulky or attenuate ENSO anomalies.

La Laguna meteorological station, located at ~3100 m a.s.l. and ~15 km to southwest of the study site, recorded a mean annual precipitation of 167 mm (1970-2009), and a mean annual air temperature (MAAT) of 8 °C (1974–2011). The 0 °C MAAT isotherm is located near 4000 m a.s.l. (Brenning, 2005; Ginot et al., 2006). A warming trend of 0.17 °C decade−1 in the MAAT was calculated at the La Laguna station for 1974–2011. Total precipitation has declined over the 21st century (Vuille and Milana 2007) and desertification has been recognized internationally as a critical problem in the SA (UNCCD, 1994). Additionally, due those to arid conditions, sublimation rates are relatively high, specially at high elevation where melt rate stagnates (Navarro et al., 2023).

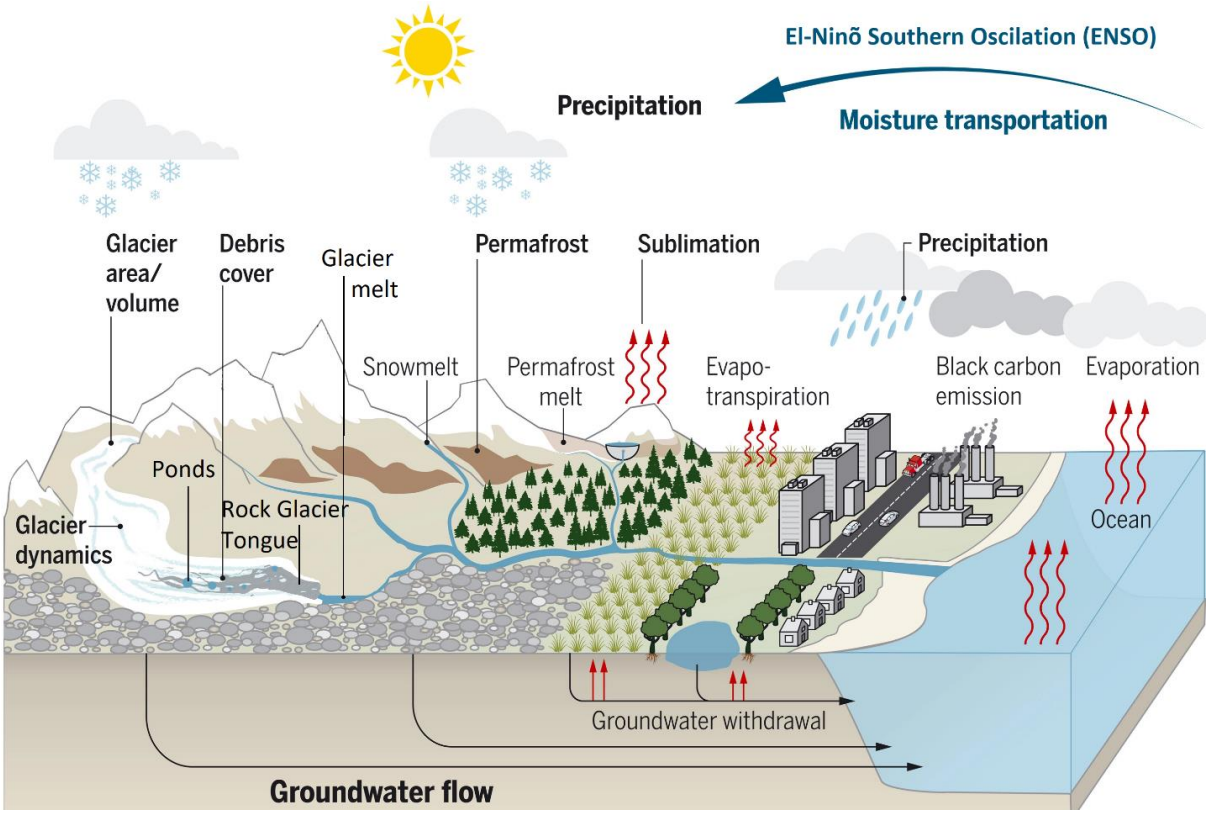

Figure 3 - Representation of major Earth's cryosphere system processes in high mountain areas adapted to Tapado Complex climatological context. Source: Adapted from Azam et al., 2021.

2.4 Hydrological system and streamflow

The main components of the hydrological system in high-altitude glaciers are snow, ice bodies, groundwater, high-altitude wetlands, and surface stream (Navarro et al., 2023). In the SA, the most important contributor to total annual runoff is snowmelt (Favier et al., 2009), specially

during autumn-winter season; which is controlled by frequency and intensity of the front, topography, wind distribution, avalanching, sublimation, albedo variability and anthropogenic activities (Hue et al, 2021; Navarro et al., 2023).

However, as snow cover only lasts 1 to 2 months after the last winter snowfall (Favier et al, 2009), during dry periods ice is exposed to extreme weather conditions (i.e., irradiant fluxes) due to the lower income of snow, thus glacial ice melt turns to be an important contributor to streamflow (Favier et al., 2009). At high altitudes, above ~4000 m a.s.l., sublimation is an important process, contributing between 46 to 90% of total ablation (MacDonell et al., 2013). This sublimation process originates ice spikes-shaped features, commonly known as penitentes, preserving snow cover from melting, as non-linear ablation loses water content to the atmosphere (Sinclair and MacDonell, 2016).

In this system, debris-covered glaciers and rock glaciers act as natural reservoirs, storing frozen water and releasing it slowly (Azócar and Brenning, 2010). In the SA, cryo-conditioned landforms represent an important long- and short-term hydrologic unit (Pourrier et al., 2014), capable of provide quite persistent flows throughout the year with higher relative contributions during dry seasons (Navarro et al., 2023). In the La Laguna catchment glaciers and rock glaciers are estimated to contribute between 4%–13% to the annual streamflow (Favier et al., 2009; Pourrier et al., 2014; Schaffer et al., 2019), while Tapado catchment was estimated to contribute 13 ± 20% this upstream watershed (Pourrier et al., 2014).

Subsequent hydrological processes are surface and subsurface runoff and storage of water that flows through pathways available in the landscape as supraglacial or englacial streamflow, or quick flow (Navarro et al., 2023), due the impermeabilization of glacial landforms by ice layers. Those flows can arise as supraglacial ponds due the blockage of conduits connectivity by impermeable layers of ice, or to sum up incoming groundwater flow and cryo-conditioned landforms meltwater, eventually reaching aquifers and rivers. The aquifers, particularly, constitute one of the most reliable hydrological reservoirs in arid and semiarid areas, due to its long hydrological memory that allows the release of water stored in previous winter precipitation (Álvarez-Garretón et al., 2021).

2.5 Area changes, lowering and mass balance

Robson et al. (2022) analyzed the wider Tapado complex's area changes, surface lowering and geodetic mass balance between 1956 and 2020. They conclude that Tapado Glacier's area

shrank by a total of −25.2 ± 4.6% (−0.42 ± 0.23 km²) at a mean rate of −0.40% ma^{-1}. Between 1956 and 1978 the glacier area reduced −0.35 ± 0.30% ma^{-1}, which increased to −0.60 ± 2.28% ma^{-1} between 2000 and 2012 and to −1.03 ± 2.19% ma^{-1} between 2012 and 2015. Between 2015 and 2020, losses decreased to −0.16 ± 2.77% ma^{-1}. The clean ice section of Tapado Glacier has seen greater changes, shrinking from 1.30 ± 0:01 km² in 1956 to 0.93 ± 0:01 km² in 2020, a change of −28.4 ± 1.1% ma^{-1}.

In the above-mentioned paper (Robson et al., 2022), Tapado Complex has lowered by an average of –7.44 m between 1956 and 2020. The clean-ice glacier and the debris-covered glacier presented the great thinning rates, with a mean annual loss of –0.64 ± 0.11 ma^{-1} and –0.44 ± 0.11 ma^{-1} between 2012 and 2020, respectively. Although, the rock-glacier showed slight thinning rates of –0.08 ± 0.11 ma^{-1}. The upper debris-covered glacier had the biggest thinning rates of by ~0.7–0.8 ma^{-1}, while the lower debris-covered glacier lost 0.3–0.5 ma^{-1}, although thinning rates are greatly enhanced within the vicinity of supraglacial lakes and ice cliffs, with rates of up to 2 m a–1. The results (Robson et al., 2022) also showed that Tapado Glacier has consistently had a negative geodetic mass balance over the entire 64-year period, with a mean mass balance of –0.11 ± 0.05 $m.w.e.a^{-1}$. The glacier mass balance was most negative in recent times, with a mean of –0.54 ± 0.10 $m.w.e.a^{-1}$ from 2012 to 2015, and –0.32 ± 0.08 $m.w.e.a^{-1}$ from 2015 to 2020.

The National Water Directorate of Chile (2010) also monitored vertical displacements withing the Tapado Complex, from 1956 to 2010, with values in between −0.01 and −2.00 ma^{-1}. Monnier et al. (2014) summarized those results, observing most pronounced surface lowering (−60 m) in the limit between the clean-ice tongue (upper-lateral frontal moraine) and upper debris-covered glacier. In the thermokarst area (depressions, supraglacial ponds, and ice-cliffs) of the upper debris-covered glacier, marked downwasting in between 20–40 was observed. Within the lower units of the study site (lower debris-covered glacier and rock glaciers), moderate downwasting of 5–10 m was pointed out in the central parts of the rock glacier tongs, and moderate surface rising of 5–15 m was identified along the boundaries between units. Moraine ridges, in general, presented surface rising of 5–10 m throughout the area.

2.6 Human and economics aspects

The water resources in Chile are not evenly distributed. In semiarid and arid regions from the Metropolitan Region of Santiago to the north (~18°–34°S), the total water supply is ~ 500 m³

person^{-1}yr^{-1}, while between Santiago and the Austral Macrozone (~34°–44°S), the water supply is ~ 53,900 m^3 person^{-1}yr^{-1} and in the Austral Macrozone (~44°–56°S), the water supply is ~2,444,600 m^3 person^{-1}yr^{-1} (DGA, 2016). The population density, respectively, is 91, 36 and 1 hab. km$^{2-1}$ (DGA, 2016). The zones of limited water resources from Santiago to the north also correspond to areas with significant agricultural development, and extensive mining activity (Schaffer et al., 2019).

The Elqui River catchment has a total population of over 230,000 people, an agricultural production worth USD 40 million a year, and water dependent industry such as mining (Cortés et al., 2012), in which most human and agricultural development is concentrated in the valleys, while the mountainous terrain is largely unpopulated or unused, except for mining operations (Schaffer et al., 2019). Water supply for these sectors is largely reliant on melting from seasonal snow and ice bodies from the Andean Cordillera (Favier et al. 2009; Azócar and Brenning 2010). For a large portion of the semiarid region of Chile, the water supply has already been exhausted (DGA, 2016), placing water availability in a precarious position as the demand for water resources is expected to rise in the future (Meza et al. 2015).

3. Supraglacial ponds, ice cliffs, and their influence on glacier mass balance

3.1 Supraglacial ponds

Supraglacial ponds, also known as proglacial or thermokarst ponds, on debris-covered glaciers have gained significant attention in recent years due to their potential influence on glacier melt rates and hydrological processes within the cryosphere. They are a common feature on the surface of glaciers covered with a layer of debris, as in figure 4. On Tapado Complex, surface water body features range from small puddles to larger ponds, however they can develop to large lakes spanning several kilometers, as seen in other debris-covered glaciers in the world. They are a temporary feature that occurs when meltwater collects and accumulates in depressions or crevasses on the glacier surface, linked to warming temperatures, negative glacier mass balance, and relatively slower ice velocities (Röhl, 2008).

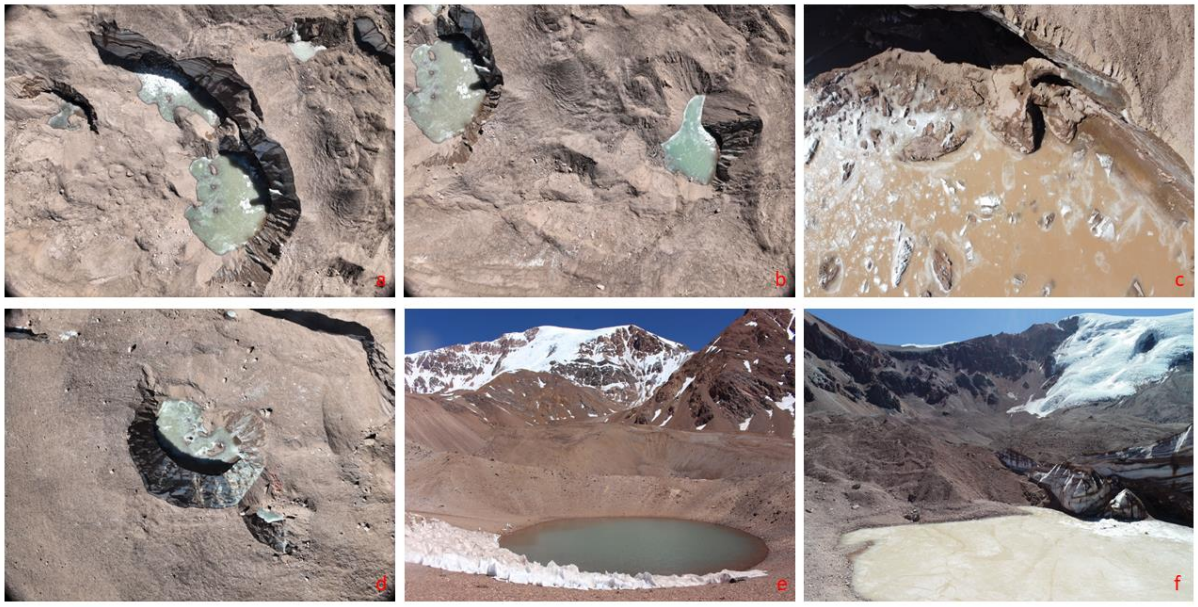

Figure 4 - Supraglacial ponds on debris-covered glacier on Tapado Complex. Figure shows a and f) supraglacial pond in contact with ice cliff; b) supraglacial pond in thermokarst depression going through ice cliff development; c) supraglacial pond in contact with ice cliff going through calving events; d) supraglacial pond on the crest of ice cliffs; e) supraglacial pond in thermokarst depression without the presence of ice cliffs. Source: UAV and field photos from December 2022.

Supraglacial pond formation starts with the disruption of the insulating debris mantle by thermokarst erosion (Figure 5), in which thermokarst depressions that exploit the pre-existing

englacial drainage network are triggered. The subsequent development of surface ponding is knowingly associated to inefficient glacial meltwater drainage, lower surface gradient, enlargement of conduits down-glacier, increase of glacier ablation budget and non-linear mass balance profile with elevation. One of the most noticeable forms of pond expansion and largest component of ice loss is the back-melting of the surrounding walls (fig. 4a, 4d, 4f), caused by ongoing pond ice edge calving in conjunction with substantial subaqueous melt, once originated by englacial conduit collapse (Miles et al., 2016). Watson et al. (2017) note that ponds bordering a cliff were much larger than other ponds, same statements were made by Loriaux and Ruiz (2021) for Verde Glacier in Chile and by Röhl (2008) for Tasman Glacier in New Zealand.

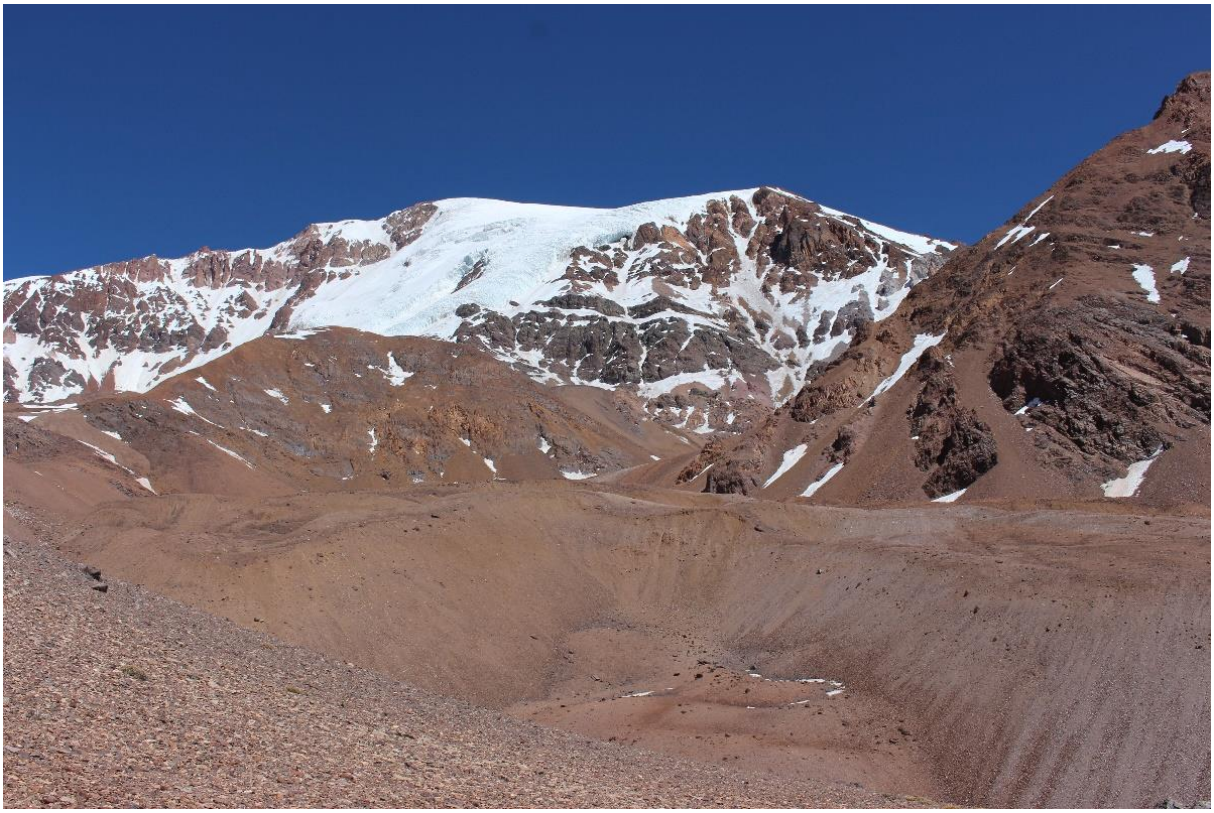

Figure 5 - Thermokarst depression on Tapado Complex without the presence of supraglacial ponds or ice cliffs. Source: Field work, dec 2022.

The position of englacial conduits is responsible for the hydraulic connection of the englacial drainage system, determining the efficiency of glacial meltwater drainage and developments of ponds (Röhl, 2008). Such supraglacial ponds can experience repeated filling and drainage, as englacial conduits are the dominant drainage route for supraglacial ponds (Miles et al., 2017a). Sakai et al. (2000) related the drainage dynamics of supraglacial ponds, especially the ones observed during melting season, to the thermal enlargement of their drainage channels and lowering of their floors – due englacial conduit collapse which could also create further ponds,

and concluded that enlargement of englacial conduits happens because at least half of the heat absorbed at the surfaces of ponds is released with outflow and its delivery is focused to the ice underneath.

The formation and size of supraglacial ponds are heavily marked by seasonal changes (i.e., meltwater generation, englacial inputs and drainages, and precipitation input), englacial base water level, topography gradient, and surface velocity that resonates in surface lowering and increased glacier stagnation. Thus, supraglacial ponds are classified in accordance with seasonality, water base level, surface gradient and surface velocity.

Some attempts to measure the influence of seasonality and climate on ponding have been made, Steiner et al. (2019) estimated a difference of 1% in pond cover from dry to wet season in the Langtang Glacier, and Zhang et al (2015) observed that smaller ponds are more sensitive to climate changes. Watson et al. (2016) showed that without exception there were more ponds evident, increased ponded area and cumulative area distributions during summer periods than during the preceding winter, as pond development proceeds alongside sporadic drainage events from accumulated snow and ice during winter season. The localized melting of ice due uneven distribution of debris activates smaller basins, therefore, enhancing meltwater generation and increasing pond connectivity with englacial drainage system (e.g., Sakai et al., 2000; Miles et al., 2016).

Sakai et al. (2000) correlated fluctuations in water level to pond surface area and depth, as water received by ponds from surrounding surface watershed and the discharged water through englacial conduits varied according to changes in water level. The same research also correlated smaller water balance changes to the presence of glacial lakes, as the water level is controlled by them. Röhl (2008) found that ponds reaching the englacial base water level tend to grow progressively and classified supraglacial ponds in debris covered glacier based to the water level as:

a) perched ponds that lie above the level of the englacial drainage system,
b) ponds that are hydraulically connected to the main drainage system at the same base water level,
c) ponds that are in the active part of the drainage system with noticeable currents.

Perched lakes are, therefore, ephemeral features that undergo cycles of expansion and drainage. Meanwhile, Benn et al. (2001) constated that the growth of perched lakes on the glacier surface is self-limiting, and although they contribute to thinning of the glacier, they are unlikely to evolve directly into large (>1 km) moraine-dammed lakes.

Reynolds (2000) proposed a glacier classification based on their surface gradient influence on the formation of dispersed ponds, in which glaciers with gradients in the range of 2°-6° are expected to experience widespread dispersed ponding and those in the range of 6°-10° expected to exhibit isolated small ponds. Sakai and Fujita (2010) complemented this classification stating that glacier terminus with surface gradient lower than 2° is prone to develop large terminal lakes. Quincey et al. (2007) concluded that surface lowering results in an overall reduction of the surface gradient in the ablation area, also reducing driving stressed and flow speed, contributing to the development of dammed moraine lakes.

Previous studies showed already that supraglacial pond development is most likely where the glaciers have a low slope angle and a low flow velocity or are stagnant (e.g., Reynolds 2000; Quincey et al., 2007; Liu et al., 2013; Chand and Watanabe, 2019; Taylor et al., 2021; Loriaux and Ruiz, 2021). Bolch et al. (2008) analyzing glacier surface flow rates of the Khumbu, Imja and Lhotse Nup Glaciers, determined that low surface flow or stagnant ice is indicative of the future formation of supraglacial ponds and glacial lakes. That occurs because ice accumulates in depressions or low-lying areas on the glacier's surface, acting as natural basins for the pooling of meltwater – in contrary, rapidly flowing glaciers may transport meltwater away more quickly, preventing the development of supraglacial lakes.

Although there is impressive literature on pond dynamics, those processes on smaller glaciers are less understood. Bolch et al. (2008) has not found any clear trend in spatial distribution of ponded area on the smaller glaciers in the study area, Watson et al. (2016) found that surface water storage is much more variable in small glaciers. Understanding the dynamics and implications of supraglacial ponds on debris-covered glaciers in small glaciers – the most endangered by climate changes – is vital for predicting future glacier behavior and assessing water resources in glacierized regions. Further research is needed to investigate the spatial and temporal distribution of supraglacial ponds, their connectivity, and their influence on glacier dynamics and downstream water availability.

Researchers have also correlated supraglacial pond presence to ablation zones and to increasing melt rates on the glacier. That is because incised supraglacial channels are common across the upper ablation zones of debris-covered glaciers, but the low gradient and dense undulations typical of the lower ablation zone greatly impede water flow, leading to ponding and water storage in closed surface depressions. (e.g., Sakai et al., 2000; Benn et al., 2001; Watson et al., 2016; Miles et al., 2017b). Sakai et al. (2000) and Watson et al. (2016) linked the pond size distribution to the evolution of debris-covered glaciers under negative mass balance, pointing out the consequent implications for the positive-feedback enhancement of melt, in and around the pond environment.

Thus, increased ablation budget of the negative mass balance increases melting, and the non-linearity concentrates those melting in critical zones. Miles et al. (2017b) observed a contribution of 12.5 ± 2.0% of mass loss originated from supraglacial ponds and Lamsal et al. (2017) affirmed that ponds enhance localized ice wastage.

Therefore, these ponds act as storage reservoirs, as they accumulate meltwater during the summer season. In this way, area measurements of supraglacial ponds are extremely important as a proxy for water storage and glacier ablation potential (e.g., Liu et al., 2015; Zhang et al., 2015), for example, Stefaniak et al. (2021) accounted that supraglacial pond stores 8% of total water volume at the Miage Glacier in Italy. As ponds grow, they can interconnect and form a network of channels and drains through which water flows, contributing to the overall meltwater output from glaciers and affecting downstream water availability and hydrological regimes.

3.2 Ice cliffs

Ice cliffs are vertical or near-vertical walls of exposed ice that form on the surface of debris-covered glaciers, as seen in Figure 6. They typically arise from the exposure of glacier ice by localized debris slumping, by the exposure of ice at the margins of supraglacial lakes and by the collapse of englacial conduits (Watson, 2017). Despite the small areal coverage of ice cliffs, estimates of their contribution to glacier mass loss are often substantial, but highly variable (Benn et al., 2001, Watson, 2017).

Previous studies have shown that independent from ice cliffs small percentual of covered area, they are responsible for high values of thinning rates. Buri et al. (2021) ice cliffs cover 2.1% ± 0.6% of debris-covered tongues but cause 17% ± 4% of their annual ice loss in Lirung and

Langtang Glaciers, while Brun et al. (2016) measured a glacier ablation rate on ice cliffs to be 6 times higher than the average glacier ablation rate over the same area. On Miage Glacier, in Italy, Reid and Brock (2017) accounted ice cliff ablation for 7.4% of total ablations. Brun et al. (2018) identified it to be 23% for Changri Nup Glacier in Nepal. Thompson et al. (2016) related 40% of total ablation to ice cliffs in the Ngozumpa Glacier, Buri et al. (2021) correlated 17% of mass loss to ice cliffs in the Langtang Valley, and Kneib et al. (2021) said that average melts on ice cliffs at Langtang glacier can be up to 14 times higher than the surrounding debris. In the Cordillera Blanc, Peruvian-Andes, Wigmore and Mark (2017) also associated ice loss to ice cliff presence.

The formation of ice cliffs is facilitated by the presence of supraglacial ponds and debris, which act as amplifiers of melting processes on the glacier surface (Benn et al., 2012). As supraglacial ponds absorb solar radiation and debris emit longwave radiation, they experience higher energy inputs compared to surrounding ice, leading to increased melting (Buri et al., 2016). The melting process enlarges existing crevasses or triggers the development of new fractures (e.g., conduit collapse), resulting in the creation of ice cliffs (Benn et al., 2012).

The insulating effect of debris cover creates an uneven ice surface topography, with the formation of ridges and depressions, where supraglacial ponds tend to accumulate. The ponded water acts as a lens, focusing solar energy onto the underlying ice, especially if considered season drainage cycles, accelerating ablation and preferential melting (Buri et al., 2016). Furthermore, as supraglacial ponds expand, the increased water pressure within the crevasses can induce fracturing and calving events (Benn et al., 2012). The pond-induced melting contributes to the growth and vertical expansion of ice cliffs, in which the calved ice exposes fresh, vertical ice walls.

Therefore, ice cliff backwasting is the result of those melting processes and mechanical forces acting on the retreat and erosion of pre-existent ice cliffs in debris-covered glaciers. Size and depth of supraglacial ponds, duration of pond presence during the melt season, englacial hydrological connections, aspect and orientation of the ice cliff, and depth of debris-cover layer influence the rates of ice cliff backwasting in debris-covered glaciers. These factors can vary spatially and temporally, leading to variations in backwasting rates across different regions and time periods. Additionally, backwasting of ice cliffs can produce accountable meltwater generation to the total melt runoff from the debris-covered area.

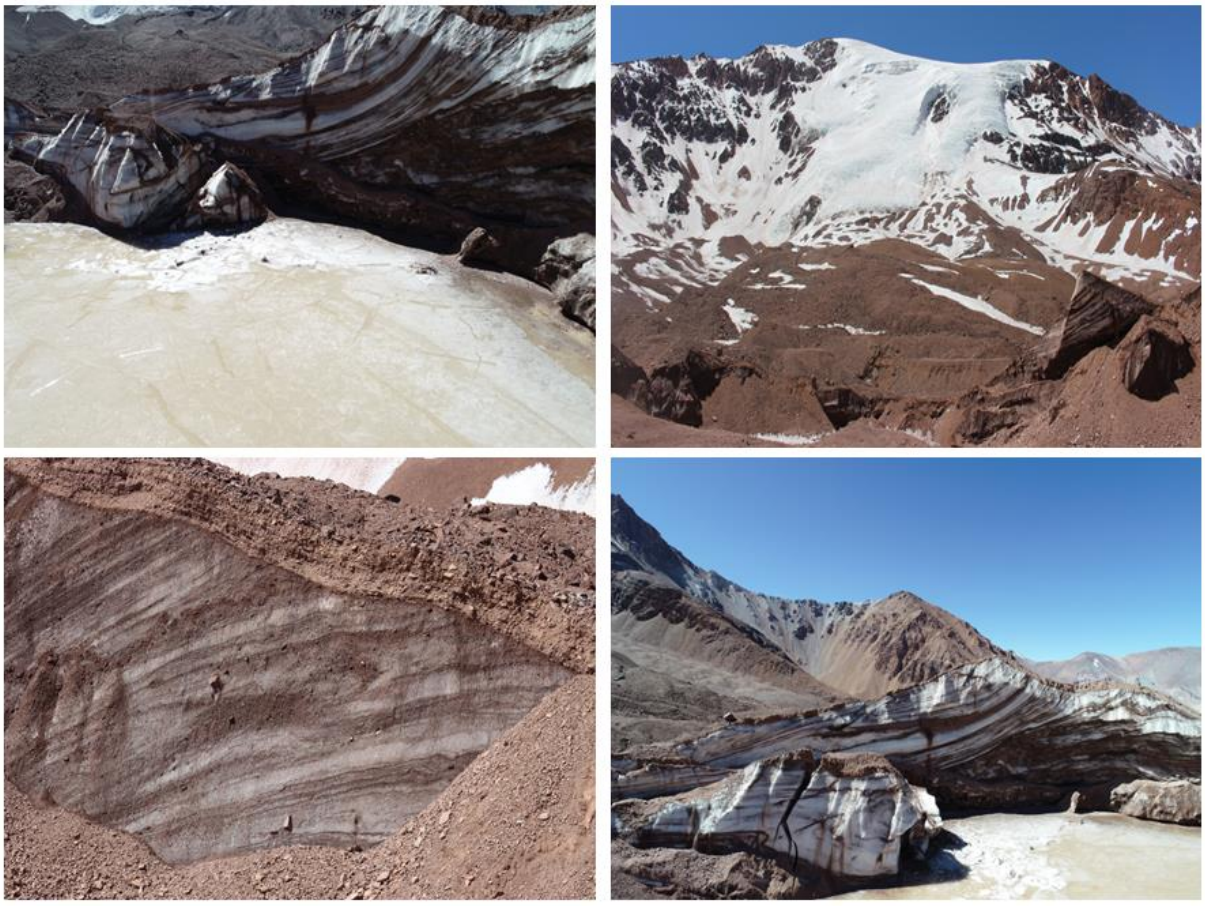

Figure 6 - Ice cliffs on debris-covered glacier on Tapado Complex showing exposed ice and thermokarst depression with and without contact of supraglacial ponds. Source: Field Work.

Buri et al. (2016) classified cliff behavior in three categories regarding pond presence: reclining cliffs, persistent cliffs and expanding cliffs. Reclining cliffs happens in absence of pond contact, which permits flattening of the cliff and causes continuous cliff reclining as fast drainage of ponds removes the steep sections from the cliff's base and the reduced ice volume from positive feedback on glacier ablation lowers cliff's top ridge (Buri et al., 2016). On the contrary, consistent pond presence, when ponds are filled slightly and then drained gradually, leads to steep sections at the cliff base, enabling a stable cliff geometry (Buri et al., 2016). Last, partial pond drainage markedly promotes cliff shape and geometry changes, thus, lowering pond water level reveals steep formerly submerged ice in a cliff that grew radially in size (Buri et al., 2016).

Cliffs have also been classified regarding aspect and orientation. Sakai et al. (2002), Steiner et al. (2015), Buri et al. (2016) and Watson (2017) related cliff survival over multiple seasons to cliff facing. On the Northern Hemisphere, a higher solar radiation receipt on south-facing cliffs is expected to cause their rapid decay and burial under debris following progressive slope angle lowering, which may explain why few south-facing cliffs are observed (Sakai et al., 2002;

Watson, 2017). In contrast, ice cliff persistence is likely to be favored on shaded north-facing slopes, as high longwave radiation input at the cliff base and low direct solar radiation input at the Cliff top appears to maintain a steep cliff angle (Sakai et al., 2002; Steiner et al., 2015; Buri et al., 2016).

Larger and deeper ponds have a larger surface area in contact with the ice cliff, leading to greater heat transfer and enhanced melting. Size and depth of ponds also affect the water pressure within crevasses, influencing the likelihood of calving events and ice cliff collapse. Calving events led by pond-cliff interactions were classified by Kirkbride and Warren (1997). Waterline calving is frequent but small events occur close to the waterline and remove several cubic meters of ice. Flake calving removes large quantity of ice from the cliff face, while in full-height slab calving detachment of large volumes of ice through the development of crevasses at the cliff top are involved. Then, subaqueous calving is when submerged ice foot develops below the zone of greatest undercutting.

In conclusion, ice cliffs and ponding are of particular interest in Tapado Glacier in Chile, due to their potential to accelerate ice melt and contribute to glacier wastage, destabilize the glacier by localized thinning and weakening of ice at the base of ice cliffs, and increase the risk of ice avalanches or glacier collapse by hydrofracturing. The positive feedback of ice cliffs and supraglacial ponds, i.e., ponds creating new cliffs that develops into new ponds and cliffs (Sakai et al., 2009), are responsible for the markedly mass loss that occurs below supraglacial debris (i.e., subaqueous melting and enlargement of conduits) and melt and calving of ice cliffs.

4. Remote sensing and UAVs

Remote sensing has played a crucial role in advancing glaciology by providing valuable insights into the dynamics and changes of glaciers. Over the years, both 2D, 2.5D and 3D remote sensing techniques have contributed significantly to our understanding of glacial processes and their responses to environmental factors.

In the early stages of glaciological remote sensing, 2D techniques in broader and medium scales were widely used, with the aid of sensors such as Landsat, Skylab, ERS, cameras attached to airplanes or even passive microwave sensors, like Nimbus. Those low and medium resolution sensors pivot the way for the remote monitoring of glacier area extent and changes (e.g., Meier, 1975; Rango and Martinec, 1981; Hall et al., 1995; Aniya et al., 1997), as it offers a synoptic view of glaciers at regular intervals over large spatial scales. The 2D techniques in their initial development, also allowed the creation of glacier inventories (e.g., Post et al., 1971; Patzelt, 1980; Aniya, 1988), topographic mapping from vertical photographs and elementary feature tracking and glacier velocity estimations were also available products.

The ascension of digital photogrammetry, the science of extracting precise geometric information from photographs in X, Y, and Z coordinates, made possible the construction of DEMs (Digital Elevation Models), comprehensive 2.5D of the Earth's surface, from aero photos. Those products and photogrammetric techniques enabled sophisticated analysis even in the 20th century and are broadly used up to today. Topographic maps, elevation changes, mass balance, surface velocity and ice flow analysis and measurements (e.g., Kappenberger et al., 1993; Etzelmüller et al., 1996; Kääb et al., 1998) could flourish without the necessary aid of field measurements.

Then, the advance of satellite spatial and spectral resolution proportioned high and fine resolution imagery. Those high-quality imagery from optical sensors increased the quality and accuracy of remote sensing results, that early on would still require geophysical, point data and other types of field measurements to complement or to determine the precision of the measurements. Inventory and further analysis of surface features, as supraglacial ponds and ice cliffs were greatly benefited.

More recently, Unmanned Aerial Vehicles (UAVs) have proved to offer several advantages over traditional remote sensing methods in glaciology. Firstly, equipped with advanced cameras and sensors, UAVs capture detailed imagery of the Earth's surface, at chosen resolution on demand,

impossible with traditional satellite imagery or aerial photography. This changeable resolution enables the detection of fine-scale features with 3D coordinates; as for larger features that would not require such fine-resolution, making it easy to adapt to different objects.

With the advent of 3D photogrammetry, fine resolution imagery could be combined with Structure from Motion (SfM) and Multi-View Stereo (MVS) enabled the generation of detailed 3D products of glaciers in accurate georeferencing. The SfM reconstructs the 3D structure of a terrain based on overlapped photos taken in different positions and angles that contains X, Y and Z coordinates, while MVS fill the gaps or reconstruct the 3D point clouds generated by SfM, increasing the density of the point cloud and providing more accurate details (Figure 7). Then, 3D analysis from point cloud, acquired from photogrammetry processing provided, a more correct and accurate representation of Earth's surface, as height were not assumed from a flat, constant, and uniform representation surface as in 2.5D data.

Also, UAVs offer enhanced temporal resolution and flexibility. Unlike satellite-based remote sensing, which operates on predefined acquisition schedules, UAVs can be deployed on-demand, allowing for more frequent and targeted data collection. This flexibility is particularly valuable for monitoring dynamic glacier processes that may exhibit rapid changes over short time periods, for example seasonal changes on supraglacial ponds and ice-cliffs. Combined to UAVs cost-effectiveness, those short-cycle dynamics and smaller glaciers can be monitored precisely and constantly.

In addition, traditional remote sensing methods often face limitations in acquiring data from rugged or remote glacier environments. In contrast, UAVs can navigate close to the glacier surface, collect data from hard-to-reach areas, and capture detailed information even in complex terrain that would not be visible from satellites, as ice-cliff backwasting. Hence, multi-view perspective from UAVs can provide highly accurate elevation data, allowing the generation of detailed 3D products of glacier, capturing retreat on the whole cliff body from its upper edge to the water contact in X, Y and Z direction. This is an important process to difference horizontal to vertical wasting (down- and backwasting).

In summary, UAVs provide several advantages over traditional remote sensing methods in supraglacial ponds and ice cliff mapping and analysis. This includes high spatial and temporal resolution, accessibility to challenging features (i.e., small supraglacial ponds and ice cliffs), accurate georeferencing, and cost-effectiveness. These advantages have significantly advanced our understanding of glacial processes and their responses to environmental changes. However,

the combination with 2D and 2.5D sensors can still significantly contribute to our understanding of glaciological processes, especially regarding historical data and time analysis, necessary to understand glacier dynamics to climate.

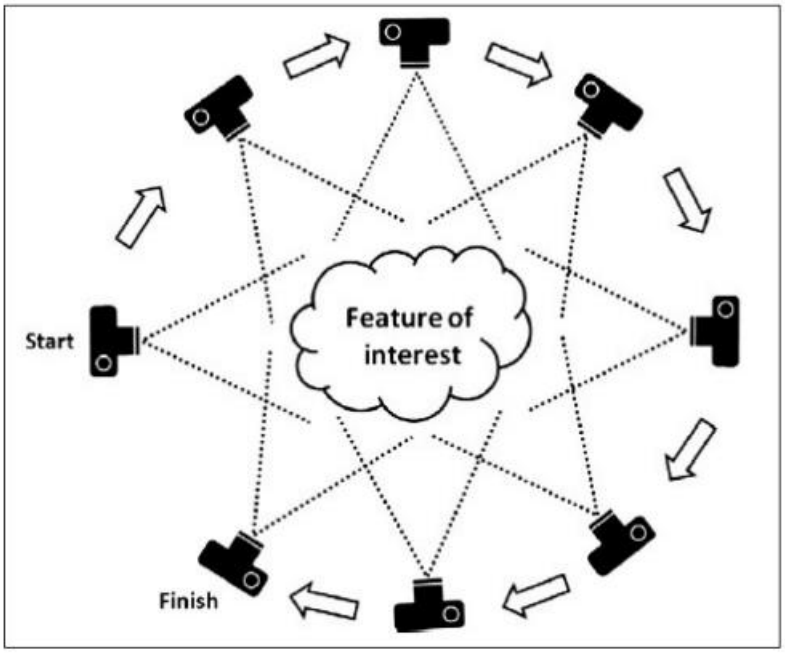

Figure 7 - Structure-from-Motion (SfM). Instead of a single stereo pair, the SfM technique requires multiple, overlapping photographs as input to feature extraction and 3D reconstruction algorithms. Source: Westoby et al. 2013.

4.1 Remote sensing and georeferencing

GPS-based positioning systems are an important part of remote sensing and photogrammetry. This technology has also evolved within the field of remote sensing, tracking, and adapting to new sensors and techniques. This allows users to determine the precision location (latitude, longitude, and altitude) of features on Earth's surface, in each image or photo. For this reason, different positioning systems are applied depending on the dataset and the accuracy necessary for the analysis.

First, there is GCP (Ground Control Points), known physical points on the surface with accurately surveyed coordinates, widely applied to georeferencing and align aerial photographs, topographic maps and satellite imagery. The ascension of services and applications that utilize GPS data and other location information to provide navigation or mapping, as Google Earth, aid on the gathering of coordinates, not necessarily requiring field surveys, at least for large or medium scale analysis. Although substantial progress has been made since then, GCP is still extensively applied nowadays, as it is a straightforward way to increase accuracy in any dataset.

Along with GCP, the usage of tie points (TP) establishes the relationship between image and ground within two or more images, important process for registration and potentially increasing accuracy. The identification of similar features within datasets, or tie points, are mostly automated or semi-automated in photogrammetry software, such as Agisoft or OrthoEngine. It can also be manually defined to align old maps to new dataset, for example.

Then, through the usage of drones and satellites, high-precision remote positioning progressed. Post-processing kinematic (PPK) positioning technique records GPS data during imagery collection and stores it in the base station and rover. It is processed afterwards using satellite orbit and clock data as post-process positions, this means that no real-time corrections are made. UAV can also benefit from PPK, however, the usage of RTK (real-time kinematic) on drones enables sub-centimeter positioning accuracy with no post-processing requirements. This is because the base station transmits corrections to the rover, allowing it to calculate its precise position. Although, the usage of RTK is enhanced and suitable for small glaciers, like Tapado Glacier, as the rover and base station needs constant communication to transmit the positioning corrections to the rover, which can be difficult to accomplish in large glaciers. It leaves PPK suitable for applications with longer baseline distances.

PPK and RTK systems revolutionized GCP applications as well, once coupled with photogrammetry software, RPCs (rational polynomial coefficients) crossed the bridge between the pixel coordinates within the satellite image and their real-world geographic counterparts. The translation of the pixel coordinates to real geographic coordinates makes the collection of GCP unnecessary – however, it still has the potential to increase accuracy in some cases.

4.2 Overview and prospects of UAV in glaciology

UAVs come in various sizes and configurations, ranging from lightweight fixed-wing aircraft to multi-rotor copters. Fixed-wing UAVs are ideal for covering large areas and conducting long-endurance flights, while multi-rotor UAVs offer vertical take-off and landing capabilities, allowing for precise data collection in confined areas. These platforms can be equipped with different payloads, including RGB cameras, multispectral and hyperspectral sensors, thermal infrared cameras, LIDAR systems, and even ground-penetrating radar (GPR) (James & Robson, 2014). Other than that, UAVs can enhance traditional field-based glaciology research by providing spatially extensive data coverage and reducing the need for manual measurements. For instance, UAVs can be used to collect ground control points for georeferencing, aiding in the accurate registration of satellite or airborne imagery.

Application of UAVs in glaciology began in polar glaciology, as high-resolution imagery allowed researchers to map glacier features and sea ice with high accuracy (e.g., Inoue, 2008; Walter et al., 2009; Crocker et al., 2011, Friedli, 2013), also allowing multi-temporal, feature tracking and flow calculations (e.g., Whitehead et al., 2013). Alpine glaciology introduced the usage of high-resolution DEM from drone imagery (Clayton et al., 2012), however, multi-view stereography through structure from-motion (SfM) to map glacial landforms was introduced a year later in polar glaciology field (e.g., Solbøa and Storvolda, 2013), which advanced the techniques for topographic mapping and photogrammetric measurements. Geomorphological mapping and glacier dynamics studies thrived with the advantages and practicalities of UAV-based mapping in the followed years (e.g., Tokin et al., 2014; Ryan et al., 2015).

Those measurements are crucial for assessing the contribution of glaciers to sea-level rise, water storage and understanding the response of glaciers to climate forcing, serving as valuable input data for numerical models that simulate glacier behavior and predict future glacier changes, improving their accuracy and reliability. Furthermore, they facilitate the identification and mapping of glaciers, as for detecting surface changes on glaciers. These features play a significant role in glacier dynamics and can provide insights into processes such as ice flow and meltwater runoff, as for helping researchers understand the drivers of glacier retreat and the impact of surface lowering on glacier mass balance.

High mountain glaciers, in other hands, had its first attempt to map and generate high-resolution DEMs and orthomosaics years later in the Himalayas (Immerzeel et al., 2014), providing a picture of the presence and dynamics supra-glacial and englacial channels and serving as a reference for other studies on glacier dynamics. Immerzeel et al. (2014) also combined, for the first time, UAV data with energy balance measurements on lakes and cliffs to understand differential melting in the debris-covered areas of a glacier. His work was succeeded by Miles et al. (2016), whose performed energy-balance modelling of a supraglacial pond on Lirung glacier, and by Kraaijenbrink et al. (2016), whose generate high-resolution DEMs and orthomosaics for further estimating the seasonal surface velocity.

The utilization of UAVs in high-altitude glacier studies has shown significant promise, especially contributing to regional water resource management and hazards assessment, response to climate change, understanding of global glacial systems and monitoring growth or retreat of ice cliffs, as it can be in centimeter-scales that requires fine precision on z-axis. Scientists have been able to analyze glacier mass loss, energy balance, and surface elevation

changes using SfM methodology (e.g., Westoby et al., 2012) and compare to localized changes within the glacier extent related to cliffs and ponds (e.g., Brun et al., 2016b; Kneib et al., 2022).

Inside the scope of high mountain glacier, repeated surveys using UAVs at different time intervals have provide insights into the seasonal variations in cliff and pond density, water level fluctuations of supraglacial pond, changes in extent in those features, and changes in ice-cliff geometry (e.g., Watson et al., 2017; Steiner et al., 2019). Ice cliff dynamics were the most benefited from UAVs, from UAV derived DEMs for ice cliff backwasting estimation (e.g., Brun et al., 2016b; Kneib et al., 2022) to 3D modelling analyzed (e.g., Buri et al., 2016a; Brun et al., 2018). Those studies and others revealed that their proportion and placement on the glacier surface can change considerably in a short time, and they can contribute drastically to total ablation.

Mostly of studies are still concentrated in the Himalayas region, with no 3D analysis for ice cliffs in the Andes region. The usage of drones in a 3D point cloud approach can improve the understanding of regional patterns, yet not broadly applied. That is because height values are generalized in some order on derived DEM analysis and multi-view UAV are undermined by nadir view of satellites, omitting horizontal displacements under cliff edge or close to water surfaces and producing higher uncertainties. Brun et al. (2018) have shown that DEM and terrestrial photography can overestimate ice cliff volume loss by 9%.

In other hand, supraglacial ponds mapping hasn't widely used UAV technology, as many recent papers still use satellite imagery (e.g., Liu et al., 2015; Watson et al., 2016; Miles et al., 2017; Miles et al., 2018; Chand and Watanabe, 2019), not yet taking advantage of temporal control, reduced cloud cover interference and higher spatial resolution for reduced cost. It is important, however, to consider the limitations of UAVs in high-altitude and debris-covered glacier studies. The extreme environmental conditions, including low temperatures, strong winds, and high altitudes, can pose operational challenges for UAV flight. The limited flight endurance of UAVs restricts the area coverage and duration of data collection. Additionally, the accuracy of UAV-derived data, such as DEMs and orthomosaics, can be influenced by factors such as image quality, flight altitude, and sensor calibration (James & Robson, 2014). Despite these limitations, UAVs have proven to be valuable tools in high-altitude and debris-covered glacier studies, offering unprecedented access to remote and challenging glacier environments. By overcoming the limitations of traditional methods, UAVs have provided researchers with a

wealth of high-resolution data, facilitating improved monitoring, analysis, and understanding of unique dynamics on supraglacial ponds and ice cliffs.

Thus, UAV technology is continuously advancing, with ongoing developments in platform design, sensor capabilities, and data processing techniques. Improvements in flight endurance, payload capacity, and autonomous flight capabilities are expanding the possibilities for UAV-based glaciology studies. The use of UAVs in conjunction with satellite remote sensing and ground-based observations offers opportunities for multi-scale data integration and model validation. Combining data from different platforms enhances our understanding of glacier processes, improves the accuracy of predictive models, and provides more comprehensive assessments of glacier change.

5. Methods and Materials

5.1 Remote sensing data

A variety of remote sensing datasets were utilized in this study, as shown in Table 1, including historical aerial photographs, stereo satellite imagery, high resolution satellite imagery, UAV imagery and post-processed raster analyzes. Three sets of aerial photography (1955, 1978 and 2000) were pre-processed by Robson et al. (2022), providing orthomosaic and DEM for respective scenes. Table 1 summarizes data processed in the current research for satellite data, and Table 2 summarizes the UAV mission, respectively. Acquired data information can be checked in the original publications.

Table 1 –Satellite datasets used in this study. For the imagery used to produce DEMs, the RMSE values for tie points are shown.

Date	Sensor	Image IDs	Resolution (m)	Tie point X RMSE (pixels)	Tie point Y RMSE (pixels)
30. november 2010	GeoEye-1	2010041214433841603031601795	0.5	0.18	0.05
23. mars 2012	GeoEye-1	2012032314444141603031604885	0.5	0.15	0.03
31. januar 2019	Pléiades	DS_PHR1A_201901231456588_FR1_PX_W070S31_0120	0.5	0.16	0.18
1. mars 2020	Pléiades	DS_PHR1B_202003011456169_FR1_PX_W070S31_0120	0.5	0.17	0.27
2. februar 2023	Pléiades	PNEO4_202302021444415	0.5	0.32	0.07
april 2017	Planet	20170413_135513_0f25	3	-	-
april 2018	Planet	20180408_154402_1049	3	-	-
march 2021	Planet	20210313_142521_1009	3	-	-
2009	QuickBird	peru_4_11_10_qb_BOOST	0.6	-	-

Table 2 – UAV datasets used in this study. Viewing angle and GPS system are shown.

Date	Sensor	Viewing angle	Resolution (cm)	Unity of photos	GPS system
11. april 2023	DJI Mavic 3E	Oblique	2.5	1212	RTK
09. dec 2022	DJI Mavic 3E	Nadir	4.8	758	RTK
26.feb.2020	DJI Mavic Mini	Free Flight	1.16	172	GCP
21.mar.2019	DJI Mavic Mini	Free Flight / Nadir	0.94	562	GCP

Multi-stereo UAV acquisitions cover different sections of Tapado Glacier, as exemplified in Figure 8, in which resolution ranges from 0.94 cm to 4.8 cm depending on date and area surveyed (Table 2).

The UAV dataset of 2022 was acquired during a field trip to Tapado Glacier, while datasets from other years were acquired by Benjamin Robson (2019 and 2020) and Álvaro Ayala (2023). Due to changes in operator, UAV-system, and positioning system, georeferencing underwent a transition from onboard GPS (2019) to DGPS (2020), while a DJI RTK base

station was used in 2022 and 2023 to provide centimeter level positioning. Flight mode and height were also heterogenous among the surveys, as oblique view missions were only applied from 2022. Thus, images in 2019 and 2020 were obtained through nadir viewing angle or free flight mode, which could lead to some areas of the ice cliffs not being adequately covered.

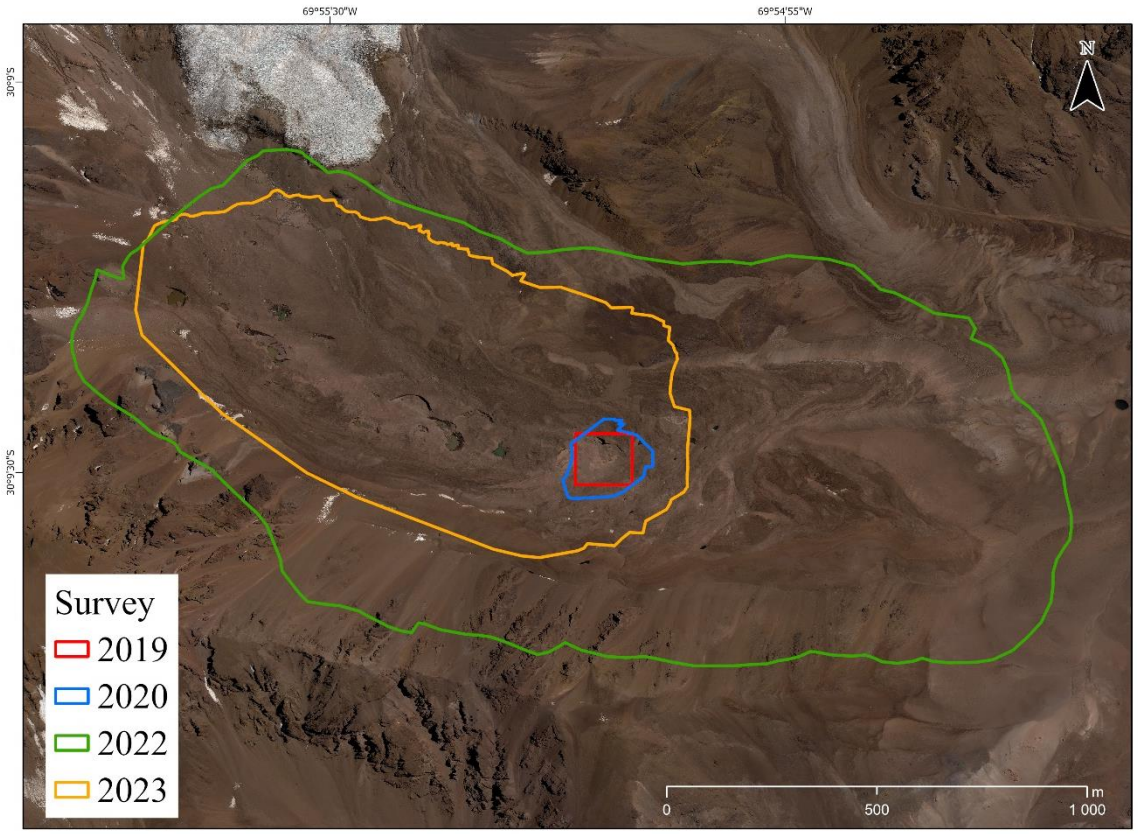

Figure 8 – Area surveyed during UAV mission in Tapado Complex, Chile, from 2019 to 2023. Orthomosaic from Pléiades imagery (2023). Source: author.

Tri-stereo satellite imagery covering the entire catchment was also used, namely two GeoEye-1 datasets (2010 and 2012) and three Pléiades datasets (2019, 2020, 2023), both at 50 cm resolution, in which RMSE from the subsequent bundle adjustment can be consulted in Table X. In addition, high resolution multispectral satellite imagery from Quickbird (2019) and Planet (2017, 2018, 2021) were also added for time resolution improvement on analysis.

Apart from datasets, post-processed raster analyses were also acquired. Differential digital elevation models (dDEMs) where pixel values represent surface thinning or thickening were available for the time periods 1955-1978, 2000-2012 and 2015-2020, and surface velocity estimation data were borrowed from Robson et al. (2022). The surface velocity data was attributed to a mean uncertainty ± 0.03 m a^{-1} (Robson et al., 2022).

5.2 Generation of photogrammetric DEM, orthomosaic and dense cloud

The DEM generation for tri-stereo satellite and UAV went through different software and processing steps. Starting with tri-stereo satellite imagery, it was photogrammetrically processed in PCI Geomatica v2222.0.6 (Figure 9) using rational polynomial coefficients (RPCs) provided with the imagery. As the pixel coordinates were linked with image coordinates, no external ground control points were used; instead, automatically generated tie points, with RMES < 0.8 pixels for the tie points, were used to solve the relative orientation and perform a bundle adjustment. Before the DEMs extraction, epipolar images were generated to align coordinates of corresponding points in the left and right images harmoniously along a shared x-axis. Then, DEMs were extracted at 50 cm resolution, using the semi-global matching (SGM) algorithm, which has been shown to work well in scenarios featuring complicated topography and fine-grained geometric complexities. The multispectral images were pansharpened before being mosaiced together.

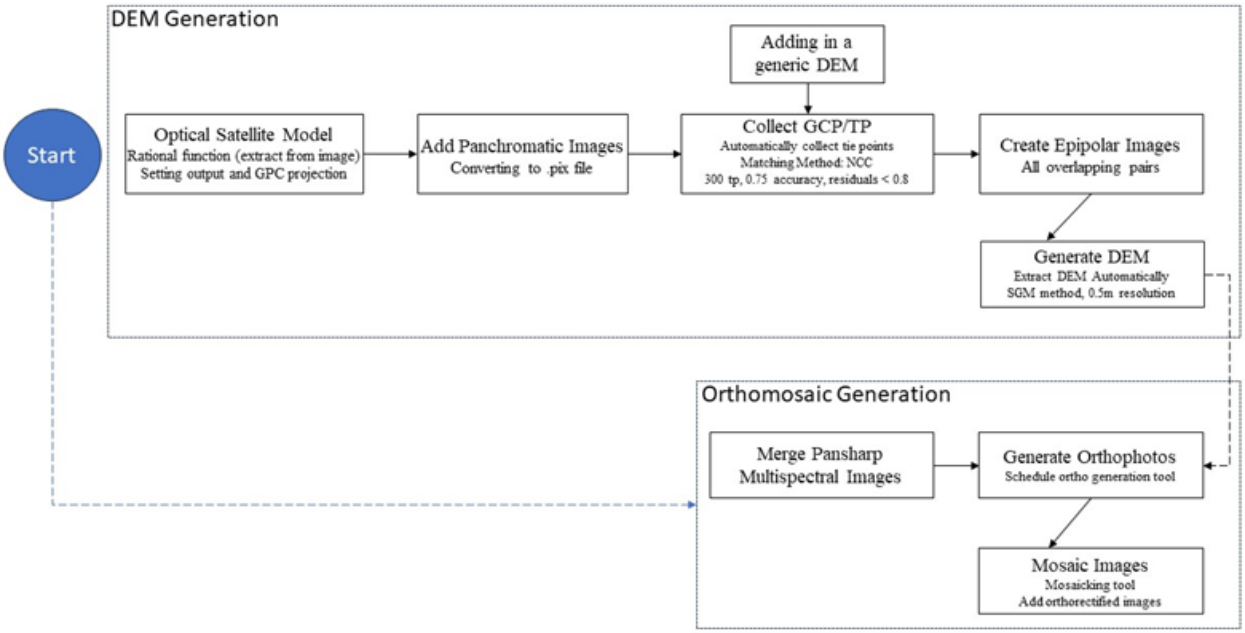

Figure 9 - Workflow model of photogrammetry for the generation of DEM and orthomosaic in PCI Geomatica v2222.0.6 performed on Geoeye and Pleiades tri-stereo satellite imagery. Source: author.

The UAV imagery was photogrammetrically processed in Agisoft Professional v2.0.2 (Figure 10) on images with quality higher than 0.7 units, using highest quality processing options. Previous to the tie point generation, cameras were calibrated and optimized, thus ties points were semi-automatically filtered using gradual selection tool. The percentage of tie points subject to removal ranged from 5% to 20% of the total tie points, as heterogenous datasets

present different noisy, erroneous, or less reliable tie points. In this way, a consistent threshold could not be defined and applied over the whole years of data, apart from image count that was set on 2. From the cleaned tie point clouds, the subsequent products of dense point cloud, mesh model, orthomosaic and DEM are generated. Although resolution varied throughout surveys, DEMs and orthomosaics were exported in a 50 cm resolution, for consistency.

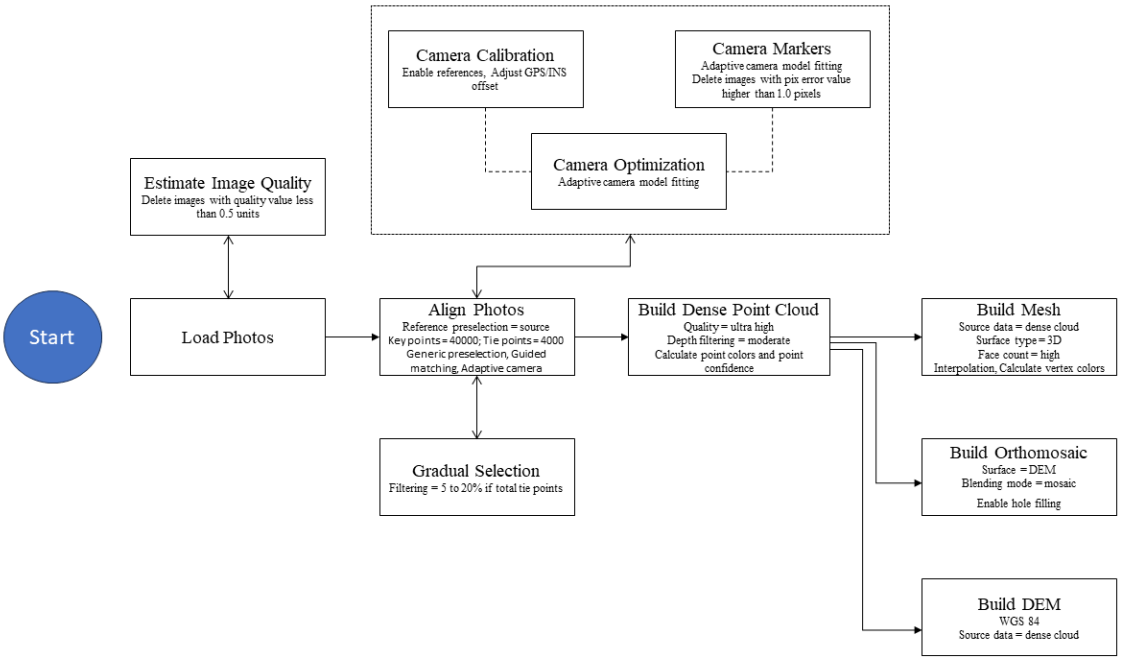

Figure 10 – Workflow of photogrammetry for the generation of DEM, orthomosaic and dense cloud from UAV **datasets performed in Agisoft Metashape Professional 2.0.2. Source: author.**

5.2 Co-registration, dDEM and point distance

Linear co-registration biases were removed following the methods presented by Nuth and Kääb (2011), which minimize the root mean square slope normalized elevation biases over stable terrain until the standard deviation over stable terrain changed by less than 2%. Polynomial co-registration biases were removed applying the iterative closest point (ICP) based on Besl and McKay (1992), which iteratively move the data in x, y, and z coordinates until it fits the reference as well as possible.

The DEMs resulted from tri-stereo satellite imagery underwent through both co-registration processes, using xDEM library on python language (Table x). The dDEM, then, were simply produced by a subtraction of reference DEM and aligned DEM. To produce yearly rates of

surface elevation changes a subtraction including date and time of original scenes was necessary, as a simple raster subtraction would only provide total lowering in between DEMs. Fortunately, xDEM library includes date and time functions for dDEM generation. As mentioned before, only the dDEM from 2020-2023 was produced for this thesis, as previous dDEMs periods were acquired from Robson et al. (2022), and co-registration matrix can be seen in the original publication.

Table 3 - Co-registration shifts calculated over stable terrain between the respective DEM pairs.

DEM pair	Co-registration shift (m)		
	X	Y	Z
2020-2023	12.46	-0.69	-14.99

On dense cloud points from UAV photogrammetry only ICP alignment was applied, however with match scale function that allows scale matching from dense clouds produced from different sensors and pixel-scale imagery. CloudCompare v2.13 was also used to calculate distance from points in between dense clouds, using the M3C2 plugin developed by Lague et al. (2013). It computes the local distance between two point clouds along a surface direction that tracks 3D variations in surface orientation in between analyzed cliff area. For ice-cliff vertical and backwasting, the +Z surface orientation was chosen.

Table 4 - Co-registration shifts calculated over stable terrain between the respective dense cloud pairs.

Dense cloud pair	Co-registration shift (m)		
	X	Y	Z
2022-2023	8.54	-10.81	51.38
2020-2022	-528.64	-644.26	278.67
2019-2020	-315.32	-330.50	1461.66
2022-2023	-32.11	-15.66	109.32

5.4 Supraglacial ponds and ice cliffs classification

Supraglacial ponds and ice cliffs were mapped from orthomosaics and high multispectral satellite resolution. In fine resolution orthomosaic and Quickbird imagery, a manual delineation of features took place, once ponds and cliffs could be clearly distinguished and accurately delineated. However, on planet imagery and orthomosaic from aerophotos, the ice cliffs and

supraglacial ponds couldn't be well distinguished from surrounding terrain, especially smaller ones.

For those data with pixel > 1m, a semi-automated workflow was constructed on model builder in ArcgisPro v3.0.2. First, normalized difference water index (NDWI), using green and near-infrared band, were used to identify water bodies. Then, a binary threshold, which categorizes an image due pixel brightness, could automated separate water bodies from non-water bodies, both for NDWI and grayscale panchromatic orthomosaic from aero photos. Ice features, however, had to be separated from water, thus, all features outside from the debris-covered area is excluded, then a threshold of $< 1025m^2$ & $> 36m^2$, this is, smaller than the biggest mapped supraglacial pond and greater than two pixels. However, manual reshaping on polygons shape were necessary, and ice-cliffs requested an entirely manual classification process, as ice is mostly hidden under the cliffs, not visible from nadir imagery.

5.5 Location and frequency analysis

Location analysis was conducted using two main products: surface elevation and surface gradient information. The glacier's surface velocity data was sourced from the work of Robson et al. (2021), while the slope gradients were derived from Digital Elevation Models (DEMs) generated previously using the slope tool in QGis 3.26.3, employing Horn's algorithm. To ensure precision, the velocity and slope values were incorporated into the pond dataset within a pixel buffer zone, accounting for the inherent uncertainty associated with their delineation.

Initially, the supraglacial ponds and ice cliffs are converted into raster format, which are reclassified into non-ponded/cliffed areas and ponded/cliffed areas, as 1 and 2 respectively. Those reclassified rasters are multiplied in between, this means that every pixel classified as ponded/cliffed area will undergo to a multiplication of factor 2, while pixels without the features will be multiplied by 1, not changing its value. Finally, the overlapped classes are further normalized from 0 to 1 using the rescale by function tool in ArcGIS Pro.

5.6 Uncertainties

5.6.1 Area extent

Three main uncertainties were quantified: supraglacial pond and ice cliff area error, dDEM distance error and M3C2 distance uncertainty. Error in area determination, caused by presence of shadows and oblique contact surfaces between supraglacial ponds and ice cliffs, was

estimated by multiplying feature perimeter by spatial resolution of dataset (Casassa et al., 2014; and Loriaux and Ruiz, 2021).

$$Ae = \pm n * p$$

In which *Ae* is the total area calculation errors, *n* is delineation error expressed as known or estimated precision of point measurements (pixels), and *p* is perimeter length. The mean estimated total error for each period analyzed is expressed in table X.

Table 5 – Calculated mean error in square meters of mapped supraglacial ponds and ice cliffs in each analyzed period.

	Mean error (m2)	
Period	Ponds	Cliffs
1955-1978	445.18	156.45
2000-2012	25.42	41.24
2015-2020	81.38	160.37
2020-2023	49.93	59.03

5.6.2 Differential DEM error

The dDEMs error (Figure 11) rely on a non-stationary spatial statistics framework to estimate and model the variability in elevation error, using terrain slope and maximum curvature as explanatory variables, with stable terrain as an error proxy for moving terrain (Hugonnet et al., 2022), with 95% confidence level. Where $\sigma h_1(x, y)$ is the average variance of elevation differences in stable ground through acquisitions (N).

$$\sigma_{h1}(x.y) = \frac{\sigma_{dh1-2}(x,y)}{\sqrt{N}}$$

Slopes with higher degree contain higher error than flatter terrain, and this is clearly seen as red (~2m error), and white (~1m error) colors are concentrated along ice-cliffs and clean-ice glacier boundary transition into debris-covered glacier.

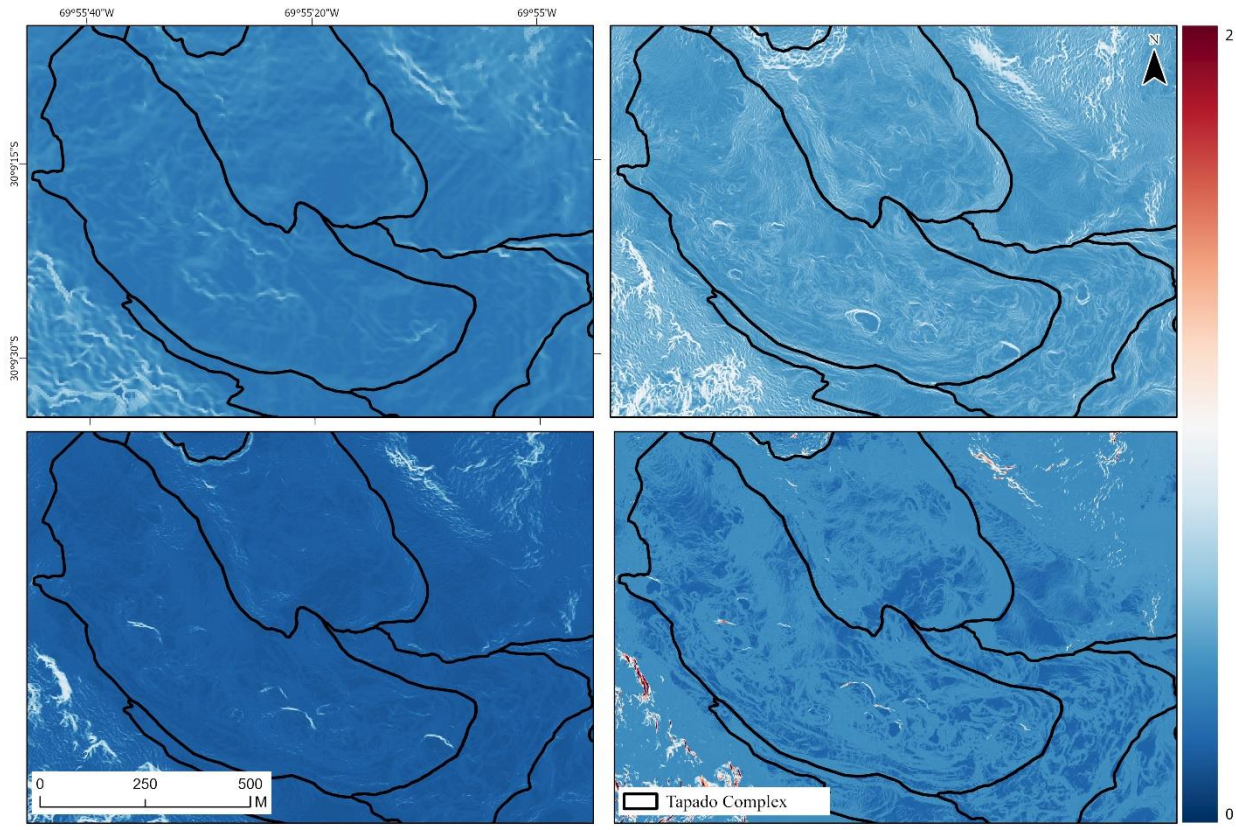

Figure 11 – Elevation error map for dDEM pairs of 1955-1978 (up left), 2000-2012 (up right), 2015-2020 (bottom lleft) and 2020-2023 (bottom right) showing yearly rates in meters. Source: author.

5.6.3 M3C2 Uncertainty

The M3C2 uncertainty ($LOD_{95\%}(d)$) assumption, in Figure 12, is based on the registration error (*reg*), assumed isotropic and spatially uniform, and the local point cloud roughnesses σ_1 and σ_2, of diameter *d* and size *n1* and *n2*, measured along the normal direction in a parametric estimate based on Gaussian statistics (Lague et al., 2013).

$$LOD_{95\%}(d) = \pm 1.96\left(\sqrt{\frac{\sigma_1(d)^2}{n_1} + \frac{\sigma_2(d)^2}{n_2}} + reg\right)$$

Errors in M3C2 is less than 0.1ma^{-1} in mostly of the terrain, even at ice cliffs, proving its higher accuracy if compared to DEM generated products.

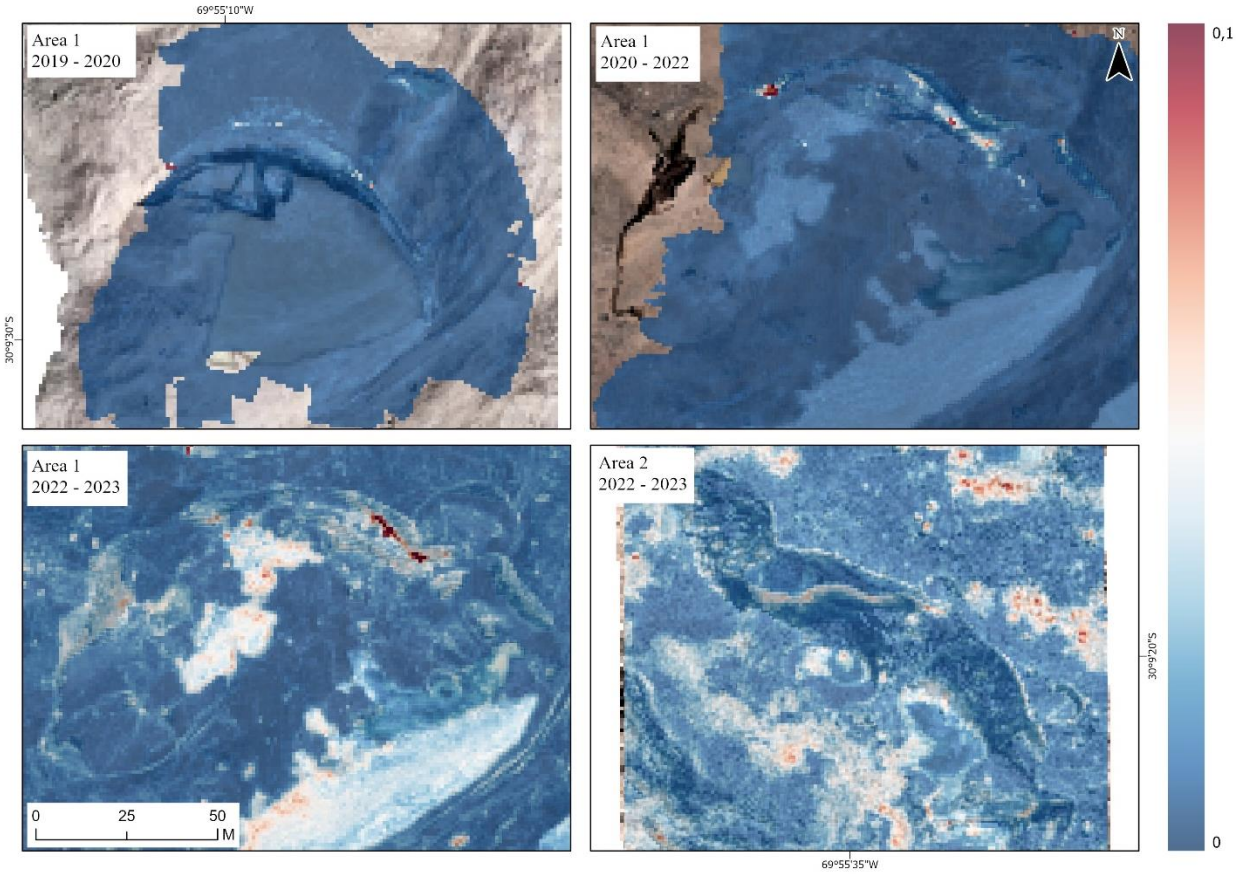

Figure 12 – M3C2 uncertainty map for dense cloud pairs for ice cliff 1 in 2019-2020, 2020-2022 and 2022-2023, and for ice cliff 2, 3 and 4 in 2022-2023. The errors are shown in meters per year, and all scenes are in the same scale. Source: author.

6. Results

6.1 Supraglacial ponds and ice-cliffs classification

6.1.1 Area extent and changes

The performed classification of the monitored features according to assigned methodology is expressed in Figure 13. There we can see the location of supraglacial ponds and ice-cliffs from 1995 to 2023 in the debris-covered glacier area.

Across all studied years it was identified a total of 285 supraglacial ponds, with a mean observed pond size of 202.71 ± 55.45 m^2 (Table 6). In 2000, 2020 and 2023 have the highest amounts of identified ponds, with 32, 44 and 38 respectively; however, the years of 1955, 2010, 2017, 2019, 2021 have the highest percentage of ponded area withing Tapado Glacier (Table 7). Number of ponds showed an inverse relationship with average area, this means that higher quantity of ponds produces smaller ponds, not being necessarily related to the total input of water in the catchment (total area of ponds).

The number of observed ice cliffs was lower than supraglacial ponds, with an overall quantity of 163 and mean area of 270.33 ± 73.75 m^2, with ~41% of ponds coinciding with an ice cliff. The years with the highest number of ponds also present the highest quantity of cliffs. Cliff area also showed a correlation with mean ponded area, in which higher pond area reflects in a higher cliffed area. As seen in Table 6, the years 2017, 2018 and 2021 shows a mean pond area of ~579.00 m^2, ~448.50 m^2 and ~603.85 m^2 for supraglacial ponds, while cliff area is ~832.70 m^2, ~867.07 m^2 and ~769.41 m^2, respectively. While the years 2000, 2010, 2012 shows a mean pond area of ~104.84 m^2, ~119.06 m^2 and ~128.53 m^2, while for cliffs it is ~135.71 m^2, ~178.61 m^2 and ~206.22 m^2, respectively.

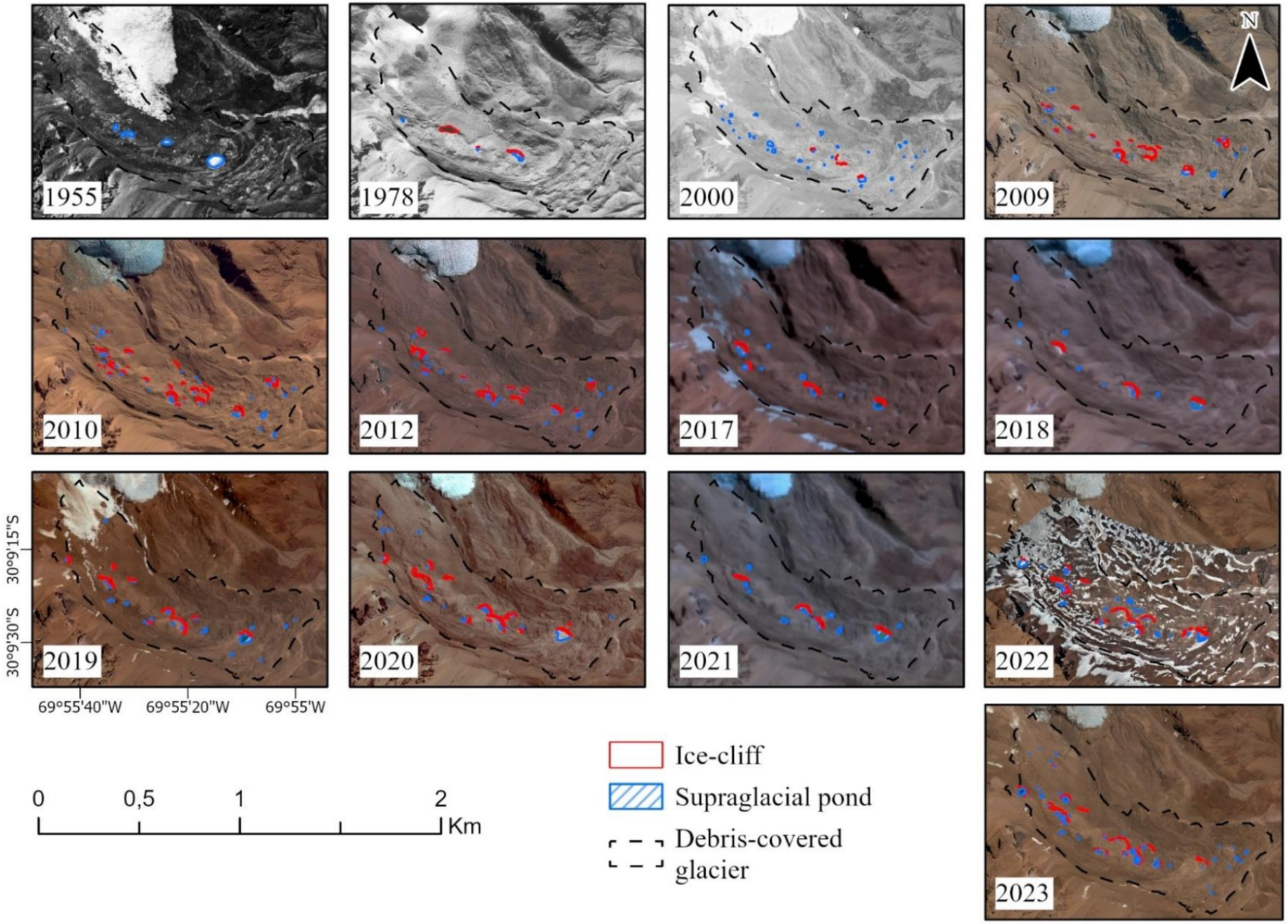

Figure 13 - Supraglacial ponds and ice cliffs in debris-covered glacier surface on Tapado Glacier from 1955 to 2023. Elaborated by author.

Table 6 - Classified supraglacial ponds and ice cliffs quantity and mean area in square meter with uncertainty included by year in the debris-covered glacier zone.

	Quantity			Supraglacial ponds				Ice cliffs			
Year	Supraglacial ponds	Ice cliffs	Ponds with cliffs	Total area (m2)	Total error (m2)	Mean area (m2)	Mean error (m2)	Total area (m2)	Total error (m2)	Mean area (m2)	Mean error (m2)
1955	4	0	0	5671.93	2846.29	1417.98	711.57	-	-	-	-
1978	3	3	1	1263.27	269.96	421.09	89.99	2905.08	469.36	968.36	156.45
2000	32	4	2	3354.91	1138.18	104.84	35.57	407.13	227.88	135.71	75.96
2009	25	16	13	4355.40	711.87	174.22	28.47	4250.57	915.51	236.14	50.86
2010	44	31	25	5238.54	812.43	119.06	18.46	5533.85	964.99	178.51	31.13
2012	31	20	13	3747.77	693.11	128.53	22.36	4124.48	860.54	206.22	43.03
2017	9	4	4	5211.01	2177.47	579.00	241.94	3330.79	2009.70	832.70	502.42
2018	8	3	2	3587.98	1782.01	448.50	222.75	2601.21	1711.62	867.07	570.54
2019	25	11	11	4872.50	669.46	194.90	26.78	3162.99	633.65	287.54	57.60
2020	23	14	13	5152.16	660.90	223.76	28.73	6691.13	923.10	477.94	65.94
2021	12	4	5	7246.25	3109.17	603.85	259.10	3077.64	2153.64	769.41	538.41
2022	31	34	6	4223.96	69.33	136.26	2.24	2597.16	99.96	76.39	2.94
2023	38	18	24	4455.24	865.43	160.30	22.77	5383.00	1052.30	299.06	58.46

The rates of changes between years vary considerably, considering only the years with consecutive monitoring and imagery at similar resolution, from ~-11% in pond quantity (2017-2018) to ~76% (2018-2019), with a mean of ~19% increase in pond quantity. The mean change

The number of observed ice cliffs was lower than supraglacial ponds, with an overall quantity of 163 and mean area of 270.33 ± 73.75 m^2, with ~41% of ponds coinciding with an ice cliff. The years with the highest number of ponds also present the highest quantity of cliffs. Cliff area also showed a correlation with mean ponded area, in which higher pond area reflects in a higher cliffed area. As seen in Table 6, the years 2017, 2018 and 2021 shows a mean pond area of ~579.00 m^2, ~448.50 m^2 and ~603.85 m^2 for supraglacial ponds, while cliff area is ~832.70 m^2, ~867.07 m^2 and ~769.41 m^2, respectively. While the years 2000, 2010, 2012 shows a mean pond area of ~104.84 m^2, ~119.06 m^2 and ~128.53 m^2, while for cliffs it is ~135.71 m^2, ~178.61 m^2 and ~206.22 m^2, respectively.

Table 7 - Classified supraglacial ponds and ice cliffs quantity and mean area in square meter with uncertainty included by year in the debris-covered glacier zone.

	Quantity			Supraglacial ponds				Ice cliffs			
Year	Supraglacial ponds	Ice cliffs	Ponds with cliffs	Total area (m2)	Total error (m2)	Mean area (m2)	Mean error (m2)	Total area (m2)	Total error (m2)	Mean area (m2)	Mean error (m2)
1955	4	0	0	5671.93	2846.29	1417.98	711.57	-	-	-	-
1978	3	3	1	1263.27	269.96	421.09	89.99	2905.08	469.36	968.36	156.45
2000	32	4	2	3354.91	1138.18	104.84	35.57	407.13	227.88	135.71	75.96
2009	25	16	13	4355.40	711.87	174.22	28.47	4250.57	915.51	236.14	50.86
2010	44	31	25	5238.54	812.43	119.06	18.46	5533.85	964.99	178.51	31.13
2012	31	20	13	3747.77	693.11	128.53	22.36	4124.48	860.54	206.22	43.03
2017	9	4	4	5211.01	2177.47	579.00	241.94	3330.79	2009.70	832.70	502.42
2018	8	3	2	3587.98	1782.01	448.50	222.75	2601.21	1711.62	867.07	570.54
2019	25	11	11	4872.50	669.46	194.90	26.78	3162.99	633.65	287.54	57.60
2020	23	14	13	5152.16	660.90	223.76	28.73	6691.13	923.10	477.94	65.94
2021	12	4	5	7246.25	3109.17	603.85	259.10	3077.64	2153.64	769.41	538.41
2022	31	34	6	4223.96	69.33	136.26	2.24	2597.16	99.96	76.39	2.94
2023	38	18	24	4455.24	865.43	160.30	22.77	5383.00	1052.30	299.06	58.46

The rates of changes between years vary considerably, considering only the years with consecutive monitoring and imagery at similar resolution, from ~-11% in pond quantity (2017-2018) to ~76% (2018-2019), with a mean of ~19% increase in pond quantity. The mean change rate in cliffs is ~90%, and a similar trend is observed, for the years with increase of ponds (2009-2010, 2022-2023), cliffs increased in ~92% and ~300%, while on 2017-2018 the quantity of cliffs decreased in ~-50%. However, in 2019-2020 supraglacial ponds decreased ~-8%, but cliffs increased ~18%. Visible trend between total area and mean area was not found, as some years experienced increase in total area but decrease in mean area, while others experienced increase or decrease in both.

Table 8 - Percentual area occupied by supraglacial ponds and ice cliffs within the surface of the Tapado Glacier and debris-covered glacier. The compared area was measured in 2023 only and used as standard value.

	Compared area (km2)		Percentage of area (%) in Tapado Glacier		Percentage of area (%) in debris-covered glacier	
Year	Tapado Glacier	Debris-covered glacier	Supraglacial Pond	Ice Cliff	Supraglacial Pond	Ice Cliff
1955			0.39	-	1.07	-
1978			0.09	0.20	0.24	0.55
2000			0.23	0.03	0.63	0.08
2009			0.30	0.30	0.82	0.80
2010			0.36	0.38	0.99	1.04
2012			0.03	0.29	0.07	0.78
2017	1.44	0.53	0.36	0.23	0.98	0.63
2018			0.25	0.18	0.68	0.49
2019			0.34	0.22	0.92	0.60
2020			0.36	0.46	0.97	1.26
2021			0.50	0.21	1.37	0.58
2022			0.29	0.18	0.80	0.49
2023			0.31	0.37	0.84	1.02

Occupied area by features is relative to their total area, this shows how much of the Tapado Glacier, and debris-covered glacier are under supraglacial ponds and ice cliff stress. Combined features reached up to ~2.23% of debris-covered glacier area in 2020, with lowest values in 1978, 2000 and 2021. Consistently, after the year 2000, those features occupied more than 1.15% of debris-covered glacier – apart from 2012 –, values do not seem before 2000, where percentage occupation varied from 0.71% in 2000 to 1.07% in 1955.

A higher mean and total area are, also, observed in supraglacial ponds that area connected with ice cliffs, as seen in Table 8. Supraglacial ponds in the vicinity of ice cliffs are on average 4.16 times bigger than the ones without developed ice cliff in the vicinity. This highlights the influence of ice cliffs in supraglacial pond development.

Table 9 – Difference in area between supraglacial with and without ice cliffs in their vicinity, as for the magnitude of extent area change between features.

Year	Cliff Presence (Yes/No)	Total area (m2)	Mean area (m2)	Magnetude of change
1978	N	221.60	110.80	9.40
	Y	1041.68	1041.68	
2000	N	2393.45	79.78	6.03
	Y	961.45	480.73	
2009	N	2371.10	169.36	1.07
	Y	1984.30	180.39	
2010	N	888.56	46.77	3.72
	Y	4349.98	174.00	
2012	N	690.44	38.36	6.13
	Y	3057.33	235.18	
2017	N	7968.64	185.32	2.22
	Y	8243.72	412.19	
2018	N	12101.49	288.13	1.51
	Y	6077.80	434.13	
2019	N	6057.78	61.81	2.96
	Y	14079.75	182.85	
2020	N	3191.33	45.59	4.13
	Y	17149.46	188.46	
2021	N	1273.86	318.46	2.34
	Y	5972.39	746.55	
2022	N	1079.99	63.53	3.53
	Y	3143.97	224.57	
2023	N	498.82	26.25	6.85
	Y	3956.42	179.84	

6.1.2 Frequency of features

Frequency analysis serves as a valuable technique for assessing the evolution of intersected pixels within supraglacial ponds and ice cliffs interannually, delineated within a scale ranging from 0 to 1, as Figure 14 and 15. In this context, 0 denotes no interannual persistency, while 1 represent the highest interannual persistence, that is 7 and 8 consecutive cliffed and ponded area, respectively.

Mostly of supraglacial ponds do not persist over the years analyzed, representing ~68.68% of total ponded area in between 1955-2023. Ponds prolonged occurrence through years vary, then, from ~14.53% to ~0.03%, for two and seven years of consecutive or reoccurrence of supraglacial ponds, as seen in Table 9. Prolonged ice cliffs follow the same pattern as ponds, although, they seem to undergo a shorter life cycle, which could indicate they are more active and/or sensitive features within the glacier. A total of ~74.21% of ice cliffs did not persist within two analyzed dates, otherwise they persistency in total area range from ~18.22% to ~0.02%, respective for two to seven consecutive appearances.

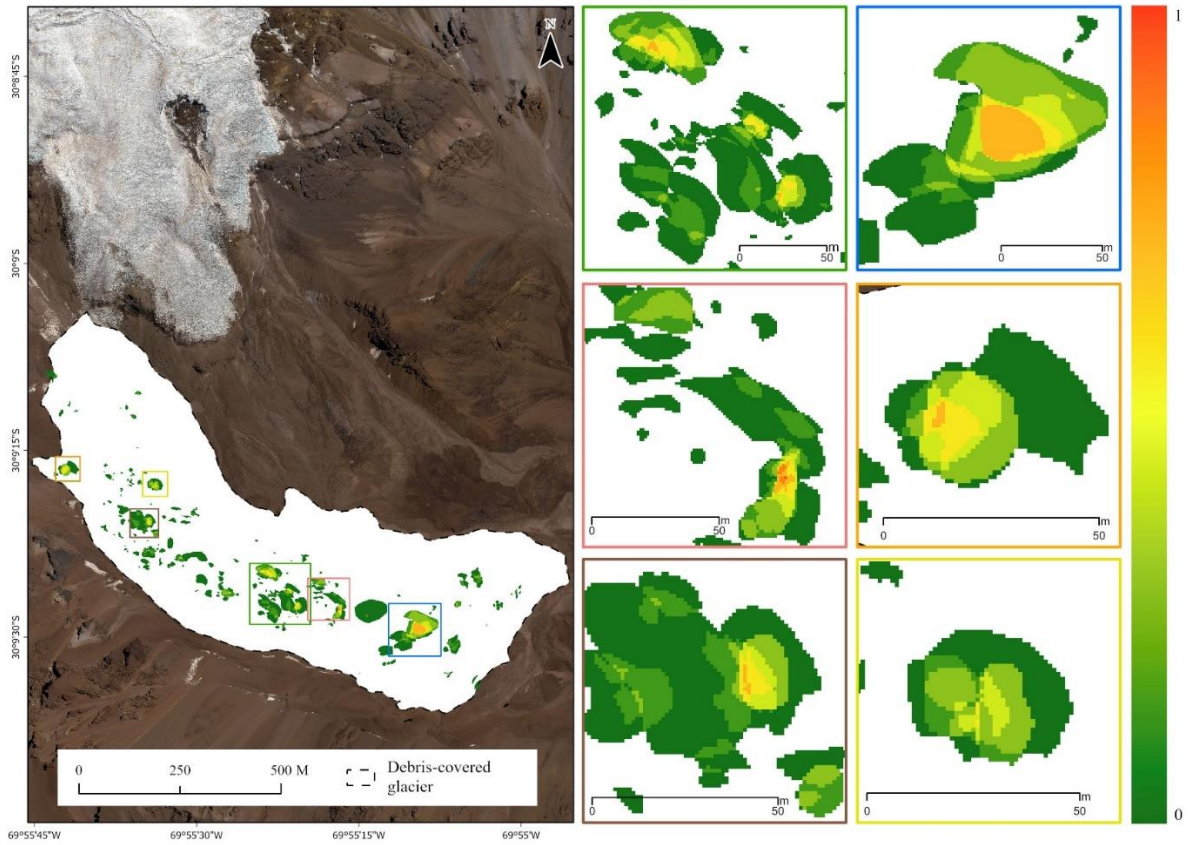

Figure 14 - Frequency of supraglacial ponds on the debris-covered glacier on Tapado Glacier, highlighting main areas of supraglacial ponds occurrence over the time series. Imagery from Pléiades 2023, elaborated by author.

Table 10 – Persistence of area in between analyzed datasets from 1955 to 2023, in which percentage of total supraglacial pond and ice cliff is represented for each persistence class. The persistence class, first column, means that ponds and cliffs were mapped from 1 scene to 8 scenes.

	Supraglacial ponds		Ice cliffs	
Persistence	Total area (m2)	Area percentage (%)	Total area (m2)	Area percentage (%)
1	26924	68.68%	23811	74.21%
2	5697	14.53%	5846	18.22%
3	3742	9.54%	1490	4.64%
4	1342	3.42%	605	1.89%
5	711	1.81%	295	0.92%
6	774	1.97%	34	0.11%
7	13	0.03%	6	0.02%
8	1	0.00%	0	0.00%

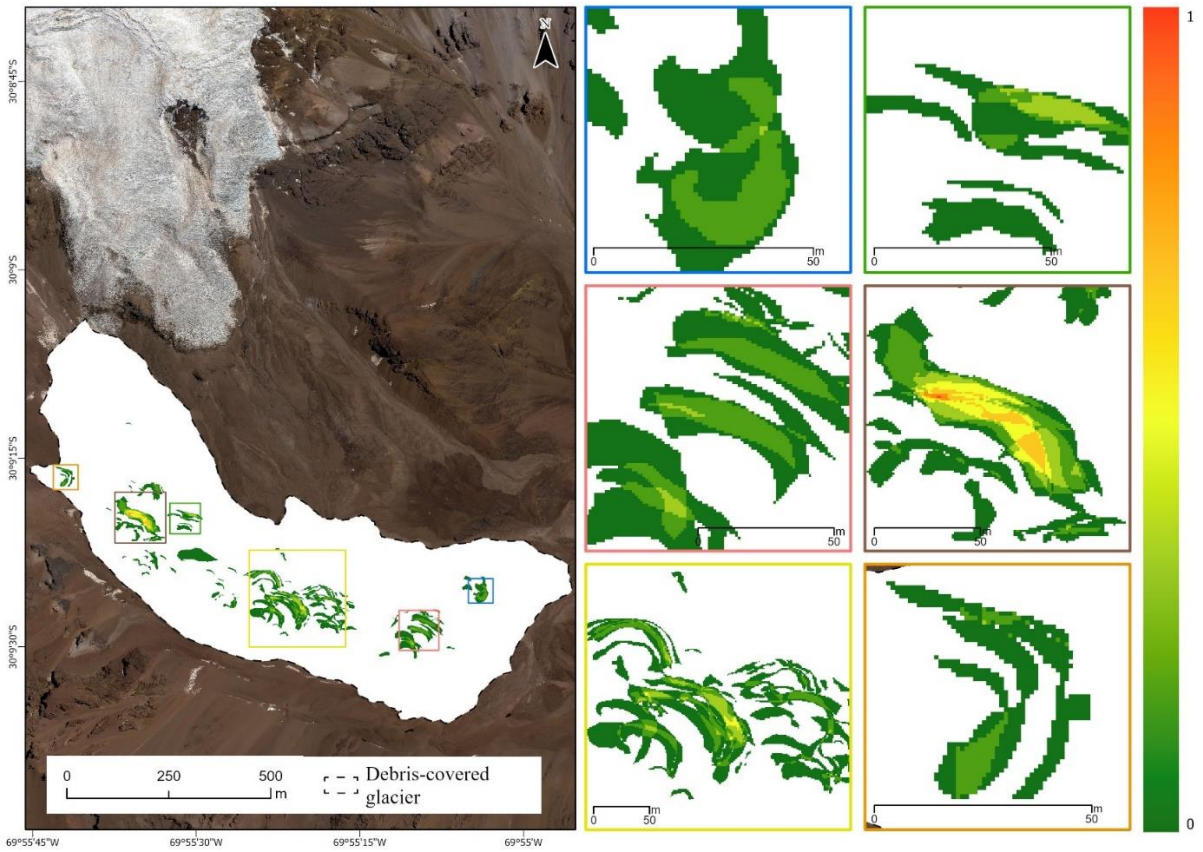

Figure *15* - Frequency of ice cliffs on the debris-covered glacier on Tapado Glacier, highlighting main areas of ice cliffs occurrence over the time series. Imagery from Pléiades 2023, elaborated by author.

6.1.3 Formation and development drivers

To get a closer answer to why supraglacial ponds originate where they do, the surface velocity and slope gradient values were calculated and related with pond presence, area size and cliff presence. Figure 16 shows each supraglacial pond by year in a color scheme – note that 2009, 2017, 2018 and 2021 years could not have their slope calculated due absence of DEMs. The determination of surface flow velocity and slope gradients within the supraglacial pond areas assumes significant importance. This analysis serves a dual purpose: first, it helps identify the regions where supraglacial ponds are likely to occur, and second, it pinpoints the specific boundaries where velocity and slope conditions play a pivotal role in their initiation or maintenance.

Although near half or more than half of our results have ponds placed within velocities < 2 ma^{-1} and on slopes between 2°–6° (category A) and between 6°–10° (category B), specially 1978, 2012, 2019 and 2022 with 66.67%, 61.29%, 60% and 93.55% respectively, there are still another near half of pond coverage in areas above 10° gradient (Category E), as for 2010 and 2019 with 40%, 2023 with 39.02% and 2012 with 36.6%. Across all years there is 28.6%,

35.5%, 0.4%, 0.8% and 34.6% of ponds in category A, B, C (> 2 ma^{-1} & < 6°), D (< 2 ma^{-1}, > 6° & < 10°) and E. Analyzing the ponded area within each category we have 31.4% in category A, 33.2% in category B, 0.06% in category C, 0.2% in category D and 35% in category E.

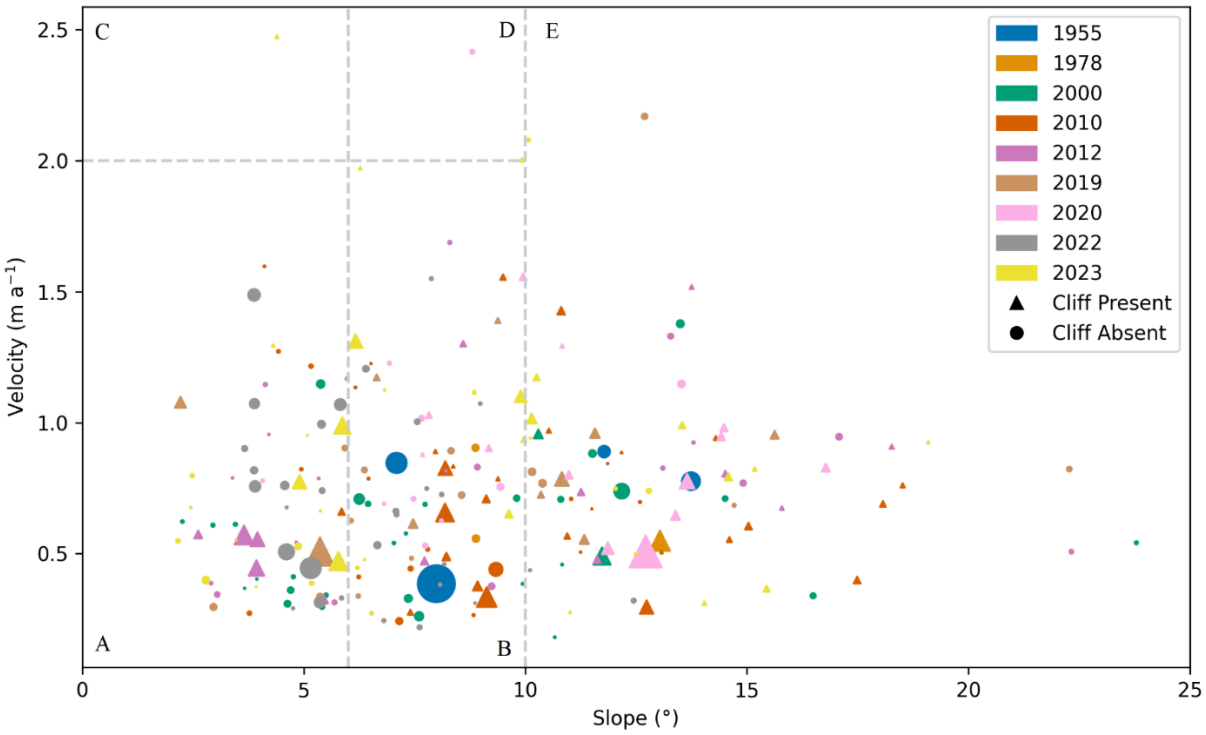

Figure 16 - Location of supraglacial ponds by cliff presence, year and area based on surface velocity and slope gradient of debris-covered glacier on Tapado Complex. In which colors represent the years, shape format represents the cliff presence and shape size represents proportioned pond area. The red line divided slopes gradient into low velocity and low gradient (Category A), low velocity and high gradient (Category B), high velocity and low gradient (Category C), high velocity and high gradient (Category D) and very high gradient (Category E). Elaborated by author, threshold values based on Reynolds et al. (2000).

Mostly supraglacial ponds are not necessarily found in those given categories. A threshold of velocity < 1.5 m^{-1} and gradient < 14° accounts for 82.90% of all mapped ponds, ranging from 100%, in 1955 and 1978, to 75.760%, in 2023, of total ponded area in the threshold zone. As velocity increases from 1.5 ma^{-1} threshold, pond density exponentially decreases independently of surface gradient. Below 1.5 ma^{-1}, surface gradient exerts a strong secondary control on density and size coupled with the surface velocity, as density and size decrease considerably above 14° and no ponds were found above 25° independently of surface velocity values.

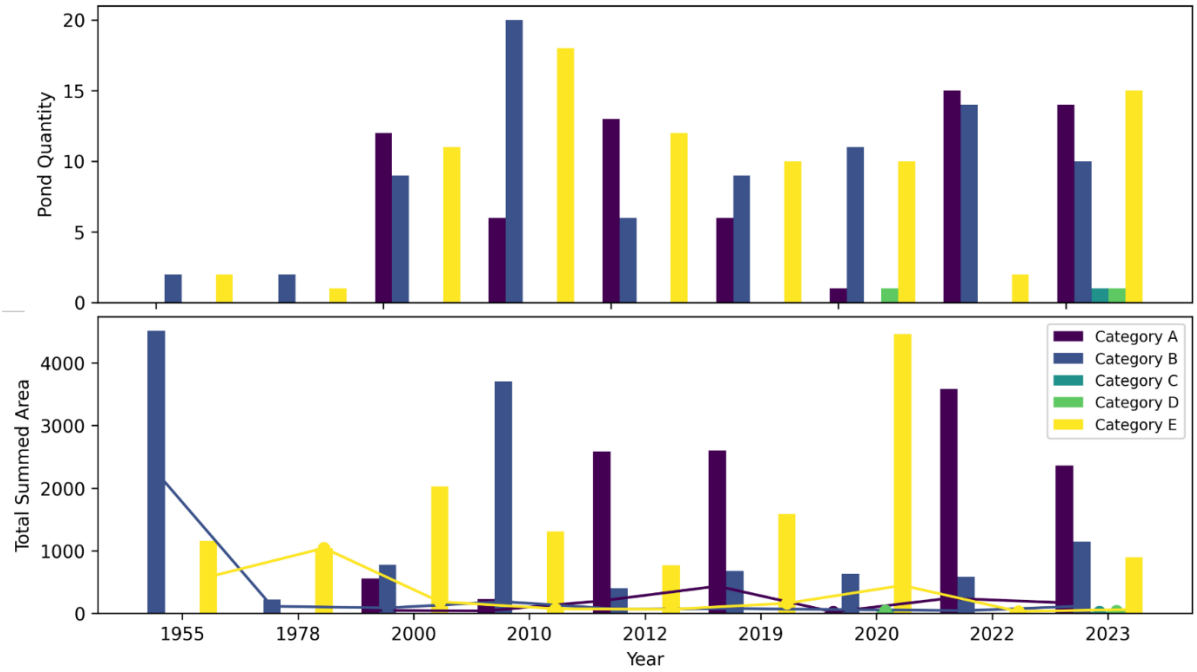

Figure 17 – In figure a supraglacial pond quantity is separated by each location class. Figure b shows the total summed area of each class in the bar plots, while the color respective lines represent the mean area of supraglacial pond for its classes. Elaborated by author.

Cliff presence seems to have lower incidence in Category A, B, C and D, as only 42 supraglacial ponds with cliff presence were present, against 111 supraglacial ponds without cliff presence. In Category E the opposite is seen, meaning cliff presence could have some influence for pond development above 10°, as there were 45 supraglacial ponds with cliffs against 36 ponds without cliffs. Figure 17 shows the quantity of supraglacial ponds, total and mean area of supraglacial ponds per category based on figure 16.

Pond quantity per category follows B > E > A > D > C, in which total pond quantity is 83, 81, 67, 2, 1 respectively, however, in total pond area it turns to be E > B > A > D > C. In any case, Categories A and B hold together a higher percentage and area than any of other categories. Saying that, it is important to note that pond quantity is not related to total occupied area. As for example, 2023 and 2010 display a high quantity of ponds in Category E, but quite low total ponded area; meanwhile, 2020 displays a medium number of ponds and the highest total area in Category E.

6.2 Surface lowering from supraglacial ponds and ice cliffs

Surface elevation changes were analyzed in four different periods: 1955 to 1978, 2000 to 2012, 2015 to 2020 and 2020 to 2023. Figure 18 shows that from supraglacial pond area to 30 m from those features, surface elevation mean change was negative in all the years. However, as

distance from ponds increases, elevation mean changes tend to become positive again. This inversely relationship highlights the influence of ponds and cliffs on the glacier wasting. After 15 m distance, surface elevation changes seem to homogenize across all the years, thus, average change at pond surface is -1.84 ± 0.48 ma^{-1}, while at 30 m distance it is -0.60 ± 0.53 ma^{-1}. This means that supraglacial ponds exert a strong influence within 15 m from its area.

The year 2021 presents the highest average changes (-1.07 ± 0.32 ma^{-1}), ranging from -2.07 ± 0.28 ma^{-1} at pond surface to -0.48 -± 0.32 ma^{-1} at 30 m distance. The years of 2009 and 2012 show the lowest changes in elevation (-0.28 ± 0.46 ma^{-1} and -0.28 ± 0.45 ma^{-1}, respectively), ranging from -0.33 ± 0.46 to -0.21 ± 0.45 ma-1 and -0.37 ± 0.46 to -0.18 ± 0.45 ma^{-1}, respectively.

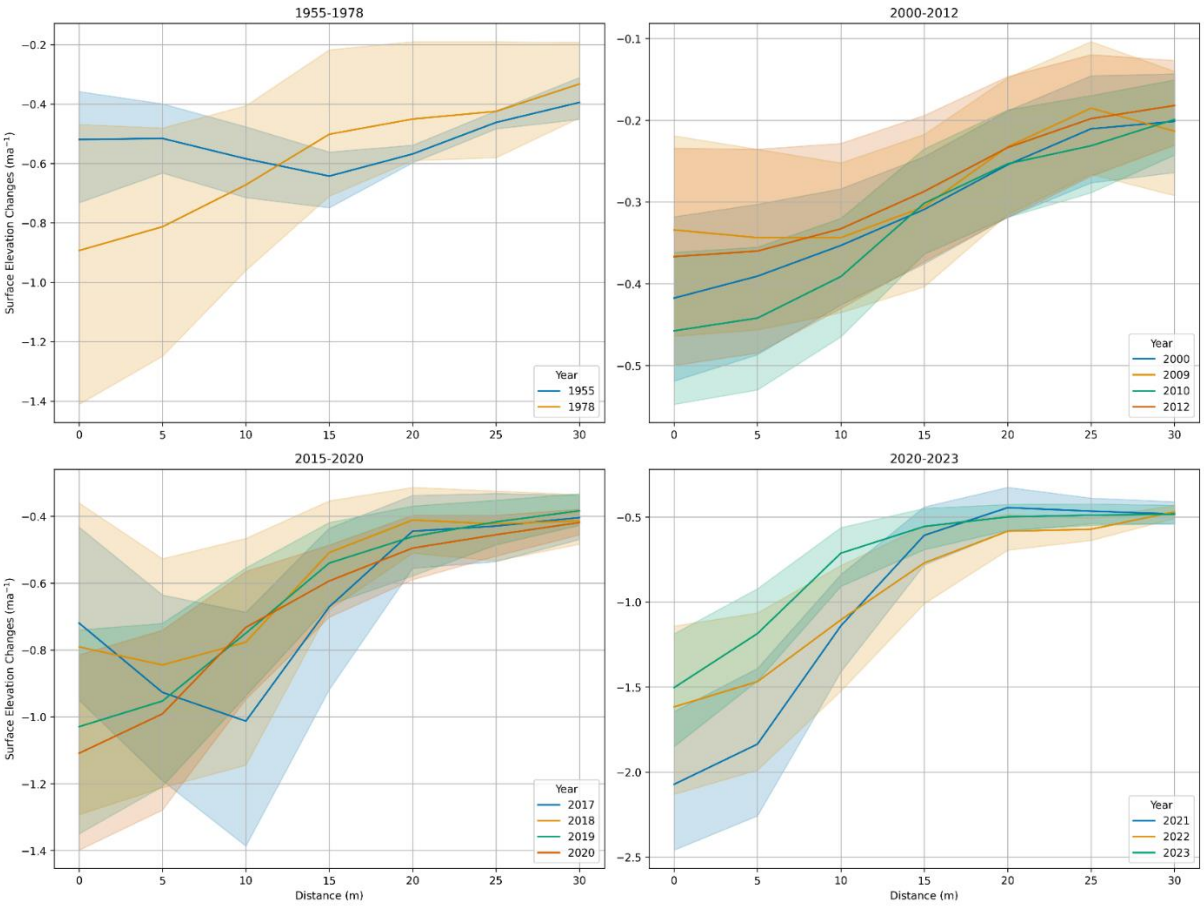

Figure 18 – Surface elevation changes related to supraglacial ponds for each year of data from pond's location to 30 meters distance. The distances were calculated within concentric circles of 5 meters radius in between distances. Elaborated by author.

In the two most recent periods, ponds and ice cliffs contributed mostly to the wasting of the glacier, with a mean of -0.90 ± 0.31 ma^{-1} and -0.64 ± 0.17 ma^{-1}, for 2020-2023 and 2015-2020

respectively, as seen in Figure 19. In 2000-2012, ponds and ice cliffs have an average contribution of -0.30 ± 0.45 ma^{-1}, even demonstrating one of the highest numbers of supraglacial ponds. Lastly, even with only 7 ponds, in the period of 1955-1978 their average contribution was of -0.55 ± 0.30 ma^{-1}.

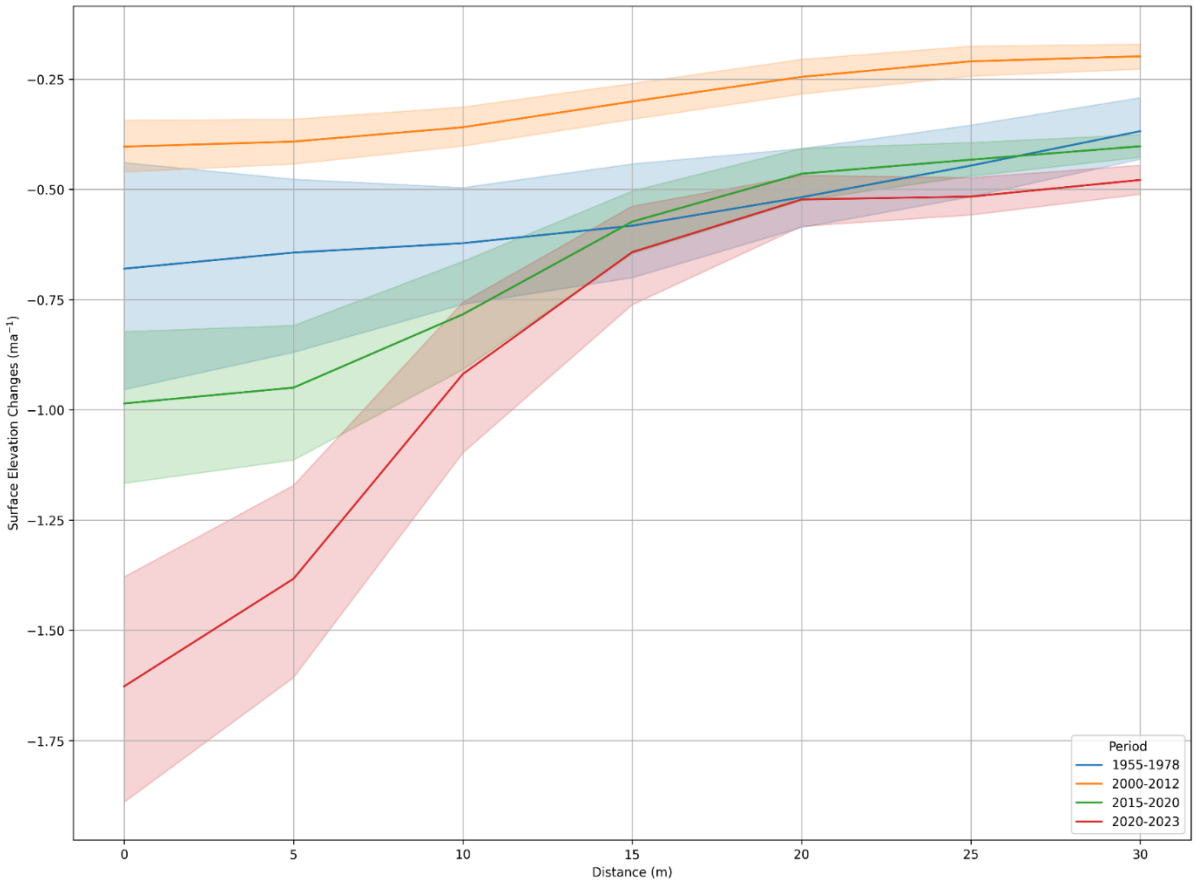

Figure 19 - Surface elevation changes related to supraglacial ponds for each period analyzed from pond's location to 30 meters distance. The distances were calculated within concentric circles of 5 meters radius in between distances. Elaborated by author.

The 15 m threshold of pond influence on surface elevation changes is also clearly visible when analyzing the periods as whole. From 0 to 15 m, elevation change decreases in -1.00 ± 0.51 ma^{-1}, while from 15 to 30 m it is only -0.23 ± 0.53 ma^{-1}. It is clearly defined the area of influence of supraglacial ponds on surface lowering, in where more dynamic changes occur below 15 m in all years analyzed, and in distances > 15 m the surface lowering tends to homogenize in between all analyzed datasets. The same threshold was applied to estipulate the influence area of cliffed and non-cliffed ponds for surface elevation changes, as in Figure 20.

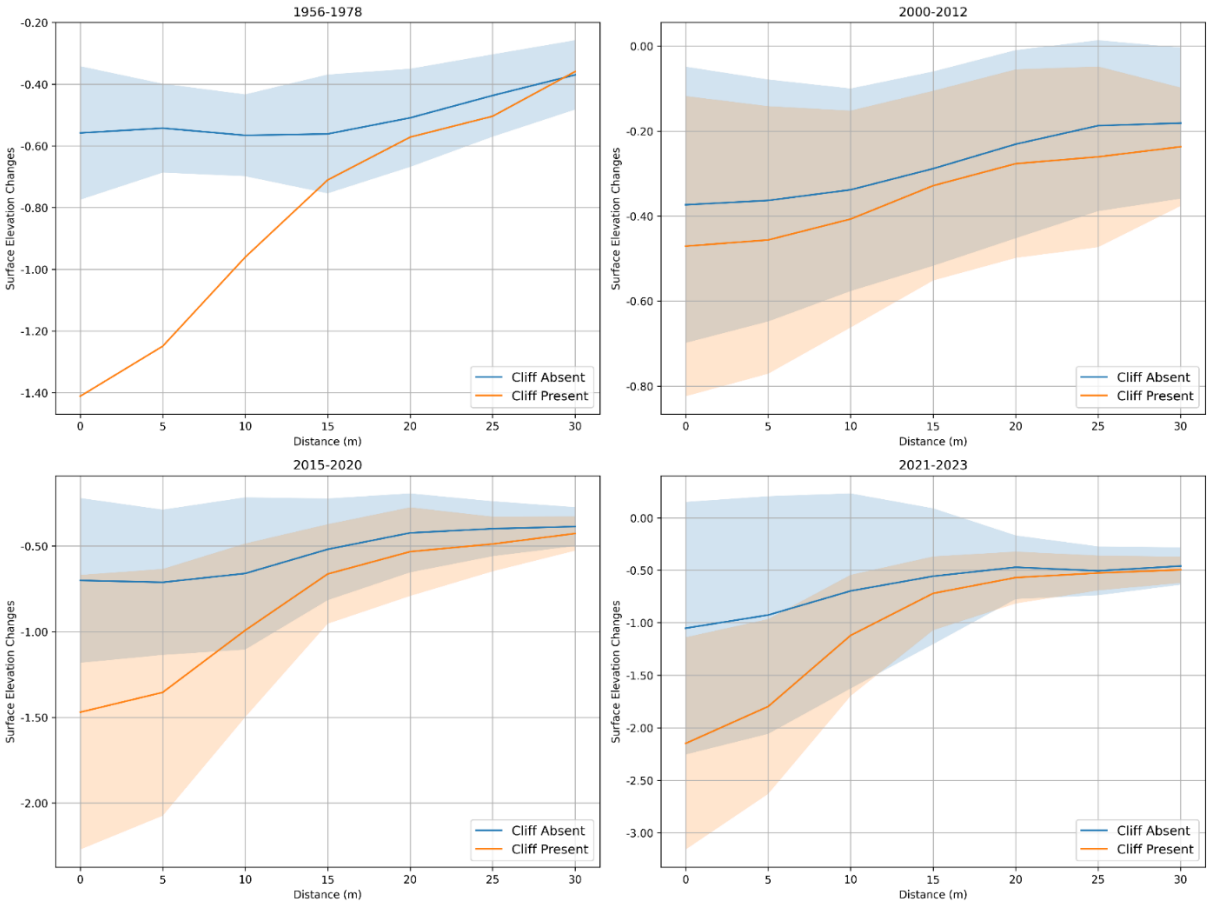

Figure *20* - Surface elevation changes related to pond presence within supraglacial ponds for each period analyzed from pond's location to 30 meters distance. The distances were calculated within concentric circles of 5 meters radius in between distances and cliff presence was manually assigned based on optical resolution. Elaborated by author.

As photogrammetry can commit some errors at water surfaces, Table 10 summarizes the mean and total elevation changes around the ponds by cliff and threshold distance without considering changes occurred on water surfaces. A huge influence of ice cliffs seems to take place in between pond boundary and 15 meters from pond boundary, with average difference up to 0.48 ± 0.32 ma^{-1} in between ponds with cliff presence and ponds with no cliff presence. After the distance threshold, the difference between cliff and no cliff pond related lowering decreases: 0.08 ± 0.3 ma^{-1}, 0.06 ± 0.45 ma^{-1}, 0.08 ± 0.17 ma^{-1} and 0.05 ± 0.31 ma^{-1} for 1955-1978, 2000-2012, 2015-2020 and 2020-2023, respectively.

Lowering experienced in the surroundings of supraglacial ponds with the existence of ice cliffs are considerably higher than the ones experienced by ponds without the presence of ice cliffs. The threshold of 15 meters also perfectly fits for cliff presence, in which areas > 15 m does not experience much difference in lowering independently of ice cliffs. Thus, the previously

pointed supraglacial pond influence area could be surface lowering induced by ice cliff presence instead.

Table 11 – Surface elevation changes from 0 to 15 m and 15 to 30 m in areas occupied by supraglacial ponds, showing the influence of ice cliff presence in the lowering rates.

		Surface Elevation Changes (ma-1)				
Period	Cliff Presence	Mean Change	Mean Error	Total Change	Total Error	Distance (m)
1955-1978	N	-0.56	±0.31	-10.01	± 5.54	0-15
	Y	-0.97	± 0.29	-2.92	± 0.86	
	N	-0.44	± 0.3	-7.89	± 5.33	15-30
	Y	-0.48	± 0.29	-1.43	± 0.86	
2000-2012	N	-0.33	± 0.45	-91.10	± 125.24	0-15
	Y	-0.40	± 0.47	-47.69	± 55.87	
	N	-0.20	± 0.45	-55.17	± 123.71	15-30
	Y	-0.26	± 0.45	-30.99	± 54.31	
2015-2020	N	-0.63	± 0.18	-77.62	± 21.8	0-15
	Y	-1.00	± 0.19	-72.27	± 13.48	
	N	-0.40	± 0.17	-49.65	± 21.48	15-30
	Y	-0.48	± 0.18	-34.81	± 12.81	
2020-2023	N	-0.73	± 0.10	-87.20	± 12.29	0-15
	Y	-1.21	± 0.11	-160.08	± 14.74	
	N	-0.48	± 0.11	-57.46	± 12.74	15-30
	Y	-0.53	± 0.11	-70.03	± 14.50	

Finally, it is possible to compare surface elevation changes experienced on ice cliffs, supraglacial ponds with cliffs and supraglacial ponds without cliffs, for the threshold > 0 and < 15 m distance, with the changes observed in the Tapado Complex, as seen in Figure 21. The analyzed features experienced massive mean elevation changes in relation to other parts in Tapado Complex. Ice cliffs show the highest surface elevation changes in 2020-2023 and 2015-2020, with -1.66 ± 0.40 ma^{-1} and -1.40 ± 0.20 ma^{-1}, respectively. Thus, ice cliffs contribute the most to downwasting, even if not associated with ponds. In 1955-1978 ponds associated with ice cliffs had slightly higher elevation changes values than ice cliffs, -1.08 ± 0.29 ma^{-1} against -0.96 ± 0.32 ma^{-1}, probably because the development of ice cliffs were not pronounced in this period.

Table 11 shows the magnitude of change if compared to the Tapado Complex, to the Tapado Glacier and to the debris-covered glacier, reaching rates up to ~48.88 times higher lowering than the whole complex in 2000-2012, when the Tapado Complex had a positive mass balance. The average magnitude compared with the Tapado Glacier, and debris-covered glacier is 5.55 and 5.14 times higher, respectively; being ~6.85, ~6.05 and ~3.74 times higher than lowering in Tapado Glacier, and ~6.53, ~5.38, ~3.49 times higher than lowering in debris-covered glacier, for ice cliffs, supraglacial ponds with ice cliffs and supraglacial ponds without ice cliffs. The ponds without cliffs, although they do enhance lowering by itself, are no near the damaged

caused by ice cliffs or ponds attached to ice cliffs, showing a magnitude ~45.32 – 46.57% lower than ice cliffs.

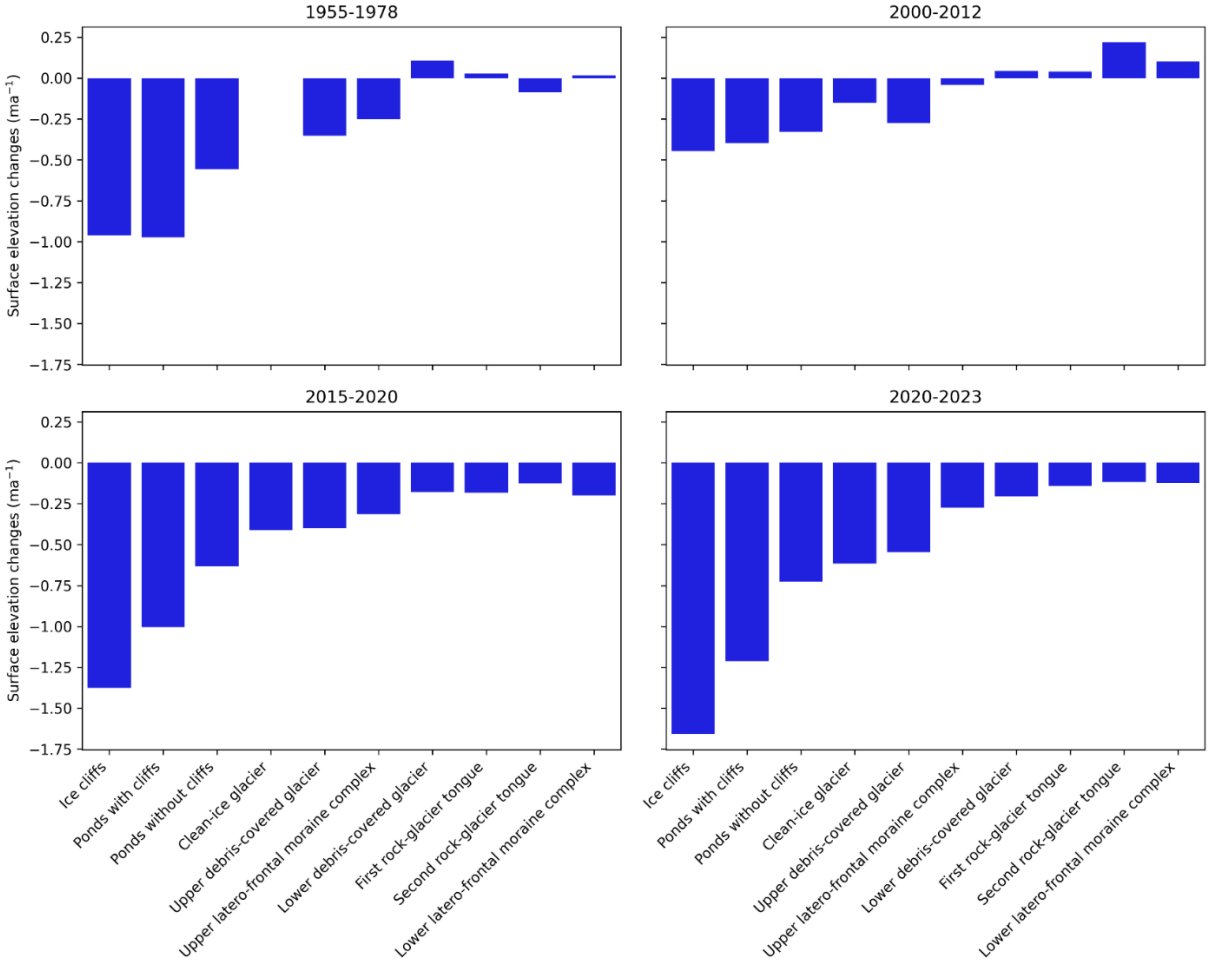

Figure 21 – Surface lowering experienced in Tapado Complex, highlighting the surface lowering occurred in ice cliffs, supraglacial ponds with cliffs and supraglacial ponds without cliff.

Table 12 – Magnetude of surface lowering experience by ponds without cliff, ponds with cliff and ice cliff ares in comparison with lowering experienced in the Tapado Complex, Tapado Glacier and debris-covered glacier.

			Tapado Complex	Tapado Glacier	Debris-covered glacier
Period	1955-1978	Ponds without cliff	7.20	6.81	4.53
		Ponds with cliff	14.00	13.26	8.81
		Ice cliffs	12.41	11.75	7.81
	2000-2012	Ponds without cliff	36.19	2.59	2.85
		Ponds with cliff	43.57	3.12	3.43
		Ice cliffs	48.88	3.50	3.85
	2015-2020	Ponds without cliff	2.44	1.92	2.19
		Ponds with cliff	3.88	3.05	3.48
		Ice cliffs	5.32	4.18	4.78
	2020-2023	Ponds without cliff	7.53	4.78	5.81
		Ponds with cliff	12.57	7.98	9.70
		Ice cliffs	5.74	3.64	4.43

6.3 Point distance on 3D modelling for ice cliff backwasting

Dense point cloud analysis was performed in two different areas, as previously stated in Figure 2. The ice cliff area 1 had the longest temporal observation (2019 to 2023, excluding the year 2021) and consists of the one supraglacial pond connected to an ice cliff, that collapsed in between 2020-2022. Ice cliff area 2, containing three different cliffs, only had surveying in 2022-2023. Thus, M3C2 point distance analysis was performed in the periods 2019-2020, 2022-2023 and 2020-2023 for area 1 (Figure 23), and in the period 2022-2023 for area 2 (figure 22).

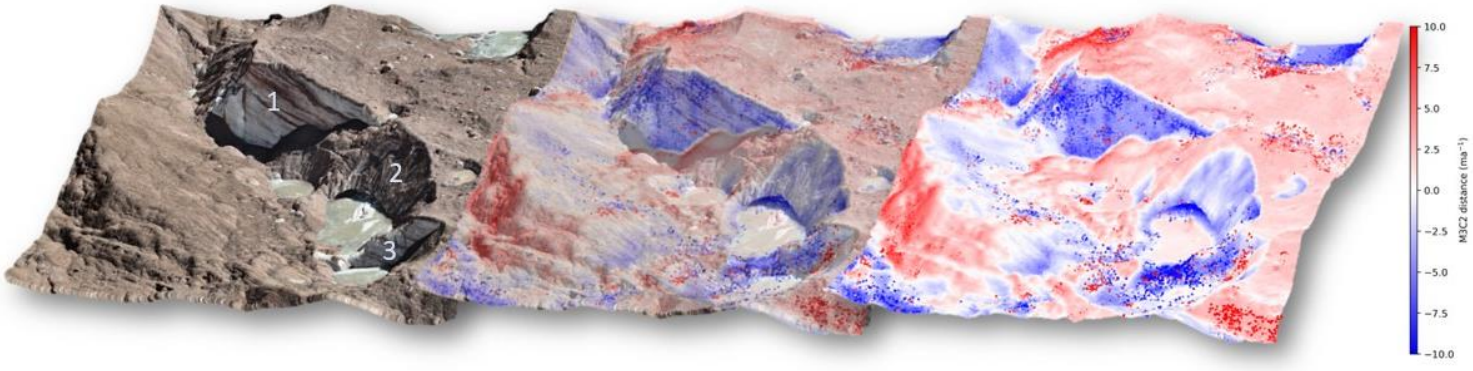

Figure 22 - M3C2 yearly distances in meters from dense cloud pair 2022-2023 for cliff area 2. On the left is the dense cloud point represented in RGB. Source: author.

Surface changes on exposed ice are observed to be higher in the analyzed areas, with mean changes of -2.91 ± 0.02 ma^{-1}, -2.65 ± 0.02 ma-1 and -4.10 ± 0.03 ma^{-1} for ice cliffs 1, 2 and 3 in Area 2, while changes in Area 2 were of 0.23 ± 0.23 ma^{-1}. The yearly rates were mathematically extrapolated, as surveys happened with only 105 days in difference between 2022 and 2023.

In Area 1 the same happens, areas with exposed ice experiences more changes than surrounding, with changes ranging from -1.67 ± 0.01 ma^{-1} to -5.08 ± 0.04 ma^{-1} in 2020-2022 and 2022-2023, respectively. However, it is known that between 2020-2022 the cliff went through a conduit collapse, as visualized in the bottom images in Figure 23. The bottom left image from 2020 shows a highly developed ice cliff, while in the bottom center image the whole area subducted. It is interesting to note that in the bottom right image, from 2023, cliffs started to develop again, although no supraglacial pond was formed since then.

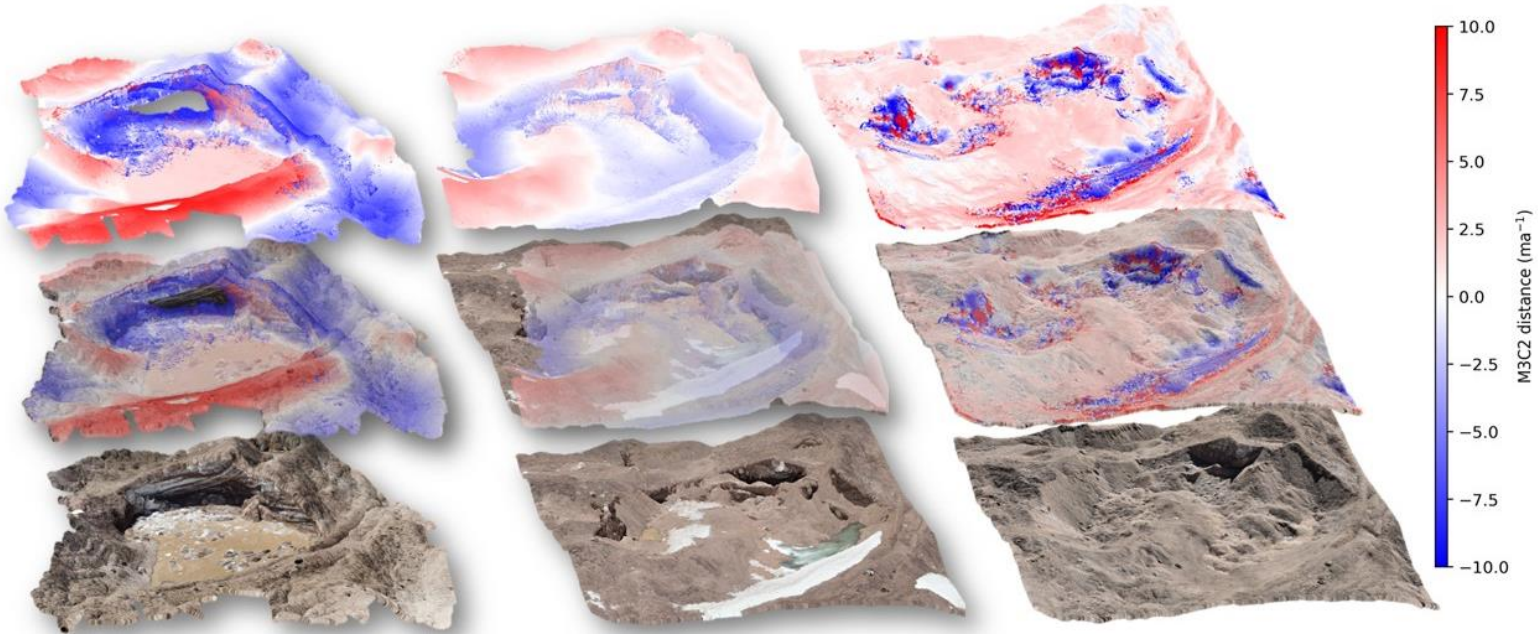

Figure 23 – M3C2 yearly distances in meters from dense cloud pairs 2019-2020 (left), 2020-2022 (center) and 2022-2023 (left). On the first row (bottom) there is the dense cloud point represented in RGB from 2020 (bottom left), 2022 (bottom center) and 2023 (bottom left). Source: author.

This collapse event can be spotted in Table 12, as the period of 2020-2022 has an overall surface change of ~-0.47 ma^{-1}, while other in other periods positive changes ranged from ~0.23 to ~0.29 ma^{-1}. In addition, Area 1, localized near the terminus of the glacier, seems to be more active, experiencing higher losses in elevation and horizontally, than area 2, localized higher up in the debris-covered glacier.

Table 13 – M3C2 distances calculated in the exposed ice and whole area. As surveys were not taken precisaly with a year difference, the annual rates were mathematically exrapolated.

				Mean			
Location	Feature	Period	Days (count)	M3C2 distance (m)	M3C2 distance (ma-1)	M3C2 distance (cmd-1)	Uncertainty (ma-1)
Area 1	all area	2019-2020	342	0.08	0.29	0.08	0.01
	cliff			-3.89	-4.14	-1.13	0.01
	all area	2020-2022	1016	-0.13	-0.47	-0.13	0.00
	cliff			-4.64	-1.67	-0.46	0.01
	all area	2022-2023	105	0.07	0.26	0.07	0.02
	cliff			-1.46	-5.08	-1.39	0.04
	all area	2020-2023	1142	-3.89	-1.25	-0.34	0.00
	cliff			-7.69	-2.46	-0.67	0.01
Area 2	all area	2022-2023	105	0.07	0.23	0.06	0.23
	cliff 1			-0.84	-2.91	-0.80	0.02
	cliff 2			-0.76	-2.65	-0.73	0.02
	cliff 3			-1.18	-4.10	-1.12	0.03

7. Discussion

7.1 Area changes and distribution comparison with glaciological studies

Steiner et al. (2019) studying the Langtang catchment in the Himalayas, found a mean area of 845 m^2 for cliffs and 475 m^2 for ponds in 2006-2015, while Miles et al. (2017a) found a mean area of 3,700 m^2 for the Langtang Valley in 1999-2013 for ponds. Taylor et al. (2021) found an average pond area of 1,206 m^2 for ponds in Bhutan region. Chand and Watanabe (2019) observed a mean pond size of 700 m^2 in the years 2015 and 2016 within 23 glaciers in the Everest region. Sato et al. (2021), Loriaux and Ruiz (2021) and Chen et al. (2021) provided only total area, as seen in Table 13.

Table 14 – Summary of area extent and distribution of supraglacial ponds and debris covered glacier related to Tapado Glacier.

References	Cliff area (m2)	Pond area (m2)	Region	Glacier area (km2)	Pond cover (%)	Cliff cover (%)	Extra Notes
Brun et al. (2018)	~70000*	-	Changri Nup Glacier	~1.49**	-	~7 - 8%	
Steiner et al. (2019)	~845	~475	Langtang	80.6	~1.1 - 2.1	~0.2 - 3.8	Size of ponds with cliffs are 12-33% higher; 7% of ponds and 17% of cliffs persisted over a decade; 30 to 50% of ponds were attached to a cliff
Miles et al. (2017a)	-	~3700	Langtang	242.2	~0.08 - 1.69	-	45% of supraglacial pond persisted for multiple years; 58 to 69% of ponds were attached to an ice cliff
Taylor et al. (2021)	-	~1206	Bhutan	25.8	~0.3 - 3.5	-	Only 19 to 29-9% of ponds were attached to an ice cliff
Chand and Watanabe (2019)	-	~700	Everest	~254.3	~0.03 - 3.24	-	
Loriaux and Ruiz (2021)	~82364*	~13517*	Verde Glacier	~8.15	~0.07 - 0.44	~1.29 - 2.70	
Sato et al. (2021)	~14214 - 18128*	~11526 - 13260*	Trakarding Glacier	~31.7	~0.4 - 0.5	~4.7 - 6.1	Up to 83% of ponds were attached to an ice cliff
Chen et al. (2023)	~720000*	~490000*	Everest	~53.29	1.34	1.96	

*Only total area occupied by features were provided
**Only debris-covered glacier area was provided

The observed mean pond and cliff size for Tapado Complex were 202.71 ± 55.45 m^2 and 270.33 ± 73.75 m^2., while total area varied from ~1263.27 – 7246.25 m2 for ponds and ~0 – 6691.13 for cliffs. These values are significantly lower than most observations in other regions. We need to consider here that Tapado Glacier is a small glacier, with only 1.44 km^2 and a debris-covered section of 0.54 km^2. In those references, mapped area ranges from 25.8 km^2 to 242.2 km^2, with single glaciers up to 93.7 km^2. All the analyzed ponds, but Loriaux and Ruiz (2021), are localized in the Himalayas, this is, glaciers in a region with strong monsoon effect, which contribute tremendously to water intake within the glacier catchment. In the case of Verde Glacier, it is localized in South Chile, a region also characterized for high water availability. As mentioned, Tapado Glacier is placed in a semi-arid region in critical desertification process. Then, it is expected that total pond area extent in Tapado Glacier is lower as it is.

Even though Tapado Glacier is small, the mean pond cover, ranging from 0.24 to 1.37% of debris-covered glacier surface, in the recent years, is relatively high if we compare to results as Sato et al. (2021) and Loriaux and Ruiz (2021), but it is in order with Himalaya observations in general. However, ice cliff cover in the debris-covered glacier in Tapado Glacier is lower than other observations, ranging from 0 to 126%, while Brun et al. (2018) attributed an ice cliff cover of 8% to Changri Nup Glacier. This lower ratio of ice cliffs could be correlated to the low persistence of supraglacial ponds – 68.8% of supraglacial ponds are only present in one dataset –, which means that calving dynamics in between ponds and cliffs are also not prolonged, thus, ice cliffs have its development retarded with the drainage events of ponds.

The frequency of multi-year ponded area is under the average in Tapado Glacier, while 45% of supraglacial persists over multiple years (Miles et al, 2017b) and 7% of ponds persisted over a decade (Steiner et al., 2019) in Langtang catchment, only 14.53% of ponds in Tapado persists within 2 datasets, and within 6 datasets this number goes down to 1.97%. Chand and Watanabe (2019) previously related that ponds in small glaciers in relative higher slopes tend to be less persistent for a longer time period.

Nonetheless, supraglacial ponds in Tapado are highly linked to ice cliffs, as seen in major glaciers in the Himalayas, with a percentage of ~41% intersection in between features, which in other topographic conditions could lead to an even higher ice cliffs development. We can assume, then, that those topographic conditions, specifically the surface gradient of 17.8° in the debris-covered glacier, retards ice cliff formation and, consequently, glacial wasting.

7.2 Surface velocity and surface gradient as drivers for pond formation

The debris-covered glacier in Tapado is nearly stagnant, with mean surface velocity of 0.73 ± 0.56 ma^{-1}. Mean surface velocity at pond location is 0.78 ± 0.32 ma^{-1}, with no mean surface velocity > 1 ma^{-1}, as seen in figure 24. In glaciers in Himalayas surface velocities under 3 ma^{-1} are considered stagnant velocities and between 3 and 10 ma-1 is considered near stagnant velocities (e.g., Miles et al., 2017b; Quincey et al., 2007), as in the Langtang catchment Miles et al. (2017b) classified low velocities as < 7.5 ma-1 and found ponds at velocities up to 30 ma^{-1}, Quincey et al. (2007) measured velocities ranging from 25 to 35 ma-1 at the Tama Koshi basin, Benn et al. (2009) observe average velocities of 10-15 ma^{-1} for the Khumbu Glacier. In other regions, those high surface velocities seems to persist: Louriaux and Ruiz (2021) observed valued up to 55 ma-1 and classified low velocities as < 17 ma^{-1} for Verde Glacier,

Röhl (2008) identified ponds where velocity reaches 80 ma^{-1} in Tasman Glacier, and Stefaniak et al. (2021) discovered a average velocity of 12 ma^{-1} for Miage Glacier.

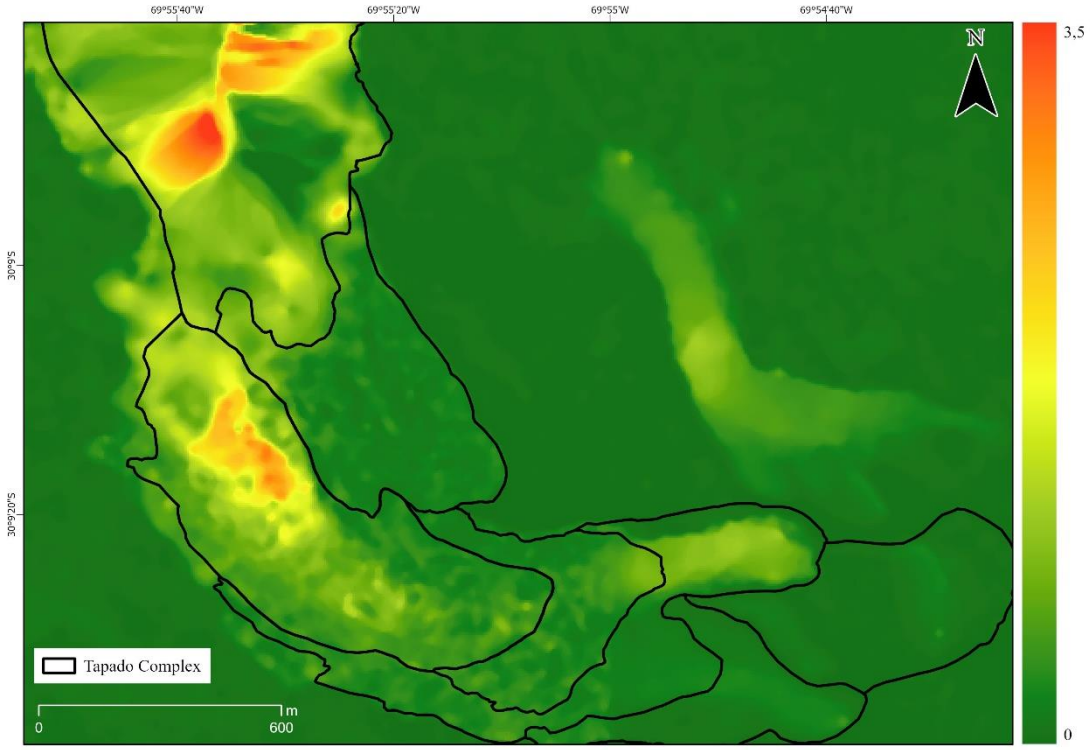

Figure 24 – Surface velocity of Tapado Complex extracted by cross-correlating features between 2012 and 2020. Source: Robson et al. (2022).

Quincey et al. (2007) described that stagnant ice with gradient > 2° would have no opportunity for reorganization of drainage conduits through flow, as steeper hydraulic gradient aids drainage and lake development would be unlikely. However, the debris-covered glacier in Tapado Glacier has similar pond coverage percentage than the glaciers in the Himalayas, even though it presents stagnant velocities and mean surface gradient at debris-covered area is > 17°. Some other discordant observations were made in the past, Stefaniak et al. (2021) found high density of ponds in contact with ice cliffs with elevated gradient slope and nearly stagnant velocity (< $3ma^{-1}$) at the southern lobes of the Miage Glacier.

Miles et al. (2017b) and Benn et al. (2009) suggested that a velocity decay down-glacier can lead to a zone of longitudinal compression, which crevasses and relict conduits may be forced to close, thus, pond drainage, after water accumulation in the thermokarst depression, would likely be enabled only by hydrofracturing. The intersection relationship of ice cliffs and supraglacial ponds can also collaborate for this hypothesis, once 115 cliffs intersected supraglacial ponds in the scenes, 127 cliffs were within one meter distance and 135 cliffs were within two meters distance. Ice cliffs formation seems to be heavily marked by pond presence

and unlikely to originated from crevasses – which, in theory, would be closed by longitudinal compression.

The surface velocity in the upper part of the debris-covered glacier (red and yellow in Figure 24) has a mean surface velocity of 2.24 ± 0.32 ma^{-1}, while the bottom part of the clean ice glacier reaches means of 2.71 ± 0.48 ma^{-1}, it is approximately 1.46 and 1.93 times higher than the velocities found at pond location, and 1.51 and 1.98 times higher than the mean velocity at debris-covered glacier zone, respectively. This velocity relationship could indicate that our debris-covered glacier has been suffering from longitudinal compression. In other words, there are indicatives that higher velocities upwards compress the regions of lower velocities downwards.

The second particularity of Tapado is, as mentioned, the high surface gradient. Supraglacial pond distribution in Tapado Complex does not entirely follows Reynolds (2000) proposed classification based on surface gradient, in which glaciers with gradients in the range 2°–6° are expected to experience widespread dispersed ponding, with those in the range 6°–10° expected to exhibit isolated small ponds, and above 10° meltwater would be able to drain away. Observations in Tapado Glacier are also not totally concordant with other regional or Himalaya observations.

Miles et al. (2016) classified 36% of the observed supraglacial pond area as category A, 44.3% of pond area is as category B, 5.2% lies under our category C, and 18.3% of pond area is within category D. The percentage of pond area follows similar pattern (B > A > D > C) in Tapado Complex, if excluded the category E (slopes > 10°). Category E, where gradient is higher than 10°, was not observed in Miles et al. (2016). Although, in areas where surface velocity is < 2 ma^{-1}, as in Ghana glacier, there are ponds exactly at 10°, even though the mean glacier surface is below 10°.

Loriaux and Ruiz (2021) defined that at Verde Glacier 14, 74 and 12% of the ponds were observed on slopes <2°, between 2°–6° and between 6°–10°, respectively. However, pond area in Verde Glacier reaches 6000 m^2 per pond. In our glacier, the biggest pond reaches only 3465 ± 1093 m^2, with only 6 ponds > than 1000 m^2. In addition, Verde Glacier's velocities reach up to 50 ma^{-1} and low velocities were considered < 17 ma^{-1}, allowing large pons formation only in gradient < than 6°. Röhl (2008) has also not found any ponds above 10° at Tasman Glacier, in New Zealand.

Table 15 – Summary of findings relate to surface velocity and surface gradient in relation to Tapado Glacier.

		Surface Gradient (%)	
	Velocity (ma-1)	< 10°	> 10°
Miles et al. (2017b)	up to 30	100	-
Quincey et al. (2007)	25 to 35	100	-
Benn et al. (2009)	10 to 15	-	-
Loriaux and Ruiz (2021)	up to 55	100	0
Röhl (2008)	up to 80	100	0
Stefaniak et al. (2021)	12 (average)	-	-
Sahu et al. (2023)	-	85	15
Chand and Watanabe (2019)	-	87	13
Tapado Glacier	0.56 to 0.93	65.4	34.6

Some studies, however, have previously dealt with moderate pond cover in debris-covered glaciers that experience surface gradient higher than Reynolds (2000) and Quincey et al. (2007) thresholds. Sahu et al. (2023) classified supraglacial ponds in Himalaya-Kararoram region found that 85% of ponds are localized in between 0°-10° in 2020, meaning that 15% of ponds are placed above the threshold of 10°, however no specific analysis was made on those supraglacial ponds. Chand and Watanabe (2019) observed few glaciers in the Everest region, in which 12 glaciers had mean surface gradient higher than 10° and 13% of supraglacial ponds were in slopes higher than 10°, again no further analysis was made in those ponds.

Quincey et al. (2007) also pointed those areas only isolated smaller ponds area found, not connected to the englacial hydrological system and are more likely to remain perched, as their level is controlled by local structures and the morphology of the glacier surface. Chand and Watanabe (2019) classified ponds < 0.1 km2 as small and less hazardous ponds and omitted 45% of ponds smaller than 0.005 km^2. This seems to be a scale originated problem, once supraglacial ponds in Himalayas can reach up to 0.96 km^2 (Quincey et al., 2007) and mean areas of 0.0037 km^2 (Miles et al., 2017b). Meanwhile, supraglacial ponds in Tapado are on average 0.0002 km^2, with only 3.86% of ponds being bigger than 0.001 km^2. It is also difficult to precisely define a threshold of what is a small pond for those authors, thus, it's only possible to assume that supraglacial ponds of the size as the ones in Tapado are mostly not considered in those analyses.

Another singularity of Tapado Glacier is that velocity exerts stronger control on pond size and density than surface gradient, as 190 ponds with approximately mean area of 177.21 m^2 are located below 1 ma^{-1}, against 44 ponds with approximately mean area of 97.95 m^2 located in

areas above 1 ma^{-1}. Zones above 2 ma^{-1} have only 5 ponds with approximately mean area of 40.34 m^2. This velocity dependency for pond development in a longitudinal compression context, which closes englacial conduits down glacier and reroutes meltwater onto the glacier surface, added to near-stagnant velocities and small glacierized area could, again, explain the presence of perched supraglacial ponds in elevated surface gradients.

Therefore, findings here partially disagree with Reynolds (2000) and Quincey et al. (2007) framework, based on Himalayas glaciers, that surface gradient exerts primary control on pond formation and development. Miles et al. (2016) previously described the strong control that surface velocity exerts on pond persistence by encouraging connectivity between the supraglacial and englacial hydrologic systems. However, pond density and size increase with lower surface gradient, exerting the role of secondary control on pond formation, as zones above 14° contain less than 10% of ponds and 5.65% of total area, meaning that meltwater is finally able to drain away even in stagnant velocities and compressive flow.

Other combability in between analysis were found, in Category C and D the lowest number of ponds were found (0.42 and 0.85%. respectively), corroborating Quincey et al. (2007) classification. Although only 3.86% of ponds being > 1000m^2 – in which 1.75% are found in 2017 and 2018, years without a surface gradient input. However, Category B was not related to potentially large ponds as expected, classifying once more Tapado Glacier as a glacier of small and perched supraglacial ponds. Such disparity between the Tapado and Himalayan examples suggests substantial regional variations of contributions to ice cliff and supraglacial pond formation, as for different scale of analysis that collaborates to different precepted trends and dynamics.

7.2 Surface elevation changes comparison with glaciological studies

In the Peruvian Andes, Wigmore and Mark (2017) observed numerous elevation changes in the upper debris-covered glacier section of the Llaca Glacier, characterized by small ponds interspersed with debris piles. They associated the highest melt rates were associated with ice cliffs and surface ponds and assigned the biggest elevation change to an ice cliff collapse. Ragettli et al. (2016) linked cliff area and lake area to changes in mean thinning in Langtang catchment, as cliff area fractions higher than 10% where consistently linked to thinning acceleration, and maximum thinning acceleration corresponded to a relatively high lake area fraction of 6% in Lirung Glacier.

Further, Salerno et al. (2017) revealed that the surface lowering in the Khumbu region was due primarily to the surface slope gradient, which exhibited strong correlations with ice-flow velocity and secondary to proglacial ponds. However, Lamsal et al. (2017) observed a strong correlation between slower ice-flow velocities and surface lowering in Kanchenjunga Glacier, as surface is covered with debris mantle, the degree of surface melt is not a function of elevation. Their findings also corroborate to the correlation between cliff and pond density to the surface lowering, as a likelihood > 50% of supraglacial pond and cliffs coexisting along surface lowering (Lamsal et al. 2017).

Table 16 – Summary of the main findings of ablation, surface lowering and their magnitude in relation to supraglacial ponds and ice cliff presence.

		Ice cliff	Supraglacial pond	Ice cliff	Supraglacial Pond
Reference	Glacier	Ablation (%)		Occupied area (%)	
Sakai et al. (2000)	Lirung	-	3.4	-	0.43
Sakai et al. (2002)	Lirung and Khumbu	20	-	2.6	-
Thompson et al. (2016)	Ngozumpa	40	-	5	-
Röhl (2008)	Tasma	-	10	-	-
Stefaniak et al. (2021)	Miage	5	-	1.3	
Miles et al. (2018)	Langtang	-	12.5	-	1
Brun et al. (2018)	Changri Nup	23%	-	7 to 8	-
Buri et al. (2021)	Langtang	17%	-	2.1	-
		Surface lowering (ma-1)			
Stefaniak et al. (2021)	Miage	-3.48 to -377	-1.78 to -4.55	1.3	
Miles et al. (2018)	Langtang	-	0.2	1	-
		Magnetude			
Stefaniak et al. (2021)	Miage	4.09 to 8.42	3.96 to 8.05	1.3	
Brun et al. (2016)	Langtang	6	-	-	-
Kneib et al. (2021)	Langtang	14	-	0.6 to 2	3.3 to 9.2

In brief, Sakai et al. (2000) attributed 3.4% of total ablation to 0.43% occupied are by supraglacial ponds in the debris-covered area at Lirung Glacier. On Lirung and Khumbu glacier, Sakai et al. (2002) estimated ~20% of debris-covered glacier ablation to ~2.6% of cliffed area in the debris-covered glacier. More recently, Miles et al. (2018) estimated that ponds cover 1.0% of the debris-covered area, yet contribute to 12.5 % ± 2.0% of the annual mass loss and account for 0.20 ± 0.03 ma^{-1} of surface lowering. Complementary, Thompson et al. (2016) observed the largest surface elevation changes occurred at ice cliffs, contributing to approximately 40% of observed lowering.

Stefaniak et al. (2021) observed a surface elevation change from -3.48 to -3.77 ma^{-1} for ice cliffs and from -1.78 to -4.55 ma^{-1} for supraglacial ponds, with a magnitude of average surface lowering from 4.09 to 8.42 and 3.96 to 8.05 times higher than lowering in the whole glacier, for cliffs and ponds respectively. Even though cliffs and ponds occupied an area of 1.3%, they

were responsible for ~5% of total mass loss (Stefaniak et al., 2021). Complementary, focusing on the terminus area of the Tasman Glacier, Röhl (2008) attributed 10% of all ice loss at glacier's surface to supraglacial ponds.

The surface elevation changes related to ice cliffs and supraglacial ponds, as for percentage of area occupied by those features within the debris-covered glacier and the magnitude of lowering was summarized in Table 16 for better understanding and comparison with references.

Table 17 – Summary of main finding in Tapado Glacier, with average surface lowering, percentage of debris-covered glacier area occupied by features, and magnitude of lowering if compared to debris-covered section.

	Surface Lowering (ma-1)		Area (%)		Magnetude	
Period	Cliff	Pond	Cliff	Pond	Cliff	Pond
1955-1978	-0.96	-0.63	0.55	0.65	11.75	10.03
2000-2012	-0.44	-0.35	0.67	0.79	3.5	2.86
2015-2020	-1.37	-0.76	0.74	0.89	4.18	2.48
2020-2023	-1.65	-0.98	0.68	1	7.98	4.21
Overall	-1.11	-0.68	0.66	0.83	6.85	4.90

Tapado Glacier has experienced an overall lower surface elevation change if compared to the surface elevation Alps (Stefaniak et al., 2021), however it shows a higher surface elevation change than the one described in Miles et al., (2018). As summarized, ice cliff related wasting in the Himalayas seems to be the main source of lowering, where supraglacial ponds only act as support, while in the Tapado Glacier those averages are not that apart in between – probably related to the underdevelopment of ice cliffs due lack of persistence of perched small ponds, closing of crevasses, etc. The mean magnitude of average surface lowering is relatively close to the observed ones at Miage Glacier, even though the average lowering is lower, easily explained by the total glacier wasting and glacier size for each glacier.

Comparing with glacier mass balance observations in Robson et al. (2022), we see that an increase of ~-0.93 ma^{-1} on surface lowering on cliffed areas and of ~-0.41ma^{-1} on ponded areas, as for an increase of ~0.07% and ~0.1% in area, for cliffs and ponds respectively, follow the negative mass balance increase from ~-0.17 m $w.e.a^{-1}$ in 2000-2012 to ~-0.32 m $w.e.a^{-1}$ in 2015-2020.

Nonetheless, temperature, precipitation, and associated changes in ice flux data is necessary to complement the input drives for lowering and mass balance dynamics, as for pond and cliff

formation dynamics, and a continued monitoring is required to assess to what extent this represents a longer-term trend of enhanced thinning rates (Stefaniak et al., 2021). It is possible, though, to correlate ice-cliffs and supraglacial ponds to higher thinning rates in Tapado Glacier and Complex, as those features overlap with highest thinning rates, as exemplified in Figure 25.

The presence of the continuous debris cover at Tapado Glacier apparently does not retard mass loss, specially at the upper debris-covered glacier, where ponds and cliff are concentrated, as expected, once debris-cover glacier produces higher thinning rates than the nearby clean-ice. The debris-covered glacier is also experiencing an increase in those lowering rates, meanwhile the area percentage and thinning rates of ponds and cliffs are also increasing. According to Robson et al. (2022), areas of debris-covered ice have also experienced an increase in extent, probably due to the low surface velocities that cannot transport debris away. Thus, this study shows that ice cliffs and supraglacial ponds are a non-negligible term in the glacier thinning and, consequently, mass loss of Tapado Glacier. It is concerning, as in recent years the increase in those features haven't slowdown.

Finally, one of the main findings in this thesis was the threshold influence of ice cliff surface lowering to the surrounding areas of Tapado Glacier. It was determined supraglacial ponds with cliffs have highly negative surface lowering within an area < 15 m from the pond itself, while after this zone of 15 m, the lowering of supraglacial ponds with cliffs and supraglacial ponds without cliff tend to homogenize. This threshold was observed in all analyzed datasets, and further analysis could be done in other glaciers to generate comparative data.

The lowering rates in the debris-covered glacier, heavily enhanced by supraglacial ponds and ice cliffs, seems to promote some sort of debris-cover glacier anomaly, as diagnosed in the Himalayas (Pellicciotti et al, 2015; Lamsal et al., 2017; Brun et al. 2018). In Figure 21 we see that the surface lowering showcased in the upper debris-covered glacier is similar, and in some cases higher, than the lowering in the clean ice tongue. This can be explained by the presence of ice cliffs acting as local hotspots for melt, contributing disproportionally to the tongue average ablation, as ablation rates in debris-cover should be lower once thick debris act as insulation and reduces ablation rates (Immerzeel et al., 2014; Pellicciotti et al., 2015; Sakai et al., 2002; Steiner et al., 2015; Brun et al., 2018).

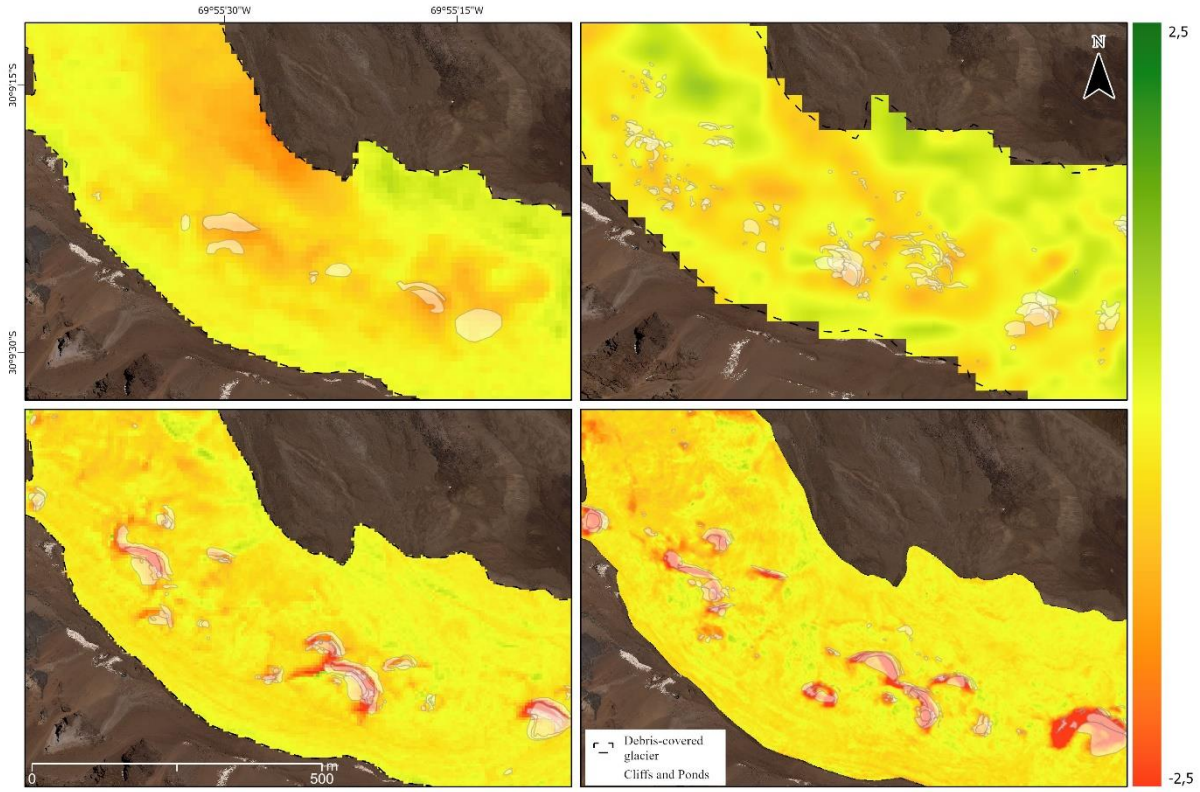

Figure 25 – Overlapping in between supraglacial ponds and ice cliffs to the dDEMs for better visualization of features location and lowering zones from 1955 to 2023. In the upper left is the period of 1955-1978, in the upper right is 2000-2012, in the bottom left is 2015-2020 and in the bottom right is 2020-2023. The dDEM from 1955-1978, 2000-2012, 2015-2020 were acquired from Robson et al. (2022).

7.3 Ice cliff 3D surface changes with M3C2 algorithm

The mean surface lowering acquired from dDEM for the same period (2020-2023) and location showed a value of -2.39 ± 0.361 ma^{-1}, while the M3C2 method attributed -2.46 ± 0.007 ma^{-1}. This means that the dDEM derived from high resolution satellite omitted 2.93% of surface lowering and proportioned an uncertainty of ~5057% higher than the error attached to the dense cloud point. Previously, Brunn et al. (2018) estimated an overestimation of ice cliff volume loss up to 9% from derived coarser imagery derived dDEM.

Altogether, seven main papers are compared to the findings in Tapado Glacier, in which six of them are placed in the Himalayas and one in the Miage Glacier, summarized in table 17. All the compared research utilized 3D methodology from UAV or LiDAR dataset, and three of those applied M3C2 algorithm to their melt rate estimations.

Table 18 – 3D ice cliff retreat references summarized with the main melt/retreat rates observed and associated with ice cliffs, as for the application of M3C2 algorithm.

Reference	Glacier	Melt rates	M3C2 (Yes/No)
Kneib et al. (2022)	Langtang	2.9 to 4.3 cmd^{-1}	Y
	24K	3.9 to 5.1 cmd^{-1}	
Buri et al. (2018)	Lirung	4.6 to 6.3 cmd^{-1}	N
Brun et al. (2018)	Changri Nup	3.88 to 3.91 ma^{-1}	N
		4.43 to 4.76 ma^{-1}	N
Sato et al. (2021)	Trakarding	> 2 ma^{-1}	N
Stainer et al. (2019	Langtang	4 to 5 cmd^{-1}	N
Watson et al. (2017)	Khumbu	0.30 to 1.49 cmd^{-1}	Y
		0.74 to 5.18 cmd^{-1}	
Stefaniak et al. (2021)	Miage	0.93 to 8.15 ma^{-1}	Y

The previously dDEM estimes of lower lowering within ice cliff surfaces for Tapado Glacier are proved once more with the highly accurate M3C2 method. While melt rates in the Himalaya's glaciers varies from -2.9 to -6.2 cmd^{-1} (Buri et al., 2018; Brun et al., 2018; Steiner et al., 2019; Sato et al., 2021; Kneib et al., 2022), the daily melt rates within the two analyzed cliff areas are no more than -1.30 cmd^{-1}. Watson et al. (2017) observed daily rates from -0.30 to -1.40 cmd-^{1} and -0.70 to -1.20 cmd^{-1} during winter season in the Khumbu Glacier, those rates are similar to the ones in Tapado Glacier during summer season.

The higher thinning rates present in 2022 and 2023 (-1.39 and -1.12 cmd^{-1} for Area 1 and 2, respectively) is probably due summer season, as surveys were done in December, 22 and April, 2023, thus only exponential retreat was computed, without the potential accumulation or lower retreat rates during winter season. However, it is only assumed and the reasons behind should be closely investigated as dDEM thinning rates are slightly higher in this period as well. Thus, without climate variables to understand deeper the cryosphere dynamics in Tapado Glacier, we can only partly explain the differences in retreat and lowering rate by morphological characteristics of the study site, as overly done already.

Table 19 – Main findings from M3C2 point distance analyzed performed in Area 1 and Area 2 of Tapado glacier summarized.

				Mean			
Location	Feature	Period	Days (count)	M3C2 distance (m)	M3C2 distance (ma-1)	M3C2 distance (cmd-1)	Uncertainty (ma-1)
Area1	cliff	2019-2020	346	-3.89	-4.14	-1.13	0.01
	cliff	2020-2022	1016	-4.64	-1.67	-0.46	0.01
	cliff	2022-2023	105	-1.46	-5.08	-1.39	0.04
	cliff	2020-2023	1142	-7.69	-2.46	-0.67	0.01
Area 2	cliff 1	2022-20023	105	-0.84	-2.91	-0.80	0.02
	cliff 2			-0.76	-2.65	-0.73	0.02
	cliff 3			-1.18	-4.10	-1.12	0.03

7.4 Uncertainties

Imagery resolution is a constant bias in the analysis, especially when working with a variety of datasets that do not share the same spatial resolution among all individual scenes. Planet imagery was considered a low-resolution imagery in contrast with Pléiades, Geoeye, Quickbird and UAV, promoting omissions and overestimations across the supraglacial ponds and ice cliffs inventory. For example, from 2020 (Pléiades) to 2021 (Planet) happened an increase of 170% in pond area, however it is impossible to know if this interannual extent changes in pond area is factual or if the 3 m pixel resolution omitted smaller ponds from the inventory, consequently increasing the mean area of features. For future research, I advise choosing datasets with same resolution, even if it is necessary lowering temporal resolution. This resolution gap can be easily fixed in the near future with more drone surveys, as resolution can be customized to match any given dataset.

Percentual of area occupied by studied features could potentially show some uncertainty, that is because total area occupied by ponds and cliffs was compared to glacier area mapped in 2023. A more accurate percentage value of occupied area could be achieved if glacier area was mapped in each given year, as Tapado Glacier and debris-covered glacier are two dynamic components of Tapado Complex which can undergo great area extent changes over the year. Robson et al. (2022) estimated a shrink of -25% ± 4.6% between 1955-2020 for the Tapado Glacier, and -0.25 ± 0.16% for the debris-covered glacier – although, within the time frame, those changes could be from 2.07 ± 2.84% to -1.63 ± 2.60% depending on the years and glacier section analyzed.

Another improvement could be made on the persistence analysis, as the whole dataset from 1955 to 2023 was used, in which the temporal resolution in not uniform and yearly. Thus, interannual variability suffered a strong bias due periods greater than 10 years being compared together. To achieve a better understanding of the interannual variability of supraglacial pond and ice cliffs, an analysis using only the datasets 2009-2010, 2017-2018, 2019-2020, 2022-

2023. In this way, both temporal and spatial resolution would contribute to accurate results, instead of creating biases.

A comparative analysis with climate data should follow the analysis made in order to estimate the climate drivers to pond and cliff dynamics, as some results could not be entirely explained yet, and the available observations shall be tested and fortified by climate variables (i.e., precipitation, humidity, temperature). For example, the year 2012 showed a relatively small total and mean ponded and cliffed area, as for smaller occupation percentage within the glacier extent, however, a higher number of ponds were present. Is this a consequence of change in temperature or precipitation? These questions could be easily answered with an integrated climate analysis. In LaLaguna catchment an automatic weather station (AWS) is positioned relatively close to the Tapado Complex, which could facilitate the acquisition of accurate meteorological data.

Relating to surface velocity dataset, it was only measured in between 2010 and 2020, this means that surface velocities in between 1955-2010 and 2020-2023 were only assumed and extrapolated from Robson et al. (2022) dataset. As Tapado Glacier does not present high velocity areas, nor expressive change in velocity, it was considered enough, however, for more precise velocity analysis and estimation, its advised to generate surface velocity for the periods it was absent.

Finally, surface lowering measurements are not enough to estimate the overall contribution of supraglacial ponds and ice cliffs to the mass balance and volume loss of the Tapado Glacier, however, it is an important starting point and showcases the overall dynamics experienced by the glacier. From the results acquired in this thesis, geodetic mass balance and volume changes can be easily calculated to enhance the overall understanding of the study area. However, surface elevation changes cannot be interpreted as incomplete values, as it is the main proxy to further calculation and gives a reasonable interpretation of supraglacial pond and ice cliff contribution to glacier wastage.

8. Conclusions

Across all studied years it was identified a total of 285 supraglacial ponds and 163 ice cliffs, with a mean size of 202.71 ± 55.45 m^2 and 270.33 ± 73.75 m^2, respectively, in which ~41% of ponds coinciding with an ice cliff and ~71% of cliffs were bordering a supraglacial pond in the scenes. It was also observed that those ponds marked by ice cliff contact are 4.16 times bigger on average.

Those features consistently occupy altogether more than 1.15% of debris-covered area since 2000, in which pond area is responsible for ~0.24 to 1.37% and cliff area for 0 to 1.26% of total debris-covered glacier. Although supraglacial pond size is considerably smaller if compared to other local and global glaciers, pond cover from total debris-covered glacier area is like other observations. In other hand, ice cliff cover is reduced in Tapado Glacier. A viable explanation is related to low pond persistence rates of perched ponds, that resonates in a retarded ice cliff evolution as calving processes within pond-cliff contact are stopped during consecutive drainage events.

They are highly dynamic components of the glacier located in surfaces from low to high slope (2° to 14°) and stagnant glacier velocities (0.78 ± 0.32 ma^{-1}). In contrast to the established bibliography based on huge glaciers, surface slope seems to act as a second drive for pond formation and size, while surface velocities are the main force that regulates pond disposition and extent, thus, ponds are likely to form in high surface gradient but unlikely to form even in moderate velocities. A proposed threshold for Tapado Glacier in which pond are likely to develop in zones > 2° & < 14° surface gradient and < 1.5 ma^{-1} surface velocity was made, as it accounts for ~83% of all mapped ponds.

This new threshold for pond formation and development can be consequence of two no corelated events. First, higher surface velocities at clean ice and debris-covered glacier contact can exert a longitudinal compression downwards, closing crevasses and relic conduits, thus, allowing pond formation in higher slope. The second possible explanation is a methodological-scale setting, once small supraglacial ponds in the Himalayas are < 1000 m^2, it is possible that small ponds are the ones found in Tapado Glacier are omitted or treated as isolated smaller ponds and less hazardous.

A second important find here is the distance threshold of supraglacial ponds and ice cliffs influence on surface lowering of the surrounding terrain. Analyzes done in different time scales

(i.e. individual years or time periods) and distances (i.e, accounting changes at water surface or excluding it) observed the same threshold of 15 m under ice cliff influence. This revealed that in distances above 15 m the surface lowering tends to homogenize within the years, periods, and in between supraglacial ponds with cliffs and without cliffs. It was show that ice cliffs enhance surface lowering in ~46.57% more than supraglacial ponds absent of cliffs, with differences in lowering up to 0.48 ± 0.32 ma^{-1}, while after the threshold those differences in lowering are maximum 0.08 ± 0.32 ma^{-1} in between analyzed period.

This threshold distance of influence explains and are explained by the "debris-cover glacier anomaly", where debris-cover glacier posses thinning rates in the same magnitude of clean ice tongue, even though they have an insulating debris mantle that should reduce melt. It was also demonstrated that in Tapado Glacier the upper debris-covered glacier and clean-ice glacier have similar lowering rates. Those lowering rates are heavily boosted by ice cliffs with an average magnitude of change 6.53 times higher than the debris-cover glacier.

Third and last, the 3D analysis of retreat rates with M3C2 algorithm proved to be more precise and accurate than dDEM derived surface changes. In between 2020-2023, for the same area, the product derived from high resolution satellites omitted 2.93% of surface elevation changes in only on cliff and was attached to an uncertainty ~5057% higher than the dense point cloud derived product. This omission, even though it seems smaller, can potentially sum up when analyzing bigger areas and longer time periods, leading to a high uncertainty when used as input for modelling and other followed up analysis. Thus, SfM from UAV and point cloud distance calculation from M3C2 proved to be a highly estimated methodology, not yet broadly applied.

9. References

Alvarez-Garreton, C., Mendoza, P. A., Boisier, J. P., Addor, N., Galleguillos, M., Zambrano-Bigiarini, M., Lara, A., Puelma, C., Cortes, G., Garreaud, R., McPhee, J., and Ayala, A.: The CAMELS-CL dataset: catchment attributes and meteorology for large sample studies – Chile dataset, Hydrol. Earth Syst. Sci., 22, 5817–5846, https://doi.org/10.5194/hess-22-5817-2018, 2018.

Alvarez-Garreton, C., Boisier, J. P., Garreaud, R., Seibert, J., and Vis, M.: Progressive water deficits during multiyear droughts in basins with long hydrological memory in Chile, Hydrol. Earth Syst. Sci., 25, 429–446, https://doi.org/10.5194/hess-25-429-2021, 2021.

Anderson, R.: A model of ablation-dominated medial moraines and the generation of debris-mantled glacier snouts. Journal of Glaciology, 46, 459-469, https://doi.org/10.3189/172756500781833025, 2000.

Aniya, M: Glacier Inventory for the Northern Patagonia Icefield Chile and Variations 1944/45 to 1985/86, Arctic and Alpine Research, 20, 179-187, http://dx.doi.org/10.2307/1551496, 1988.

Aniya, M., Sato, H., Naruse, R., Skvarca, P., & Casassa, G.: Recent Glacier Variations in the Southern Patagonia Icefield, South America. Arctic and Alpine Research, 29(1), 1–12. https://doi.org/10.2307/1551831, 1997.

Azócar, G.F. and Brenning, A.: Hydrological and Geomorphological Significance of Rock Glaciers in the Dry Andes, Chile (278–338S), Permafrost and Periglac. Process, 21, 42–53, https:// 10.1002/ppp.669doi.org/ 10.1002/ppp.669, 2010.

Azócar, G. F., Brenning, A., Bodin, X.: Permafrost distribution modelling in the semi-arid Chilean Andes, The Cryosphere, 11, 877–890, https://doi.org/10.5194/tc-11-877-2017, 2017.

Barcaza, G., Nussbaumer, S., Tapia, G., Valdés, J., García, J., Videla, Y., Albornoz, A., Arias, V.: Glacier inventory and recent glacier variations in the Andes of Chile, South America, Annals of Glaciology, 58, 166-180, https://doi.org/10.1017/aog.2017.28, 2017.

Benn, D., Wiseman, S., Hands, K.: Growth and drainage of supraglacial lakes on debris-mantled Ngozumpa Glacier, Khumbu Himal, Nepal, Journal of Glaciology, 47, 626-638, https://doi.org/10.3189/172756501781831729, 2001.

Benn, D., Gulley, J., Luckman, A., Adamek, A., Glowacki, P, Englacial drainage systems formed by hydrologically driven crevasse propagation, Journal of Glaciology, 55(191), 513-523, https://doi.org/10.3189/002214309788816669, 2009.

Benn, D.I., Bolch, T., Hands, K., Gulley, J., Luckman, A., Nicholson, L.I., Quincey, D., Thompson, S., Toumi, R., Wiseman, S.: Response of debris-covered glaciers in the Mount Everest region to recent warming, and implications for outburst flood hazards, Earth-Science Reviews,114, 156-174, https://doi.org/10.1016/j.earscirev.2012.03.008, 2012.

Briner, J.P: Dating glacial landforms. In: Vijay P. Singh, Pratap Singh & Umesh K. Haritashya (eds.), Encyclopedia of Snow, Ice and Glaciers, 175-176, https://doi.org/10.1007/978-90-481-2642-2_616, 2011.

Bolch, T., Buchroithner, M., Pieczonka, T., & Kunert, A.: Planimetric and volumetric glacier changes in the Khumbu Himal, Nepal, since 1962 using Corona, Landsat TM and ASTER data.

Journal of Glaciology, 54(187), 592-600, https://doi.org/10.3189/002214308786570782, 2008.

Brun, F., Buri, P., Miles, E., Wagnon, P., Steiner, J., Berthier, E., Ragettli, S., Kraaijenbrink, P., Immerzeel, W.W., Pellicciotti, F.: Quantifying volume loss from ice cliffs on debris-covered glaciers using high-resolution terrestrial and aerial photogrammetry, Journal of Glaciology, 62(234), 684-695, https://doi.org/10.1017/jog.2016.54, 2016.

Brun, F., Wagnon, P., Berthier, E., Shea, J. M., Immerzeel, W. W., Kraaijenbrink, P. D. A., Vincent, C., Reverchon, C., Shrestha, D., and Arnaud, Y.: Ice cliff contribution to the tongue-wide ablation of Changri Nup Glacier, Nepal, central Himalaya, The Cryosphere, 12, 3439–3457, https://doi.org/10.5194/tc-12-3439-2018, 2018.

Brun, F., Wagnon, P., Berthier, E., Shea, J. M., Immerzeel, W. W., Kraaijenbrink, P. D. A., Vincent, C., Reverchon, C., Shrestha, D., Arnaud, Y.: Ice cliff contribution to the tongue-wide ablation of Changri Nup Glacier, Nepal, central Himalaya, The Cryosphere, 12, 3439–3457, https://doi.org/10.5194/tc-12-3439-2018, 2018.

Buri, P., Miles, E. S., Steiner, J. F., Immerzeel, W. W., Wagnon, P., and Pellicciotti, F.: A physically based 3-D model of ice cliff evolution over debris-covered glaciers, J. Geophys. Res. Earth Surf., 121, 2471–2493, https://doi.org/10.1002/2016JF004039, 2016a.

Buri, P., Pellicciotti, F., Steiner, J., Miles, E., Immerzeel, W.: A grid-based model of backwasting of supraglacial ice cliffs on debris-covered glaciers, Annals of Glaciology, 57, 199-211, https://doi.org/10.3189/2016AoG71A059, 2016b.

Buri, P. and Pellicciotti, F.: Aspect controls the survival of ice cliffs on debris-covered glaciers, P. Natl. Acad. Sci. USA, 115, 4369– 4374, https://doi.org/10.1073/pnas.1713892115, 2018.

Buri, P., Miles, E. S., Steiner, J. F., Ragettli, S., and Pellicciotti, F.: Supraglacial Ice Cliffs Can Substantially Increase the Mass Loss of Debris-Covered Glaciers, Geophys. Res. Lett., 48, e2020GL092150, https://doi.org/10.1029/2020GL092150, 2021.

Casassa, G., Rodríguez, J.L., Loriaux, T.: A New Glacier Inventory for the Southern Patagonia Icefield and Areal Changes 1986–2000. In: Kargel, J., Leonard, G., Bishop, M., Kääb, A., Raup, B. (eds), Global Land Ice Measurements from Space, Springer Praxis Books, Springer, Berlin, Heidelberg, https://doi.org/10.1007/978-3-540-79818-7_27, 2014.

Chand, M.B., Watanabe, T.: Development of Supraglacial Ponds in the Everest Region, Nepal, between 1989 and 2018, Remote Sens, 11, 1058, https://doi.org/10.3390/rs11091058, 2019.

Chen, F., Wang, J., Li, B., Yang, A., Zhang, M.: Spatial variability in melting on Himalayan debris-covered glaciers from 2000 to 2013, Remote Sensing of Environment, 291, 113560, ISSN 0034-4257, https://doi.org/10.1016/j.rse.2023.113560, 2023.

Clayton, A.I.: Remote sensing of subglacial bedforms from the British Ice Sheet using an unmanned aerial system (UAS): Problems and potential, Durham E-thesis Durham University, 2012.

Cortés, A.E., Oyarzún, R., Kretschmer, N., Chaves, H., Soto, G., Soto, M., Amézaga, J., Oyarzún, J., Rötting, T., Señoret, M., Maturana, H.: Application of the Watershed Sustainability Index to the Elqui river basin, North-Central Chile, Obras y Proyectos, 12, 57-69, 2012.

Crocker, R. I., Maslanik, J. A., Adler, J. J., Palo, S. E., Herzfeld, U. C., Emery, W. J.: A Sensor Package for Ice Surface Observations Using Small Unmanned Aircraft Systems, IEEE

Transactions on Geoscience and Remote Sensing, 50, 4, 1033-1047, https://doi.org/10.1109/TGRS.2011.2167339, 2012.

Dirección General de Aguas (DGA): Dinámica de glaciares rocosos en el Chile semiárido Technical report, Santiago de Chile, 2010.

Dirección General de Aguas (DGA): Atlas del Agua, Chile 2016, Dirección General de Aguas (DGA), Ministerio de Obras Publicos. Retrieved from http://www.dga.cl/atlasdelagua/Paginas/default.aspx. Accessed 22 August 2023.

Escobar, F. and Aceituno, P.: ENSO influence on Andean winter snowfall in central Chile, Bull. Inst. fr. étud. Andines, 27, 753–759, 1998.

Etzelmüller, B., Hagen, J., Vatne, G., Ødegård, R., Sollid, J.: Glacier debris accumulation and sediment deformation influenced by permafrost: Examples from Svalbard, Annals of Glaciology, 22, 53-62, https:/doi.org/10.3189/1996AoG22-1-53-62, 1996.

Falvey, M. and Garreaud, R.: Wintertime Precipitation Episodes in Central Chile: Associated Meteorological Conditions and Orographic Influences, J. Hydrometeor., 8, 171–193, https://doi.org/10.1175/JHM562.1, 2007.

Favier, V., Falvey, M., Rabatel, A., Praderio, E., López, D.: Interpreting discrepancies between discharge and precipitation in high-altitude area of Chile's Norte Chico region (26–32°S), Water Resour. Res., 45, W02424, https://doi.org/10.1029/2008WR006802, 2009.

Friedli, E: Photogrammetric methods for the reconstruction and monitoring of glaciers, Master Thesis ETH Zurich (http://www.igp.ethz.ch/photogrammetry/education/oldstudentsprojects/MA_Report_EFriedli_final.pdf. Accessed on September, 2013.

Fyffe, C. L., Brock, B. W., Kirkbride, M. P., Mair, D. W. F., Arnold, N. S., Smiraglia, C., Diolaiuti, G., Diotri, F.: An investigation of the influence of supraglacial debris on glacier-hydrology, The Cryosphere Discuss., 9, 5373–5411, https://doi.org/10.5194/tcd-9-5373-2015, 2015.

Gao, J.: Global population projection grids based on Shared Socioeconomic Pathways (SSPs), downscaled 1-km grids, 2010–2100. Palisades, NY: NASA Socioeconomic Data and Applications Center (SEDAC), https://doi.org/10.7927/H44747X4, 2019.

Gruber, S.: Derivation and analysis of a high-resolution estimate of global permafrost zonation. The Cryosphere, 6, 221–233, https://doi.org/doi:10.5194/tc-6-221-2012,2021.

Hall, D.K., Benson, C.S., Field; W.O: Changes of glaciers in glacier bay, Alaska, using ground and satellite measurements, Physical Geography, 16:1, 27-41, https://10.1080/02723646.1995.10642541, 1995.

Herreid, S., Pellicciotti, F.: The state of rock debris covering Earth's glaciers, Nat. Geosci., 13, 621–627, https://doi.org/10.1038/s41561-020-0615-0, 2020.

Hock, R., G. Rasul, C., Adler, B., Cáceres, S., Gruber, Y., Hirabayashi, M., Jackson, A., Kääb, S., Kang, S., Kutuzov, Al., Milner, U., Molau, S., Morin, B., Orlove, H. Steltzer: High Mountain Areas. In: Pörtner, H.O., Roberts, D.C., Masson-Delmotte, V., Zhai, P., Tignor, M., Poloczanska, E., Mintenbeck, K., Alegría, A., Nicolai, M., Okem, A., Petzold, J., Rama, B., Weyer, N.M. (eds.), IPCC Special Report on the Ocean and Cryosphere in a Changing Climate, Cambridge University Press, Cambridge, UK and New York, NY, USA, 131-202. https://doi.org/10.1017/9781009157964.004, 2019.

Hugonnet, R., Brun, F., Berthier, E., Dehecq, A., Mannerfelt, E.S., Eckert, N., Farinotti, D.: Uncertainty Analysis of Digital Elevation Models by Spatial Inference From Stable Terrain. In IEEE Journal of Selected Topics in Applied Earth Observations and Remote Sensing, 15, 6456-6472, https://doi.org/10.1109/JSTARS.2022.3188922, 2022.

Huo D., Bishop, M.P., Bush, A.B.G.: Understanding Complex Debris-Covered Glaciers: Concepts, Issues, and Research Directions, Front. Earth Sci, 9, 652279, https://doi.org/10.3389/feart.2021.652279, 2021.

Immerzeel, W.W. Kraaijenbrink, P.D.A, Shea, J.M., Shrestha, A.B., Pellicciotti, F., Bierkens, M.F.P., de Jong, S.M.: High-resolution monitoring of Himalayan glacier dynamics using unmanned aerial vehicles, Remote Sensing of Environment, 150, 93-103, https://doi.org/10.1016/j.rse.2014.04.025, 2014.

Inoue, J., Curry, J., Maslanik, J.: Application of aerosondes to melt-pond observations over Arctic sea ice, Journal of Atmospheric and Oceanic Technology, 25(2), 327–334, 2008.

James, M.R., Robson, S.: Sequential digital elevation models of active lava flows from ground-based stereo time-lapse imagery, ISPRS Journal of Photogrammetry and Remote Sensing, 97, 160-170, https://doi.org/10.1016/j.isprsjprs.2014.08.011, 2014.

Janke, J.R., Ng, S., Bellisario, A:: An inventory and estimate of water stored in firn fields, glaciers, debris-covered glaciers, and rock glaciers in the Aconcagua River Basin, Chile, Geomorphology, 296, 142-152, https://doi.org/10.1016/j.geomorph.2017.09.002, 2017.

Jones, B., O'Neil, B.V.O.: Spatially explicit global population scenarios consistent with the Shared Socioeconomic Pathways, Environ. Res. Lett., 11, 084003, https://doi.org/10.1088/1748-9326/11/8/084003, 2016.

Kääb, A., Gudmundsson, G.H., Hoelzle, M.: Surface deformation of creeping mountain permafrost. Photogrammetric investigations on rock glacier Murtèl, Swiss Alps, 7th International Permafrost Conference, Yellowknife, Canada: 531–537, 1998.

Kappenger, G., Steinegger, U., Braun, L.N., Kotska, r.: Recent changes in glacier tongue in the Langtang Khola basin, Nepal, determined by terrestrial photogrammetry, IAHS Publ., 218, 1993.

Kirkbride, M. and Warren, C.: Calving processes at a grounded ice cliff, Annals of Glaciology, 24, 116-121, https://doi.org/10.3189/S0260305500012039, 1997.

Kirkbride, M.P.: Debris-Covered Glaciers. In: Singh, V.P., Singh, P., Haritashya, U.K. (eds), Encyclopedia of Snow, Ice and Glaciers, Encyclopedia of Earth Sciences Series, Springer, Dordrecht, 180-182, https://doi.org/10.1007/978-90-481-2642-2_622, 2011.

Kneib, M., Miles, E. S., Buri, P., Molnar, P., McCarthy, M., Fugger, S., Pellicciotti, F.: Interannual dynamics of ice cliff populations on debris-covered glaciers from remote sensing observations and stochastic modeling, Journal of Geophysical Research: Earth Surface, 126, e2021JF006179, https://doi.org/10.1029/2021JF006179, 2021.

Kneib, M., Miles, E. S., Buri, P., Fugger, S., McCarthy, M., Shaw, T. E., Chuanxi, Z., Truffer, M., Westoby, M. J., Yang, W., Pellicciotti, F.: Sub-seasonal variability of supraglacial ice cliff melt rates and associated processes from time-lapse photogrammetry, The Cryosphere, 16, 4701–4725, https://doi.org/10.5194/tc-16-4701-2022, 2022.

Kraaijenbrink, P., Meijer, S., Shea, J., Pellicciotti, F., De Jong, S., Immerzeel, W.: Seasonal surface velocities of a Himalayan glacier derived by automated correlation of unmanned aerial

vehicle imagery. Annals of Glaciology, 57, 103-113, https://doi.org/10.3189/2016AoG71A072, 2016.

Lague, D., Brodu, N. Leroux, J.: Accurate 3d comparison of complex topography with terrestrial laser scanner: application to the Rangitikei Canyon (n-z), ISPRS Journal of Photogrammetry and Remote Sensing, 82, 10-26, https://doi.org/10.1016/j.isprsjprs.2013.04.009, 2013.

Liu, Q., Mayer, C., Liu, S.: Distribution and recent variations of supraglacial lakes on dendritic-type glaciers in the Khan Tengri-Tomur Mountains, Central Asia, The Cryosphere Discuss., 7, 4545–4584, https://doi.org/10.5194/tcd-7-4545-2013, 2013.

Liu, Q., Mayer, C., Liu, S.: Distribution and interannual variability of supraglacial lakes on debris-covered glaciers in the Khan Tengri-Tumor Mountains, Central Asia, Environ. Res. Lett., 10, 014014, https://doi.org/10.1088/1748-9326/10/1/014014, 2015.

Loriaux, T. and Ruiz, L.: Spatio-Temporal Distribution of Supra-Glacial Ponds and Ice Cliffs on Verde Glacier, Chile, Frontiers in Earth Science, 9, https://doi.org/10.3389/feart.2021.681071, 2021.

MacDonell, S., Kinnard, C., Mölg, T., Nicholson, L., and Abermann, J.: Meteorological drivers of ablation processes on a cold glacier in the semi-arid Andes of Chile, The Cryosphere, 7, 1513–1526, https://doi.org/10.5194/tc-7-1513-2013, 2013.

Meier, M.: Application of remote-sensing techniques to the study of seasonal snow cover. Journal of Glaciology, 15(73), 251-265, https:/doi.org/10.3189/S0022143000034419, 1975.

Meza, F.J., Vicuna, S., Gironás, J., Poblete, D:, Suárez, F., Oertel, M.: Water–food–energy nexus in Chile: the challenges due to global change in different regional contexts, Water International, 40:5-6, 839-855, https://doi.org/10.1080/02508060.2015.1087797, 2015.

Miles, E., Pellicciotti, F., Willis, I., Steiner, J., Buri, P., Arnold, N.: Refined energy-balance modelling of a supraglacial pond, Langtang Khola, Nepal. Annals of Glaciology, 57, 29-40. https://doi.org/10.3189/2016AoG71A421, 2016.

Miles, E.S., Steiner, J., Willis, I., Buri, P., Immerzeel, Wa.W., Chesnokova, A., Pellicciotti, F.: Pond Dynamics and Supraglacial-Englacial Connectivity on Debris-Covered Lirung Glacier, Nepal, Frontiers in Earth Science, 5, https://doir.org/10.3389/feart.2017.00069, 2017a.

Miles, E., Willis, I., Arnold, N., Steiner, J., & Pellicciotti, F.: Spatial, seasonal and interannual variability of supraglacial ponds in the Langtang Valley of Nepal, 1999–2013, Journal of Glaciology, 63(237), 88-105, https://doi.org/10.1017/jog.2016.120, 2017b.

Miles, E. S., Willis, I., Buri, P., Steiner, J. F., Arnold, N. S., Pellicciotti, F.: Surface pond energy absorption across four Himalayan glaciers accounts for 1/8 of total catchment ice loss, Geophysical Research Letters, 45, 10, 464–10, 473, https://doi.org/10.1029/2018GL079678, 2018.

Monnier, S., Kinnard, C., Surazakov, A., and Bossy, W.: Geomorphology, internal structure, and successive development of a glacier foreland in the semiarid Chilean Andes (Cerro Tapado, upper Elqui Valley, 30 080 S., 69 550 W.), Geomorphology, 207, 126–140, https://doi.org/10.1016/j.geomorph.2013.10.031, 2014.

Navarro, G., MacDonell, S., Valois, R.: A conceptual hydrological model of semiarid Andean headwater systems in Chile. Progress in Physical Geography: Earth and Environment, 47, 668-686, https://doi.org/10.1177/03091333221147649, 2023.

Obu, J.: How Much of the Earth's Surface is Underlain by Permafrost?, Journal of Geophysical Research: Earth Surface. 126, e2021JF006123: https://doi.org/doi:10.1029/2021JF006123, 2021.

Patzelt, G.: The Austrian glacier inventory GI 1, PANGAEA, https://doi.org/10.1594/PANGAEA.844983, 1980.

Pourrier, J., Jourde, H., Kinnard, C., Gascoin, S., Monnier, S.: Glacier meltwater flow paths and storage in a geomorphologically complex glacial foreland: The case of the Tapado glacier, dry Andes of Chile (30°S), Journal of Hydrology, 519, 1068-1083, 0022-1694, https://doi.org/10.1016/j.jhydrol.2014.08.023, 2014.

Post, A., Richardson, D., Tangbron, W.V., Rosselot, F.L.: Inventory of Glaciers in the North Cascades, Washington, Geological Survey Professional Paper 705-A, United Stayes Government Printing Office, Washington, https://doi.org/10.3133/pp705A, 1971

Quincey, D.J., Richardson, S.D., Luckman, A., Lucas, R.M., Reynolds, J.M., Hambrey, M.J., Glasser, N.F.: Early recognition of glacial lake hazards in the Himalaya using remote sensing datasets, Global and Planetary Change, 56, 137-152, https://doi.org/10.1016/j.gloplacha.2006.07.013, 2007.

Rango, A. and Martinec, J: Accuracy of Snowmelt Runoff Simulation, Nordic Hydrology, 12, 265-274, 1981.

Reid, T. and Brock, B.: An energy-balance model for debris-covered glaciers including heat conduction through the debris layer, Journal of Glaciology, 56(199), 903-916, https://doi.org/10.3189/002214310794457218, 2017.

Reynolds, J.M.: On the formation of supraglacial lakes on debris-covered glaciers, IAHS Publ. 264 (Symposium at Seattle 2000 – Debris-Covered Glaciers), 153–161, 2000.

Robson, B. A., MacDonell, S., Ayala, Á., Bolch, T., Nielsen, P. R., and Vivero, S.: Glacier and rock glacier changes since the 1950s in the La Laguna catchment, Chile, The Cryosphere, 16, 647–665, https://doi.org/10.5194/tc-16-647-2022, 2022.

Röhl, K.: Characteristics and evolution of supraglacial ponds on debris-covered Tasman Glacier, New Zealand. Journal of Glaciology, 54(188), 867-880, https://foi.org/10.3189/002214308787779861, 2008.

Rounce, D. R., Hock, R., McNabb, R. W., Millan, R., Sommer, C., Braun, M. H., Malz, P. Maussion, F. Mouginot, J., Seehaus, T.C., Shean, D.E.: Distributed global debris thickness estimates reveal debris significantly impacts glacier mass balance, Geophysical Research Letters, 48, e2020GL091311, https://doi.org/10.1029/2020GL091311, 2021.

Ryan, J. C., Hubbard, A. L., Box, J. E., Todd, J., Christoffersen, P., Carr, J. R., Holt, T. O., Snooke, N.: UAV photogrammetry and structure from motion to assess calving dynamics at Store Glacier, a large outlet draining the Greenland ice sheet, The Cryosphere, 9, 1–11, https://doi.org/10.5194/tc-9-1-2015, 2015.

Sahu, R., Ramsankaran, R., Bhambri, R., Verma, P., Chand, P.: Evolution of Supraglacial Lakes from 1990 to 2020 in the Himalaya–Karakoram Region Using Cloud-Based Google Earth Engine Platform, J Indian Soc Remote Sens, https://doi.org/10.1007/s12524-023-01773-2, 2023.

Sakai, A., Takeuchi, N., Fujita, K. and Nakawo, M.: Role of supraglacial ponds in the ablation process of a debris-covered glacier in the Nepal, IAHS Publ, 264, Symposium at Seattle 2000 – Debris-Covered Glaciers, 119–130, 2000.

Sakai, A., Nakawo, M., Fujita, K.: Distribution Characteristics and Energy Balance of Ice Cliffs on Debris-covered Glaciers, Nepal Himalaya, Arctic, Antarctic, and Alpine Research, 34:1, 12-19, https://doi.org/10.1080/15230430.2002.12003463, 2002.

Sakai, A., Nishimura, K., Kadota, T., Takeuchi, N.: Onset of calving at supraglacial lakes on debris-covered glaciers of the Nepal Himalaya, Journal of Glaciology, 55(193), 909-917, https://doi.org/10.3189/002214309790152555, 2009.

Sakai, A. and Fujita, K.: Formation conditions of supraglacial lakes on debris-covered glaciers in the Himalaya, Journal of Glaciology, 56(195), 177-181, https://doi.org/10.3189/002214310791190785, 2010.

Santibáñez, F.: Possible Impact on Agriculture Due to Climatic Change and Variability in South America. In: Yoshino, M., Domrös, M., Douguédroit, A., Paszyński, J., Nkemdirim, L.C. (eds), Climates and Societies — A Climatological Perspective. The GeoJournal Library, 36, Springer, Dordrecht, https://doi.org/10.1007/978-94-017-1055-8_12, 1997.

Sato, Y., Fujita, K., Inoue, H., Sunako, S., Sakai, A., Tsushima, A., Podolskiy, E.A., Kayastha, R., Kayastha, R.B.: Ice Cliff Dynamics of Debris-Covered Trakarding Glacier in the Rolwaling Region, Nepal Himalaya, Frontiers in Earth Science, 9, https://doi.org/10.3389/feart.2021.623623, 2021.

Schaffer, N., MacDonell, S., Réveillet, M., Yáñez, E., Valois, R.: Rock glaciers as a water resource in a changing climate in the semiarid Chilean Andes, Reg Environ Change, 19, 1263–1279, https://doi.org/10.1007/s10113-018-01459-3, 2019.

Sinclair, K. E. and MacDonell, S.: Seasonal evolution of penitente glaciochemistry at Tapado Glacier, Northern Chile, Hydrol. Process., 30, 176–186, https://doi.org/10.1002/hyp.10531, 2016.

Solbø, S. and Storvold, R.: Mapping Avalbard glaciers with the cryowing UAS, Int. Arch. Photogramm, Remote Sens. Spatial Inf. Sci., XL-1/W2, 373–377, https://doi.org/10.5194/isprsarchives-XL-1-W2-373-2013, 2013.

Stefaniak, A.M., Robson, B.A., Cook, S.J., Clutterbuck, B., Midgley, N.G., Labadz, J.C.: Mass balance and surface evolution of the debris-covered Miage Glacier, 1990–2018, Geomorphology, 373, 107474, https://doi.org/10.1016/j.geomorph.2020.107474, 2021.

Steiner, J., Pellicciotti, F., Buri, P., Miles, E., Immerzeel, W., Reid, T.: Modelling ice-cliff backwasting on a debris-covered glacier in the Nepalese Himalaya. Journal of Glaciology, 61, 889-907, https://doi.org/10.3189/2015JoG14J194, 2015.

Steiner, J., Buri, P., Miles, E., Ragettli, S., Pellicciotti, F.: Supraglacial ice cliffs and ponds on debris-covered glaciers: Spatio-temporal distribution and characteristics, Journal of Glaciology, 65(252), 617-632, https://doi.org/10.1017/jog.2019.40, 2019

Strauch, G., Oyarzun, J., Fiebig-Wittmaack, M., González, E. Weise, S.M.: Contributions of the different water sources to the Elqui river runoff (northern Chile) evaluated by H/O isotopes, Isotopes in Environmental and Health Studies, 42:3, 303-322, https://doir.org/10.1080/10256010600839707, 2006.

Taylor, C., Carr, J., & Rounce, D.: Spatiotemporal supraglacial pond and ice cliff changes in the Bhutan–Tibet border region from 2016 to 2018, Journal of Glaciology, 68(267), 101-113, https://doi.org/10.1017/jog.2021.76, 2021

Thompson, S., Benn, D., Mertes, J., Luckman, A.: Stagnation and mass loss on a Himalayan debris-covered glacier: Processes, patterns and rates, Journal of Glaciology, 62(233), 467-485. https://doi.org/10.1017/jog.2016.37, 2016.

Tonkin, T.N., Midgley, N.G., Graham, D.J., Labadz, J.C.: The potential of small unmanned aircraft systems and structure-from-motion for topographic surveys: A test of emerging integrated approaches at Cwm Idwal, North Wales, Geomorphology, 226, 35-43, https://doi.org/10.1016/j.geomorph.2014.07.021, 2014.

United Nations Convention to Combat Desertification in those Countries Experiencing Serious Drought and/or Desertification, Particularly in Africa, Paris, 1994.

Vivero, S., Bodin, X., Farías-Barahona, D., MacDonell, S., Schaffer, N., Robson, B. A., Lambiel, C.: Combination of Aerial, Satellite, and UAV Photogrammetry for Quantifying Rock Glacier Kinematics in the Dry Andes of Chile (30°S) Since the 1950s, Frontiers in Remote Sensing, 2, https://doi.org/10.3389/frsen.2021.784015, 2021.

Vuille, M. and Milana, J.P.: High-latitude forcing of regional aridification along the subtropical west coast of South America, Geophys, Res. Lett., 34, L23703, https://doi.org/10.1029/2007GL031899, 2007.

Watson, C.S., Quincey, D.J., Carrivick, J.L., Smith, M.W.: The dynamics of supraglacial ponds in the Everest region, central Himalaya, Global and Planetary Change, Volume 142, 2016, 14-27, https://doi.org/10.1016/j.gloplacha.2016.04.008, 2016.

Watson, C., Quincey, D., Smith, M., Carrivick, J., Rowan, A., James, M.: Quantifying ice cliff evolution with multi-temporal point clouds on the debris-covered Khumbu Glacier, Nepal, Journal of Glaciology, 63(241), 823-837, https://doi.org/10.1017/jog.2017.47, 2017.

Westoby, M.J., Brasington, J., Glasser, N.F., Hambrey, M.J., Reynolds, J.M.: Structure-from-Motion photogrammetry: A low-cost, effective tool for geoscience applications, Geomorphology, 179, 300-314, https://doi.org/10.1016/j.geomorph.2012.08.021, 2012.

Westoby, M.J., Rounce, D.R., Shaw, T.E., Fyffe, C.L., Moore, P.L., Stewart, R.L., Brock, B.W.: Geomorphological evolution of a debris-covered glacier surface. Earth Surf. Process, Landforms, 45, 3431– 3448, https://doi.org/10.1002/esp.4973, 2020.

Whitehead, K. L.: An integrated approach to determining short-term and long-term patterns of surface change and flow characteristics for a polythermal Arctic glacier, PhD thesis Canada: University of Calgary, http://hdl.handle.net/11023/812, 2013.

Wigmore, O. and Mark, B.: Monitoring tropical debris-covered glacier dynamics from high-resolution unmanned aerial vehicle photogrammetry, Cordillera Blanca, Peru, The Cryosphere, 11, 2463-2480, https://doi.org/10.5194/tc-11-2463-2017, 2017.

van Woerkom, T., Steiner, J.F., Kraaijenbrink, P.D.A., Miles, E.S., Immerzeel, W.W.: Sediment supply from lateral moraines to a debris-covered glacier in the Himalaya, Earth Surf. Dynam., 7, 411–427, https://doi.org/10.5194/esurf-7-411-2019, 2019.

Zhang, G., Yao, T., Xie, H., Wang, W., Yang, W.: An inventory of glacial lakes in the Third Pole region and their changes in response to global warming, Global and Planetary Change, 131, 148-157, https://doi.org/10.1016/j.gloplacha.2015.05.013, 2015.